

The Physical Mechanism of Heat Transfer Augmentation in Stagnating Flows Subject to Freestream Turbulence and Related Studies

by: Andrew Roger Gifford

A dissertation submitted to the Faculty of the
Virginia Polytechnic Institute and State University
in partial fulfillment of the requirements for the degree of

Doctor of Philosophy
in
Mechanical Engineering

*Virginia Tech Department of Mechanical Engineering
Advanced Experimental Thermofluids Research Laboratory*

Dr. Thomas Diller, Chairman
Dr. Pavlos Vlachos, Co-Chairman
Dr. Clinton Dancey
Dr. Roger Simpson
Dr. Danesh Tafti

Blacksburg, VA

Keywords: heat transfer, turbulence, mechanism,
heat flux sensor, time-resolved, particle image velocimetry

Copyright 2008, Andrew R. Gifford

December 17, 2008

This page left blank.

The Physical Mechanism of Heat Transfer Augmentation in Stagnating Flows Subject to Freestream Turbulence and Related Studies

by: Andrew Roger Gifford

Abstract

The mechanism of heat transfer augmentation due to freestream turbulence in classic Hiemenz stagnation flow was studied experimentally for the first time using time-resolved digital particle image velocimetry (TRDPIV) and a new thin film heat flux sensor called the Heat Flux Array (HFA). Unique measurements of simultaneous, time-resolved velocity and surface heat flux data were obtained along the stagnation line on a simple, rectangular flat plate model mounted in a water tunnel facility. Identification and tracking of coherent structures in the stagnation region lends support to the theory that coherent structures experience stretching and amplification of vorticity by the mean flow strain rate upon approaching the stagnation surface. The resulting flow field in the near-wall region is comprised primarily of high strength, counter-rotating vortex pairs with decreased integral length scale relative to the imposed freestream turbulence. It is hypothesized that the primary mechanism of heat transfer augmentation is the movement of cooler freestream fluid into the heated near-wall region by these coherent structures. Furthermore, the level of heat transfer augmentation is dictated by the integral length scale, circulation strength, and core-to-surface distance of the coherent structures. To test this hypothesis, these properties were incorporated into a mechanistic model for predicting the transient, turbulent heat transfer coefficient. The model was successful in predicting the shape and magnitude of the measured heat transfer coefficient over much of the experimental measurement time.

In a separate yet related set of studies, heat flux sensors and calibration methods were examined. The High Temperature Heat Flux Sensor (HTHFS) was designed and developed to become one of the most durable heat flux sensors ever devised for long duration use in high temperature, extreme environments. Extensive calibrations in both conduction and convection were performed to validate the performance of the sensor near room temperature. The measured sensitivities in conduction and convection were both very close to the predicted sensitivity using a thermal resistance model of the HTHFS. The sensor performance was unaffected by repeated thermal cycling using kiln and torch firing. Finally, the performance of Schmidt-Boelter heat flux sensors were examined in both shear and stagnation flow using two custom designed convection calibration facilities. Calibration results were evaluated using an analytical sensitivity model based on an overall sensor thermal resistance from the sensor to the heat sink or mounting surface. In the case of convection the model included a term for surface temperature differences along the boundary layer. In stagnation flow the apparent sensitivity of the Schmidt-Boelter sensors decreased non-linearly with increasing heat transfer coefficient. Estimations of the sensor's internal thermal resistance were obtained by fitting the model to the stagnation calibration data. This resistance was then used with the model to evaluate the effects of non-uniform surface temperature on the shear flow sensitivity. A more pronounced non-linear sensitivity dependence on heat transfer coefficient was observed. In both cases the main result is that convection sensitivity varies a great deal from standard radiation calibrations.

Contents

Abstract	iii
Table of Contents	iv
List of Figures	vi
List of Tables	viii
Acknowledgements	ix
1 Introduction	1
1.1 Motivation	1
1.2 Structure of Dissertation	1
I Primary Studies	3
2 The Physical Mechanism of Heat Transfer Augmentation in Stagnating Flows Subject to Freestream Turbulence	4
2.1 Abstract	4
2.2 Nomenclature	5
2.3 Introduction	6
2.4 Background and Related Studies	6
2.5 A Hypothetical Mechanism	7
2.6 Water Tunnel Facility	8
2.7 Turbulence Generation	9
2.8 Experimental Model and Heat Transfer Instrumentation	9
2.9 Flow Measurements: Time-Resolved Digital Particle Image Velocimetry and Setup	10
2.10 Experiments and Procedures	11
2.11 Data Reduction and Analysis	11
2.11.1 Heat Transfer	11
2.11.2 TRDPIV: Image Processing, Proper Orthogonal Decomposition, and Turbulence Statistics	12
2.11.3 Coherent Structure Identification and Dynamic Tracking	13
2.12 Results	14
2.13 Laminar Flow and Heat Transfer	14
2.14 Time-average Turbulent Heat Transfer: Mean Augmentation	15
2.15 Transient Flow and Heat Transfer: Insight into the Mechanism of Heat Transfer Augmentation	16
2.16 Validation of the Transient Mechanistic Model	20
2.17 Conclusions	21
2.18 Acknowledgements	22
2.19 References	22
3 Further Validation of the Mechanistic Model for Heat Transfer Augmentation	26

3.1	Introduction	26
3.2	Modified Mechanistic Model Using A Cumulative Induced Velocity Method	27
3.3	Modified Mechanistic Model Validations	28
3.4	Trend Analysis Validations	31
3.5	Conclusions	32
3.6	References	33
 II Related Studies		 35
4	A Durable Heat Flux Sensor for Extreme Temperature and Heat Flux Environments	36
4.1	Abstract	36
4.2	Nomenclature	36
4.3	Introduction	37
4.4	Heat Flux Sensor Design	37
4.5	Theoretical HTHFS Sensitivity	39
4.6	Heat Flux Sensor Calibrations	40
	4.6.1 Introduction	40
	4.6.2 Conduction Calibration	40
	4.6.3 Convection Calibration	43
	4.6.4 Calibration Uncertainty Analysis	44
4.7	Thermal Cycling: Kiln and Torch Tests	46
4.8	Conclusions	47
4.9	Acknowledgements	48
4.10	References	48
5	Convection Calibration of Schmidt-Boelter Heat Flux Sensors in Shear and Stagnation Flow	50
5.1	Abstract	50
5.2	Nomenclature	50
5.3	Introduction	51
5.4	Heat Flux Measurement	51
5.5	General Thermal Model of the Heat Flux Gage	52
5.6	Heat Flux Gages	53
5.7	Radiation Calibration	55
5.8	Convection Calibration	56
5.9	Convection Calibration Facility	56
	5.9.1 Stagnation Stand	57
	5.9.2 Shear Stand	58
5.10	Data Analysis	60
5.11	Calibration Results	61
	5.11.1 Effects of Water Cooling	63
5.12	Conclusions and Recommendations	65
5.13	Acknowledgments	66
5.14	References	66
6	Conclusions and Recommendations for Future Research	67
6.1	Conclusions	67
6.2	Recommendations for Future Research	68
 Appendix		 70
A	Computational Codes	70

List of Figures

*Unless otherwise noted, all images are property of the author

2.1	A Hypothetical Mechanism for Heat Transfer Augmentation at a Stagnation Point	8
2.2	Hiemenz Flow Model and Instrumentation	9
2.3	Water Tunnel Facility and Experimental Setup	11
2.4	Laminar Flow and Boundary Layer	14
2.5	The effects of freestream turbulence on time-average heat transfer	15
2.6	Stream-wise variation in time-averaged flow properties and predicted heat transfer augmentation	16
2.7	Peak coherence and associated frequencies between fluctuating velocity and surface heat transfer	17
2.8	Comparison of fluctuating velocity and heat transfer signals in a region of high coherence	18
2.9	Histogram of coherent structures identified in the stagnation region and corresponding physical properties	18
2.10	Behavior of coherent structure integral length scale and circulation with core-to-plate distance	19
2.11	Coherent structure tracking results for a representative trial	20
2.12	Example #1: Mechanistic Model Validations for Stream-wise Coherent Structure Interaction	24
2.13	Example #2: Mechanistic Model Validations for a Complicated Coherent Structure Interaction	25
3.1	Schematic of Cumulative Induced Velocity Method	27
3.2	Mechanistic Model Predictions Using the Cumulative Induced Velocity Method: u_{θ_x-C}	29
3.3	Mechanistic Model Predictions Using the Cumulative Induced Velocity Method: u_{θ_y-C}	29
3.4	Mechanistic Model Predictions Using the Cumulative Induced Velocity Method: $u_{\theta-C}$	30
3.5	Accuracy of the Mechanistic Model Using $u_{\theta-C}$	31
3.6	Coherent Structure Circulation Versus Measured Heat Transfer In the Vicinity of the HFA	32
3.7	Coherent Structure Integral Length Scale Versus Measured Heat Transfer In the Vicinity of the HFA	33
3.8	Coherent Structure Reynolds Number Versus Measured Heat Transfer In the Vicinity of the HFA	34
4.1	Surface mountable HTHFS with High Temperature Housing	38
4.2	Simplified 1-D thermal resistance model of HTHFS	40
4.3	The Core of the Conduction Calibration Facility	41
4.4	Conduction Calibration Results	42
4.5	The Core of the Stagnation Flow Convection Calibration Facility	43
4.6	Convection Calibration Results	44
4.7	Thermal cycling HTHFS at $1050^{\circ}C$	47
4.8	Propane Torch Test Apparatus and Torch Testing	47

4.9	Example of Torch Testing Data	48
5.1	Simplified 1-D thermal resistance model of HTHFS	52
5.2	Heat flux gage resistance network for convection	54
5.3	Schematic diagram sketch of the Schmidt-Boelter gage	55
5.4	Schematic of the Convection Calibration Facility	56
5.5	Stagnation Calibration Stand	57
5.6	HFM mounting in a plate	58
5.7	Shear Stand Nozzles	59
5.8	Picture of the assembled shear stand	59
5.9	Exit nozzle velocities from total pressure measurements	60
5.10	Typical heat flux and temperature data for the shear stand	61
5.11	Typical progression of the heat transfer coefficient for the shear stand	61
5.12	Stagnation calibration sensitivities for <i>SB137861</i> in stagnation flow	62
5.13	Calibration sensitivities for <i>SB 137861</i> in shear flow	63
5.14	Stagnation calibration sensitivities for <i>SB 137861</i> in stagnation flow with water cooling	64
5.15	Calibration sensitivities for <i>SB 137861</i> in shear flow with water cooling	65

List of Tables

3.1	Induced Velocity Component Calculations	28
4.1	Maximum Temperatures and Seebeck Coefficients Near Room Temperature	38
4.2	Average Bias, Precision, and Total Uncertainties in Measured and Calculated Variables	46
4.3	Average Total Uncertainties in Sensitivity for Conduction and Convection	46
5.1	Summary of stagnation calibration results	62
5.2	Ratio of heat transfer coefficients for shear flow	64

Acknowledgements

I would like to extend my deepest gratitude to the following for help during the course of this research:

- My research advisors Dr. Thomas Diller and Dr. Pavlos Vlachos for their patience and guidance.
- My dissertation committee members Dr. Clinton Dancey, Dr. Roger Simpson, and Dr. Danesh Tafti.
- My collaborators: David Hubble, Jerrod Ewing, Clay Pullins, and Chris Weiland.
- The many office and machine shop personnel in Randolph Hall.
- My wonderful family and friends for their love and support over the years of schooling, especially Grandma Nancy Gifford and Grandma Marge Amy who have passed away during my time at Virginia Tech.
- My mother Catherine Amy Pierotti for always encouraging me to live up to my potential.
- My father Jeffrey Gifford for engaging my curiosity in the "way things work" in life.
- My "goodest boy" Fisher who is the greatest dog I've ever met.
- Last but certainly not least, my wife Erika. Without her love and support this endeavor would not have been possible.

Chapter 1

Introduction

1.1 Motivation

The effects of freestream turbulence on heat transfer in stagnating flows continues to be a challenging and important area of research. Numerous experimental and analytical studies have shown that elevated levels of freestream turbulence contribute to an increase in the mean or time-averaged surface heat transfer over laminar flow levels. Truly understanding the physical mechanism responsible for this heat transfer augmentation is essential for providing designers and engineers with very accurate and useful prediction tools. Better prediction tools will inevitably lead to more efficient, energy saving devices in a world of shrinking natural resources. In this largely experimental work, new and improved flow and heat transfer measurement technologies are used to gain a deeper insight into the augmentation mechanism.

1.2 Structure of Dissertation

The dissertation has been divided naturally into two parts. Part *I* reports on the results from the primary area of research, wherein the physical mechanism of heat transfer augmentation in stagnating flows subjected to freestream turbulence was examined. The mechanism of augmentation was studied experimentally for the first time using time-resolved digital particle image velocimetry (TRDPIV) and a new thin film heat flux sensor called the Heat Flux Array (HFA). Unique measurements of simultaneous, time-resolved velocity and surface heat flux data were obtained along the stagnation line on a simple, rectangular flat plate model mounted in a water tunnel facility. Chapter 2 goes into great detail about the post processing and analysis of the experimental flow and heat transfer data. In this case, deeper understanding of the physical mechanism was gained by identifying and tracking coherent structures as they interact with the stagnation region. A model was developed that successfully predicted transient surface heat flux measured with the HFA using only the properties of the tracked coherent structures in the TRDPIV flow field. Chapter 3 focuses on two unpublished aspects of the overall study which were not included in Chapter 2. These studies were designed to help improve and validate the mechanistic model. The first section describes modifications to the mechanistic model using a cumulative induced velocity method for evaluating the fluid motion generated at the HFA sensor by all coherent structures present in the flow field. The results of this improved model are compared to the measured heat transfer for validation. In the second section, trends are identified in coherent structure properties and associated heat transfer near the HFA sensor. The results are used to validate the form and function of the mechanistic model.

Part *II* contains a number of secondary, yet related studies dealing with the development and calibration of heat flux sensors. Much of this work was necessary for completion of the primary research objectives. Chapter 4 discusses the design, development, and evaluation of an entirely new and novel heat flux sensor called the High Temperature Heat Flux Sensor (HTHFS). This robust heat flux sensor is designed to make long-duration measurements in extremely high temperature and heat flux environments. As discussed in Chapter 5, a major study on the convection calibration of Schmidt-Boelter type heat flux sensors in shear and stagnation flow was completed. The effects of heat transfer coefficient and flow orientation on the sensitivity of these heat flux sensors was quantified. Chapter 6 summarizes the key findings from the various works and suggests future research directions that may be taken. Finally, Appendix A provides reference copies of the various computer codes used in these studies.

Part I
Primary Studies

Chapter 2

The Physical Mechanism of Heat Transfer Augmentation in Stagnating Flows Subject to Freestream Turbulence

This chapter is comprised of sections from ASME Journal of Heat Transfer Paper No. *HT* – 08 – 1371 submitted on September 5, 2008. Acceptance of this paper for publication is still pending.

2.1 Abstract

Experiments have been performed in a water tunnel facility to examine the physical mechanism of heat transfer augmentation by freestream turbulence in classical Hiemenz flow. A unique experimental approach to studying the problem is developed and demonstrated herein. Time-Resolved Digital Particle Image Velocimetry (TRDPIV) and a new variety of thin film heat flux sensor called the Heat Flux Array (HFA) are used simultaneously to measure the spatio-temporal influence of coherent structures on the heat transfer coefficient as they approach and interact with the stagnation region. Laminar flow and heat transfer at low levels of freestream turbulence ($\overline{T}u_x = 1.0\%$) are examined to provide baseline flow characteristics and heat transfer coefficients. Similar experiments using the turbulence grid are performed to examine the effects of turbulence with mean stream-wise turbulence intensity of $\overline{T}u_x = 5.5\%$ and an integral length scale of $\overline{L}_x = 3.25\text{cm}$. At a Reynolds number of $\overline{Re}_d = \frac{\overline{U}_\infty D}{\nu} = 21,000$ an average increase in the mean heat transfer coefficient of 64% above the laminar level was observed. The mechanism of heat transfer augmentation in the stagnation region is investigated using a coherent structure identification scheme and a customized vortex tracking algorithm. Tracking these structures reveals a complex flow field in the vicinity of the stagnation region. It is dominated by counter-rotating vortex pairs, single sweeping vortex structures, and secondary flow structures. It is apparent through examination of transient physical properties (vortex circulation strength, length scale, and distance from the stagnation plate) that stretching of coherent structures from the freestream and subsequent amplification of vorticity affects near wall flow and heat transfer. A mechanistic model incorporating these physical properties is developed that successfully predicts the transient heat transfer coefficient measured by the HFA on the stagnation plate.

2.2 Nomenclature

a	stagnation flow parameter ($1/s$)
a_p	P.O.D. projection coefficient ($1/s$)
b	grid bar diameter (cm)
d	coherent structure core-to-surface distance (cm)
D	characteristic width of stagnation plate (cm)
f	frequency (Hz)
Fs	sampling frequency (Hz)
h	heat transfer coefficient ($W/cm^2 - ^\circ C$)
k	thermal conductivity ($W/cm - ^\circ C$)
M	TRDPIV camera magnification ($\mu m/pixel$)
Mu	grid spacing (cm)
N_p	total # POD projection coefficients
N_k	total # TRDPIV time instances
Nu	Nusselt number
Pr	Prandtl number
q''	heat flux (W/cm^2)
R	normalized autocorrelation function
S	power spectral density ($power/Hz$)
Re	Reynolds number
S_q	sensitivity of heat flux sensor ($\mu V/W/cm^2 - ^\circ C$)
t	time (s)
T	temperature ($^\circ C$)
Tu	turbulence intensity (%)
U	total flow velocity (cm/s)
u'	fluctuating velocity component (cm/s)
V_q	heat flux sensor output voltage (μV)

Greek Symbols

α	thermal diffusivity (cm^2/s)
δ	boundary layer thickness (cm)
$\Delta\epsilon$	TRDPIV vector spacing
Δh_{Turb}	turbulent heat transfer augmentation
γ	coherence (%)
Γ	vortex circulation (cm^2/s)
Λ	integral length scale (cm)
ν	kinematic viscosity (cm^2/s)
Θ	tangential velocity component (cm/s)
ϕ_p	POD eigenmode (cm)
σ	grid solidity (%)

Subscripts

s	stagnation plate surface
x,1	stream-wise or longitudinal flow direction
y,2	cross-stream or transverse flow direction

∞	freestream indicator
Turb	turbulent flow
Lam	laminar flow

2.3 Introduction

It has long been known that freestream turbulence has a pronounced effect on boundary layer heat transfer, particularly in regions of stagnating flow. Very high levels of surface heat transfer augmentation, or increase in mean heat transfer rate above laminar levels, have been observed for relatively small changes in freestream turbulence parameters. The importance of understanding and accurately modeling this phenomenon cannot be understated. Turbomachinery airfoils, for instance, are routinely operated at temperatures close to or exceeding their maximum material temperature limits. Being able to predict the peak heating loads on these airfoils is therefore crucial in maintaining structural integrity and achieving peak efficiency.

2.4 Background and Related Studies

There is to date a large body of experimental and theoretical work spanning over 65 years devoted to the topic of freestream turbulence and its effects on boundary layer heat transfer. Much of this work has focused on the effects of freestream turbulence on laminar flow in the stagnation region of various geometries. Hiemenz (1) was the first to solve the governing equations for laminar flow. Goldstein (2) and others examined the laminar heat transfer solutions for various heat transfer boundary conditions. Much of the experimental work dealing with the problem prior to 1965 has been summarized by Kestin (3). Subsequent experiments by Kestin et al. (3), (4), Smith and Kuethe (5), Lowery and Vachon (6), and others succeeded in determining the local and overall variation of heat transfer augmentation on cylinders. Correlations for the time-average stagnation region heat transfer as a function of Reynolds number, Prandtl number, and turbulence intensity were developed, although no single correlation could capture all available experimental data. Analytical work by Traci and Wilcox (7) and others using various turbulence models were somewhat successful in predicting the augmentation of heat transfer. The effects of turbulence parameters such as turbulence length scale have gained recent attention. Yardi and Sukhatme (8) have shown that for a given turbulence intensity and Reynolds number, decreasing length scale served to increase heat transfer augmentation. Experiments by Dullenkopft et. al. (9), Van Fossen et al. (10), (11), and recently by Sak (12) and Peyrin et al. (13) confirm that turbulence length scale is an important parameter in correlating stagnation point heat transfer. Beginning with the works of Sutera et al. (14), (15) a clearer picture of the mechanism of heat transfer augmentation emerged including the effects of turbulent length scale. It was shown numerically that freestream vorticity with scale greater than a certain neutral scale and orientation set parallel to the stagnation streamlines could be amplified near the boundary layer by the mean flow strain rate. This induced changes in the thermal and momentum boundary layers which led to significantly increasing surface heat transfer over laminar cases. A pair of recent numerical studies by Bae et al. (16), (17) provided yet another picture of how Reynolds number, disturbance intensity, and length scale affect heat transfer in the stagnation region. For a fixed disturbance amplitude and Reynolds number the augmentation of heat transfer increases with disturbance length scale up to a maximum length scale of $\Lambda/\delta \sim 5.3$ and then decreases. A numerical study by Zhongmin et al. (18) examined the effects of unsteady 3-D fluctuations upstream of a

Hiemenz boundary layer. Results similar to (17) were observed. A number of experimental studies (19), (20), (21) have examined the behavior of freestream turbulence in the stagnation region, many providing evidence for the vorticity amplification theory. Nearly all of these studies were performed in air using classic flow visualization and hot-wire methods. The first digital particle image velocimetry (DPIV) study of the problem was done by Sakakibara et al. (22). DPIV and laser induced fluorescence (LIF) were used to simultaneously measure flow field velocity and temperature near the stagnation point of a rectangular water jet impinging on a heated flat plate. In agreement with previous studies, maximum local increases in surface heat transfer coincided with the presence of coherent (vortex) structures which are stretched and amplified by the mean flow strain rate. Full flow field temperature measurements reveal that these structures create an "up-wash" region pulling cold fluid into the plate from the freestream while warmer fluid is ejected from the surface. This agrees qualitatively with the analytical results of (17). With the exception of the work in (22), particle image velocimetry has not been used to thoroughly study the problem. In this work advanced time-resolved DPIV techniques are used to examine the physical interaction of freestream turbulence and the heated Hiemenz boundary layer while simultaneously measuring transient surface heat transfer.

2.5 A Hypothetical Mechanism

In a recent paper by Nix et. al. (23) a mechanistic model was developed that successfully predicted experimentally measured values of time-average heat transfer to a stagnation region subjected to large-scale, high-intensity freestream turbulence. In this model it is assumed that an essentially laminar boundary layer exists in the stagnation region. Turbulent structures sweeping into the heated region bring cooler fluid near to the surface. This interaction causes an increase in heat transfer. It is suggested that an overall time-average heat transfer coefficient, $\overline{h_{Turb}}$ at the stagnation point can be described as a linear superposition of contributions from the mean laminar flow, $\overline{h_{Lam}}$ and that due to the turbulent structures interacting with the surface, $\Delta\overline{h_{Turb}}$:

$$\overline{h_{Turb}} = \overline{h_{Lam}} + \overline{\Delta h_{Turb}} \quad (2.1)$$

To model the augmentation or turbulent term a semi-infinite medium assumption is used. A coherent structure approaches the surface and exchanges energy via pure conduction:

$$\overline{\Delta h_{Turb}} = \frac{k}{\sqrt{\pi\alpha \frac{\overline{\Lambda_x}}{u'_{rms}}}} \quad (2.2)$$

where k and α are the thermal conductivity and thermal diffusivity of the fluid and the ratio of mean stream-wise integral length scale to stream-wise R.M.S. fluctuating velocity, $\overline{\Lambda_x}/u'_{rms}$ is a characteristic time scale for the interaction. These time-average flow properties were measured in a region of significant coherence between the measured heat transfer and fluctuating velocity near the stagnation point. Results predicted the time-averaged heat transfer augmentation for a variety of turbulence intensities and integral length scales (23). It is hypothesized that a new model, incorporating transient flow properties of individual coherent structures ($\Lambda, d, \Gamma, u_\theta$), would capture the fundamental physics of the interaction and in turn accurately predict the transient heat transfer measured experimentally in the stagnation region. These properties are shown schematically in Figure 2.1. After some simplification,

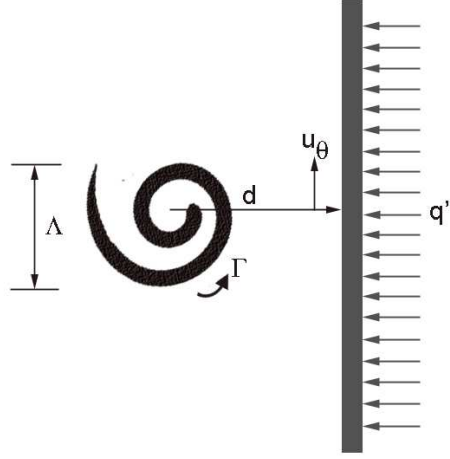


Figure 2.1: A Hypothetical Mechanism for Heat Transfer Augmentation at a Stagnation Point

the corresponding transient versions of Eqns. 2.1 and 2.2 are:

$$h_{Turb}(t) = h_{Lam}(t) + \Delta h_{Turb}(t), \text{ where :}$$

$$\begin{aligned} \Delta h_{Turb}(t) &= \frac{k}{\sqrt{\pi \Lambda^2(t) \frac{\alpha}{\nu} \frac{\nu}{\Lambda(t) u_\theta(t)}}} \\ &= \frac{k}{\Lambda(t) \sqrt{\pi}} Pr^{0.5} Re_\Lambda(t)^{0.5} \end{aligned} \quad (2.3)$$

In this case the Reynolds number is based on the induced velocity at the plate surface due to the coherent structure and the integral length scale:

$$Re_\Lambda = \frac{\Lambda(t) u_\theta(t)}{\nu} \quad (2.4)$$

The induced velocity, while measured experimentally may also be calculated by approximating a structure as an infinite line vortex. The Biot-Savart Law then gives:

$$u_\theta(t) = \left| \frac{\Gamma(t)}{2\pi d(t)} \right| \quad (2.5)$$

thereby incorporating the circulation or strength of the vortex and the distance of the structure core from the surface. Later in this work the identification, tracking, and analysis of coherent structures using TRDPIV data is discussed. Transient data from this analysis is used with Eqns. 2.1:2.5 to predict both the transient and time-average heat transfer coefficients measured experimentally with the HFA.

2.6 Water Tunnel Facility

The Virginia Tech AETHER Laboratory low speed water tunnel facility was used to conduct the current experiments. This variable speed, closed loop tunnel is impeller driven from approximately $0.05m/s$ to $1.0m/s$. The tunnel has a clear acrylic test section with dimensions of $0.61m \times 0.61m$ and a length of $1.77m$. A series of screens are used in the upstream contraction to reduce freestream turbulence, to around 1% over the length of the test section at low speeds.

2.7 Turbulence Generation

A simple bi-plane grid was designed, constructed, and tested with the intent of generating homogenous, isotropic turbulence in the water tunnel facility. Grid sizing was based on correlations by Baines and Peterson (24). The grid was constructed of rigid PVC pipe with nominal diameter $b = 2.14\text{cm}$. The center-to-center pipe spacing was set at $Mu = 4.8\text{cm}$, which gave a grid solidity of $\sigma \cong 70\%$. The performance of the grid design was evaluated using TRDPIV data reduction techniques described later in this work. With the time-average freestream velocity downstream of the grids set at 10cm/s , flow data was acquired at several x/b locations. The spatio-temporally averaged stream-wise turbulence intensity and stream-wise integral length scales are in good qualitative agreement with the correlations. Furthermore, the spatio-temporally averaged power spectral densities for the grid data compare well with the theoretical one-dimensional energy spectrum for homogeneous, isotropic turbulence of von Karman (25).

2.8 Experimental Model and Heat Transfer Instrumentation

A basic flat plate model was constructed to create classic Hiemenz stagnation flow. As shown in Figure 2.2 the model is comprised of a smooth, removable face plate mounted to a water-tight rectangular housing. Two long square tubes are used to hold the model rigidly in the flow and double as conduits to carry heater and sensor wires safely out of the water. A long splitter plate is attached aft of the rectangular housing to eliminate vortex shedding interactions with the stagnation region. The measurement

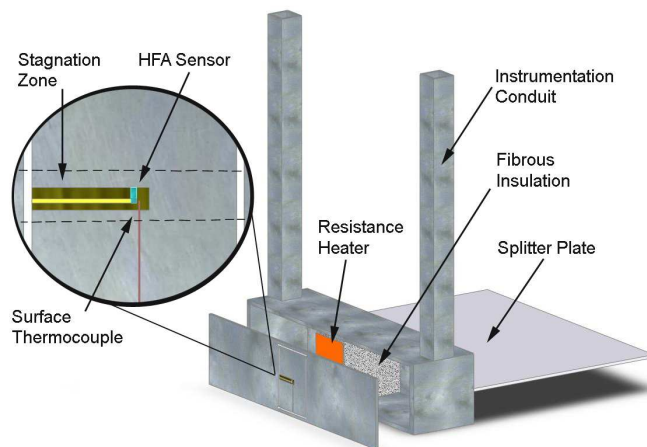


Figure 2.2: Hiemenz Flow Model and Instrumentation

area (inset Fig. 2.2) on the face plate is limited to a section approximately 10cm wide by 15cm tall at the center of the plate. This section is isolated thermally from the rest of the face plate by a series of channels machined through the surface. The entire testing area is heated to a uniform power density of $1.5\text{W}/\text{cm}^2$ using a thin-film resistance heating element applied with adhesive to the back of the plate. Low thermal conductivity fibrous insulation is applied to the back of the heater to force heat conduction through the face plate and into the oncoming flow.

The heat transfer instrumentation includes three fine wire thermocouples and one thin film heat flux sensor. The first type K thermocouple monitors heater core

temperature. A second type K thermocouple is embedded in the face plate adjacent to the heat flux sensor for measurements of fluctuating surface temperature. A final type K thermocouple is used to monitor the freestream temperature in the water tunnel facility. Measurements of the transient surface heat flux are made using a prototype sensor called the Heat Flux Array or HFA. This thin-film, direct-measurement sensor is based on a differential thermocouple design. Details of the design, fabrication, calibration, and performance of the HFA are found in (26) and (27). The HFA used in this study is hot pressed with thin plastic and epoxy onto the center of the measurement area in the stagnation line region as shown in Figure 2.2. The mean sensitivity of the HFA in convective heat transfer conditions was found to be $S_q = 42.6\mu V/W/cm^2$ measured in-situ on the stagnation plate surface. In all experiments discussed in this work the heat transfer data was sampled at a fixed frequency of using a National Instruments 6015DAQ and SCB – 16 block with 16 – bit resolution. The resulting data was down-sampled to the sampling frequency of the TRDPIV images. The microvolt signal of the HFA was first amplified using a custom fabricated amplifier with a fixed gain of 1000 and 480Hz anti-aliasing filter. Preliminary error analysis for the AETHER convection calibration facility (27) shows the measurement uncertainty of the HFA to be $\pm 6.6\%$.

2.9 Flow Measurements: Time-Resolved Digital Particle Image Velocimetry and Setup

This study examines the full two-dimensional velocity field in front of the experimental model using Time-Resolved Digital Particle Image Velocimetry or TRDPIV. This technique delivers non-invasive, full-flow-field velocity measurements with high spatial resolution and high sampling frequencies.

In digital particle image velocimetry (DPIV) a laser is used to illuminate a thin two-dimensional plane within a chosen flow field. Particles or tracers seeded in the flow become highly visible as they interact with and scatter light. A digital camera oriented normal to the laser plane captures images of the particles at precise intervals of time within a region of interest (ROI). The velocity field within the ROI may then be inferred by calculating the displacement of particle patterns between two or more images in the predetermined time interval. References (28) and (29) provide details on the general method.

As shown in Figure 2.3 the TRDPIV system used here employs a New Wave Research Pegasus dual head laser. The laser light is guided by an optical train and spread into a thin (1mm) plane which is aligned perpendicular to the stagnation flow model along the stagnation line. A Photron Fastcam digital camera is used to acquire images and is located underneath the water tunnel. Timing of the laser and camera are controlled via a timing hub and software by Integrated Design Tools Inc. A central PC is used to control the camera, laser, and timing hub and to acquire and store images and heat transfer data. The region of interest for these experiments was fixed at 8.75 cm tall by 10.75 cm wide centered on the HFA sensor junction along the stagnation line of the plate surface. The ROI was imaged using 1024 x 832 pixels, giving an image magnification of $M = 105.25\mu m/pixel$. With 4 pixel x 4 pixel vector spacing this ROI contains 53,248 vectors. TRDPIV data were continuously sampled in single pulsing fashion at Hz (i.e. one laser pulse per image at fixed time interval). This combination of magnification, ROI, and sampling rate was more than sufficient to resolve the characteristic scales of the grid turbulence. Sampling times were maximized to fill the available memory of the camera. This gave roughly 3200 images per trial or 60 seconds of data. The total uncertainty in TRDPIV velocity measurements using the aforementioned experimental setup and image-processing techniques is estimated to be $\pm 10\%$ (30).

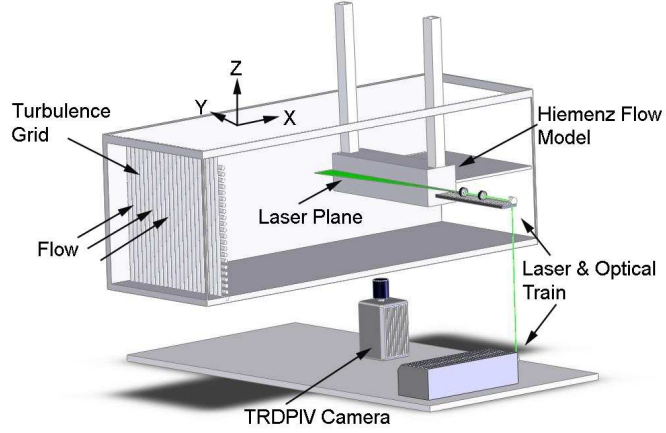


Figure 2.3: Water Tunnel Facility and Experimental Setup

2.10 Experiments and Procedures

In this work a single mean Reynolds number of $\overline{Re_D} = 21,000$ is used which corresponds to a mean freestream velocity $\overline{U_\infty} = 10\text{cm/s}$ and plate width in the z -direction of $D = 15.25\text{cm}$. An initial series of three laminar stagnation flow trials were completed to validate the experimental approach and provide baseline flow and heat transfer quantities for comparison with turbulent flow scenarios. Three trials were then completed to study the effects of freestream turbulence. Using the grid turbulence studies discussed previously the chosen grid-to-plate distance was fixed at $x/Mu = 17.5$. This provided a mean turbulence intensity of $\overline{Tu_x} 5.5\%$ and a mean stream-wise integral length scale of $\overline{\Lambda_x} = 3.25\text{cm}$ at this location in the absence of the stagnation model.

To begin an experiment the unheated stagnation plate was allowed to reach thermal equilibrium with the water tunnel. The heater was then turned on to full power and the system was allowed to reach steady state conditions. The TRDPIV system was then initiated and images were acquired. The laser pulse and camera signals were synchronized with the heat transfer data so precise comparison of the two data sets in time could be performed. A total of sixty seconds of concurrent TRDPIV and heat transfer data was acquired. The heater was then turned off.

2.11 Data Reduction and Analysis

The following subsections describe the data reduction procedures used to reduce the raw heat transfer and TRDPIV flow data for analysis.

2.11.1 Heat Transfer

All heat transfer raw voltage signals were first zero-phase-shift, low-pass filtered to 35Hz which is the highest frequency resolved by this particular HFA prototype. Transient surface temperature $T_s(t)$ and freestream temperature $T_\infty(t)$ were calculated in degrees Celsius using NIST Type-K thermocouple tables. The transient surface heat

flux $q_s''(t)$ was calculated according to Equation 2.6:

$$q_s''(t) = \frac{V_q(t)}{S_q} \quad (2.6)$$

where $V_q(t)$ and S_q are the gain adjusted transient HFA voltage output and HFA sensitivity, respectively. The transient surface heat transfer coefficient $h(t)$ whether laminar or turbulent follows from Newton's Law of Cooling:

$$h(t) = \frac{q_s''(t)}{(T_s(t) - T_\infty(t))} \quad (2.7)$$

In comparing turbulent flow quantities to turbulent heat transfer quantities it is customary to follow the Reynold's decomposition technique. Hence, the mean removed or fluctuating heat transfer coefficient becomes:

$$h'(t) = h(t) - \sum_{k=1}^N \frac{h(t_k)}{N_k} \quad (2.8)$$

where $k = 1, 2, \dots, N_k$ is the number of samples in the data set.

2.11.2 TRDPIV: Image Processing, Proper Orthogonal Decomposition, and Turbulence Statistics

The reduction of TRDPIV data begins with processing of the raw particle image sequences. Image processing is done using a custom analysis software package developed and validated by researchers in the AETHER laboratory. The details of the various methods used in image processing and validation can be found in Westerweel (29) and Eckstein (30). The focus here is on the post-processing of the two-dimensional flow field images. All post-processing was performed using customized codes in MATLAB.

A given TRDPIV data set is comprised of $k = 1, 2, \dots, N_k$ time instances t_k of the flow field each having a regularly spaced grid of $N_i \times N_j$ total vectors:

$$\vec{U}(x_i, y_j, t_k) = \sum_{l=1,2} u_l(x_i, y_j, t_k) \hat{x}_l \quad (2.9)$$

where for reference, index $l = 1$ corresponds to the x-direction and $l = 2$ corresponds to the y-direction which spans the ROI. Subscripts $i = 1, 2, \dots, N_i$ and $j = 1, 2, \dots, N_j$ are indices describing the x and y locations in the grid. Each of the TRDPIV flow fields contains a certain degree of noise dependent upon how the image sequences are processed and validated. The method of proper orthogonal decomposition (POD) is used in this study as a filtering tool to remove noise. As described in Smith et. al. (31) the method of P.O.D. seeks to reconstruct the original flow field $\vec{U}(x_i, y_j, t_k)$ in terms of N_p time dependent projection coefficients $a_p(t)$ and optimal basis functions or eigenmodes $\phi_p(x_i, y_j)$ such that:

$$\vec{U}(x_i, y_j, t_k) = \sum_{p=1}^{N_p} a_p(t_k) \phi_p(x_i, y_j) \quad (2.10)$$

Using Equation 10 it is possible to reconstruct the flow field using any number of eigenmodes. In fact, using only the most energetic eigenmodes in the flow field

reconstruction serves to eliminate high spatial frequency, and low energy noise. Hence, reconstruction of the flow fields in this study was done using only the number of modes required to capture 90% of the total flow field energy. This typically results in a substantially less noisy flow field, and one which better represents the flow structures of interest in this study. The POD reconstructed flow field is divided into mean and fluctuating velocity fields using Reynold's decomposition. The fluctuating velocities at each grid point at time t_k become:

$$u'_l(x_i, y_j, t_k) = u_l(x_i, y_j, t_k) - \sum_{k=1}^{N_k} \frac{u_l(x_i, y_j, t_k)}{N_k} \quad (2.11)$$

The first turbulence quantities calculated from the fluctuating velocity fields are the root-mean-square or R.M.S. velocity fields:

$$u'_{l-rms}(x_i, y_j) = \sqrt{\sum_{k=1}^{N_k} \frac{u'_l(x_i, y_j, t_k)^2}{N_k}} \quad (2.12)$$

The r.m.s velocity fields are used to calculate the turbulence intensities:

$$Tu_l(x_i, y_j, t_k) = \frac{u'_l(x_i, y_j, t_k)}{u'_{l-rms}(x_i, y_j)} \quad (2.13)$$

The integral length scale characterizes the largest, most energetic structures present in the turbulent flow field which are important contributors to heat transfer augmentation. Several methods exist for calculating the integral length scale, and recent studies have examined the accuracy and appropriate use of each method. In this work length scales are calculated by integration of spatial transverse and longitudinal autocorrelation functions up to the first zero crossing. The autocorrelations are calculated forwards and backwards along the transverse and longitudinal flow directions at each time t_k :

$$\Lambda_{\pm l}(x_i, y_j, t_k) = \int_0^{R_{u'_l u'_l}=0} R_{u'_l u'_l}(\pm \epsilon'_l) d\epsilon'_l \quad (2.14)$$

The longitudinal and transverse spatial autocorrelation functions at time t_k are calculated according to:

$$\begin{aligned} R_{u'_1 u'_1}(\pm \epsilon'_1) &= \frac{u'_1(x_i, y_j, t_k) u'_1(x_i \pm \epsilon'_1, y_j, t_k)}{u'_1(x_i, y_j, t_k) u'_1(x_i, y_j, t_k)} \\ R_{u'_2 u'_2}(\pm \epsilon'_2) &= \frac{u'_2(x_i, y_j, t_k) u'_2(x_i, y_j \pm \epsilon'_2, t_k)}{u'_2(x_i, y_j, t_k) u'_2(x_i, y_j, t_k)} \end{aligned} \quad (2.15)$$

2.11.3 Coherent Structure Identification and Dynamic Tracking

A number of works have examined methods of coherent structure identification. In this study the critical point method of Chong et. al. (32) is used. Briefly, critical points in the given 2D flow field, which collectively identify a coherent structure, occur when the following function is strictly positive:

$$\Delta = (Q/3)^3 + (R/2)^2 > 0 \quad (2.16)$$

where Q and R are invariants of the rate-of-deformation tensor for a particular point in the flow field. Ref. 35 provides more details on the method. Eq. 2.16 is applied to each point in the TRDPIV flow field at each time instance. In most cases the criterion results in closed contours of Δ surrounding clearly defined vortical structures. However, some subjective filtering is required to eliminate falsely identified structures which result from noise in approximation of the rate-of-deformation tensor. The tracking of coherent flow structures has been the subject of a number of works. The method utilized in this study is based on a simplified combination of features from Samtaney et. al. (33). Briefly, each time step in the coherent structure analysis results in a certain number of identified structures. Key parameters are calculated for each structure including: core location, integral length scale, and circulation. With the dense spatio-temporal information given by TRDPIV it is possible to track a particular structure in time without ambiguity by simply comparing these parameters at different time steps. This algorithm has proven reliable for tracking complex vortex motion in the stagnation region.

2.12 Results

2.13 Laminar Flow and Heat Transfer

One of the interesting features of laminar Hiemenz flow is the fact that the boundary layer thickness is constant across the stagnation region (1):

$$\delta_{Lam} = 2.40\sqrt{\frac{\nu}{a}} \quad (2.17)$$

where ν is the kinematic viscosity of the fluid and the parameter a depends on the characteristic width of the stagnating body and the freestream velocity. This parameter is found experimentally from TRDPIV measurements of laminar flow velocity along the stagnation streamline to be $a = 0.59(1/s)$. This gives a predicted boundary layer thickness of $\delta_{Lam} = 2.8mm$ using Eqn. 2.17. The film temperature was used to calculate thermodynamic properties, as the plate was heated in all three laminar flow trials.

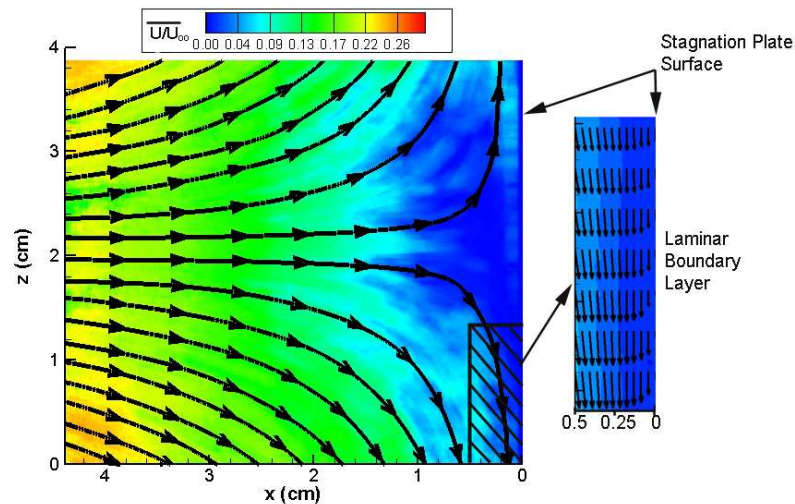


Figure 2.4: Laminar Flow and Boundary Layer

Figure 2.4 shows a contour plot of time-average velocity magnitude normalized by freestream velocity along with associated streamtraces. The comparison to classic Hiemenz flow is striking. The inset image in Fig. 2.4 shows a closer view of the laminar boundary layer. The measured laminar boundary layer thickness is approximately $\delta_{Lam} = 3.0mm$, which is slightly larger than that predicted using Eqn. 2.17. Focusing now on the thermal aspects of the laminar flow cases, the mean laminar heat transfer coefficient for the three trials was found to be $\overline{h_{Lam}} = 0.053W/cm^2 - ^\circ C$. The solution for the laminar heat transfer coefficient given by Goldstein (2) for stagnation point flow is:

$$h_{Lam} = 0.5421kPr^{0.42}\sqrt{\frac{a}{\nu}} \quad (2.18)$$

where k is the thermal conductivity of the fluid, Pr is the Prandtl number of the fluid, and a and ν are defined as previously. Using Eqn. 2.18 the predicted heat transfer coefficient is $\overline{h_{Lam}} = 0.058W/cm^2 - ^\circ C$. The value measured experimentally is slightly lower, but near the experimental uncertainty.

2.14 Time-average Turbulent Heat Transfer: Mean Augmentation

An example of the effect of freestream turbulence on stagnation heat transfer is seen in Figure 5. This image compares the time-average laminar value to the turbulent heat transfer coefficient measured by the HFA for a representative trial. It is clear that

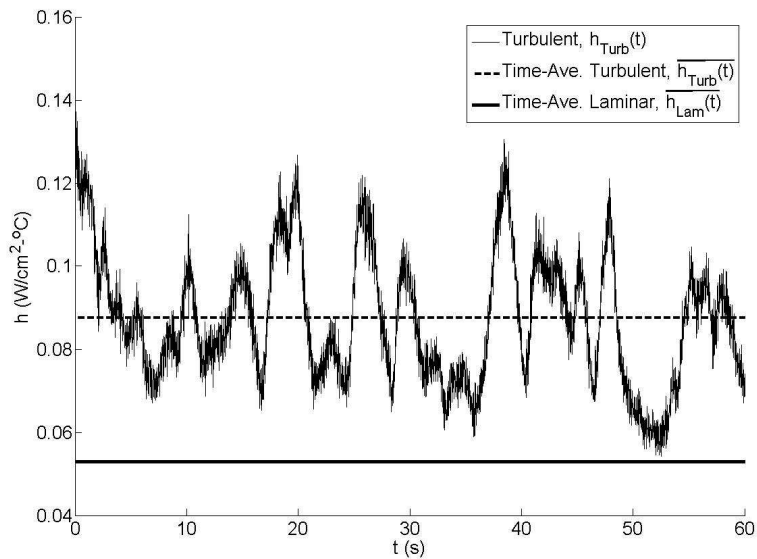


Figure 2.5: The effects of freestream turbulence on time-average heat transfer

large scale fluctuations in heat transfer coefficient serve to shift the mean heat transfer levels above the mean laminar values. The average augmentation for the three trials was $\Delta\overline{h_{Turb}} = 0.034W/cm^2 - ^\circ C$ or an increase of 64%. As discussed in section 2.5, Nix et. al. (23) developed a successful mechanistic model which uses time-averaged turbulent flow information in the vicinity of the stagnation region to predict the augmentation of heat transfer. This model was applied to the TRDPDV data taken

simultaneously with the turbulent heat transfer data shown in Figure 2.5. Figure 2.6 shows the stream-wise variations in the r.m.s. fluctuating velocity, u'_{l-rms} , time-averaged integral length scale, $\overline{\Lambda_{\pm 1}}$ and the time-averaged heat transfer augmentation according to Eqn. 2.2, $\overline{\Delta h_{Turb}}$. Reported values are spatial averages across the height (y-direction) of the TRDPIV field-of-view at each stream-wise location. As shown in

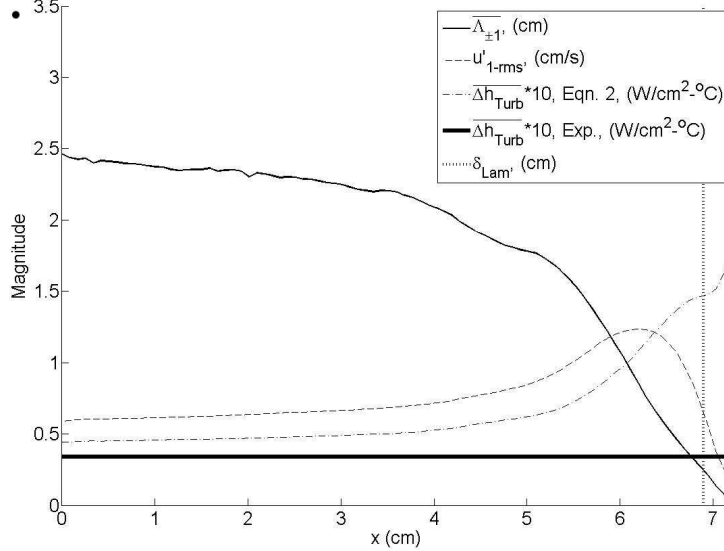


Figure 2.6: Stream-wise variation in time-averaged flow properties and predicted heat transfer augmentation

Figure 2.6 the time-averaged integral length scale begins lower than the freestream value and decreases to near zero at the stagnation plate surface. This demonstrates the influence of the stagnation plate upstream in the water tunnel facility beyond the TRDPIV field of view. The r.m.s. fluctuating velocity increases upon approaching $d \cong 3\delta_{Lam}$, then decreases near the stagnation plate surface. While this flow behavior is consistent with that observed by Nix et. al. (23) the predicted heat transfer augmentation using Eqn. 2 is shown to over-predict the experimentally measured value by around 30% across much of the TRDPIV field of view. It is not clear at this time why such a large discrepancy exists between the time-averaged experimental and predicted heat transfer augmentation. There are however pronounced differences in the experimental approaches of Reference (23) and the current study.

2.15 Transient Flow and Heat Transfer: Insight into the Mechanism of Heat Transfer Augmentation

To better understand the mechanism of heat transfer augmentation the coherence between the flow field and the measured heat transfer coefficient is examined. The coherence function is defined as:

$$\gamma_{AB}(f) = \frac{|S_{AB}^2|}{S_{AA}S_{BB}} \quad (2.19)$$

The coherence function is defined as the magnitude of the squared cross-power spectrum between two signals A and B normalized by the product of the auto-power spectrum for each signal. The resulting function of frequency has values on the interval $[0, 1]$. If two signals have a high coherence they share significant energy content at similar frequencies in time. Eqn. 2.19 was applied to the fluctuating velocity $u'_1(x_i, y_j, t)$ at every point in the transient flow field and the transient heat transfer coefficient, $h'_{Turb}(t)$ for the data shown in Figure 2.5. Figure 2.7(a) shows a contour plot of the maximum coherence between signals, while Figure 2.7(b) shows the corresponding frequency at the peak coherence.

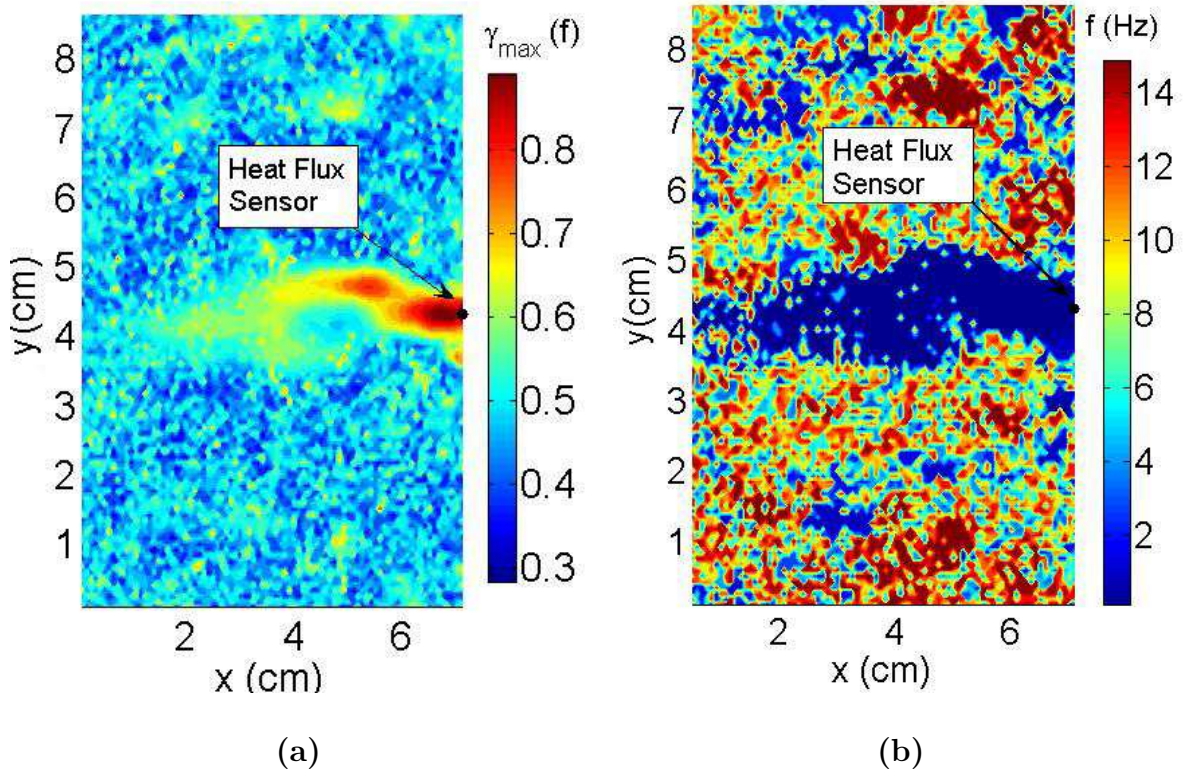


Figure 2.7: Peak coherence and associated frequencies between fluctuating velocity and surface heat transfer

It is clear from Figure 2.7(a – b) that very high levels of coherence are present corresponding to very low frequencies ranging from $0.1 - 1.5 Hz$. These low frequencies are precisely the frequencies of the integral length scales determined in our turbulence grid analysis. Figure 2.8 compares $u'_1(x_i, y_j, t)$ and $h'_{Turb}(t)$ in the region of high coherence, which is near the laminar boundary layer. It can be seen quite clearly that these low frequency, large scale fluctuations in velocity correspond directly to large fluctuations in heat transfer. A small amount of time lag on the order of $1.0s$ is also present. While the coherence analysis is beneficial it does not describe the physical nature of the flow structures interacting with the stagnation plate surface. This information was obtained using the coherent structure identification and tracking analysis described in Section 2.11.3. Coherent structures within the flow fields were first identified at each time instance. The mean integral length scale ($\overline{\Lambda_{\pm 1,2}}$), circulation (Γ), and core location and distance relative to the stagnation plate surface

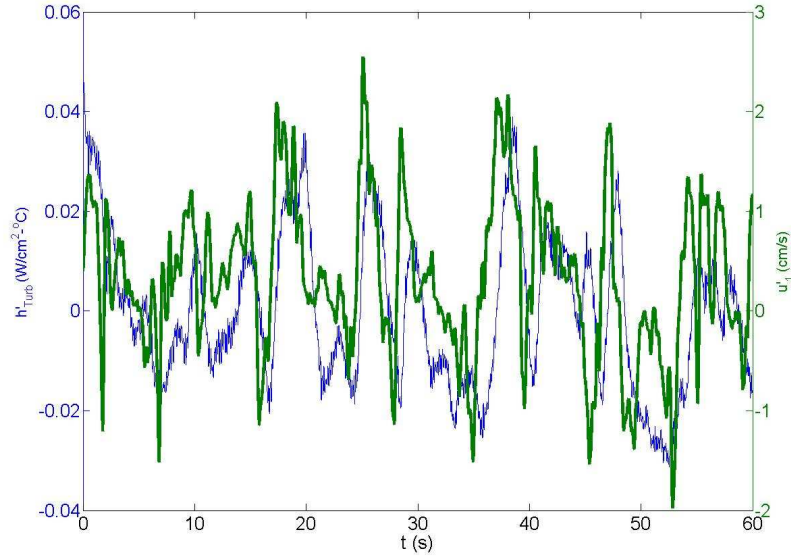


Figure 2.8: Comparison of fluctuating velocity and heat transfer signals in a region of high coherence

(*d*) were calculated for each structure at each time instance. This information was then combined into the four-dimensional histogram shown in Figure 2.9 below.

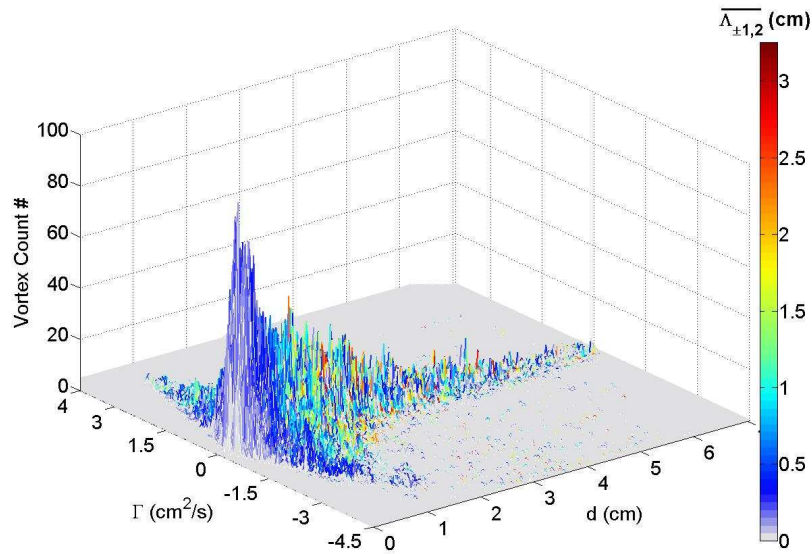


Figure 2.9: Histogram of coherent structures identified in the stagnation region and corresponding physical properties

Several immediate observations can be made from Figure 2.9. First, it is clear that a large degree of symmetry exists in the flow field. Similar numbers of coherent structures exist with either positive or negative circulation (spin). This is a direct result of the imposed grid generated turbulence which is on average homogeneous

and isotropic. As seen in flow field animations, spin symmetry is also manifest in the presence of counter-rotating vortex pairs which form near the stagnation plate surface. Secondly, the number of coherent structures increases upon approaching the stagnation plate surface, with more structures of weaker circulation strength and smaller integral length scales. The concentration of small, weak coherent structures reaches a peak just outside the laminar boundary layer thickness of $\delta_{Lam} = 0.03cm$ cm and decreases thereafter. The increase in smaller, weaker coherent structures near the stagnation plate surface is thought to be primarily due to the generation of secondary flow structures. Thirdly, a large percentage of the identified structures have core-to-plate distances small enough, and integral length scales large enough, to completely penetrate the laminar boundary layer. These structures may be responsible for heat transfer augmentation as they can bring cold freestream fluid directly into the heated stagnation surface. This would be in agreement with the results of the coherence analysis. Finally, there appears to be a general decrease in integral length scale upon approaching the stagnation plate surface. This decrease in integral length scale is concurrent with the sharp increase in circulation strength for structures which reside in the "wings" or side regions of the histogram. To clarify this point a projected view of Figure 2.9 is shown below in Figure 2.10. Note that a similar behavior for stream-wise integral length scale and fluctuating velocity was noted earlier in the time-averaged data of Figure 2.6. The peak of the "wing" region in Figure 2.10 is also near $d \cong 3 * \delta_{Lam}$. As suggested by the time-averaged data in Figure 2.6 the increase

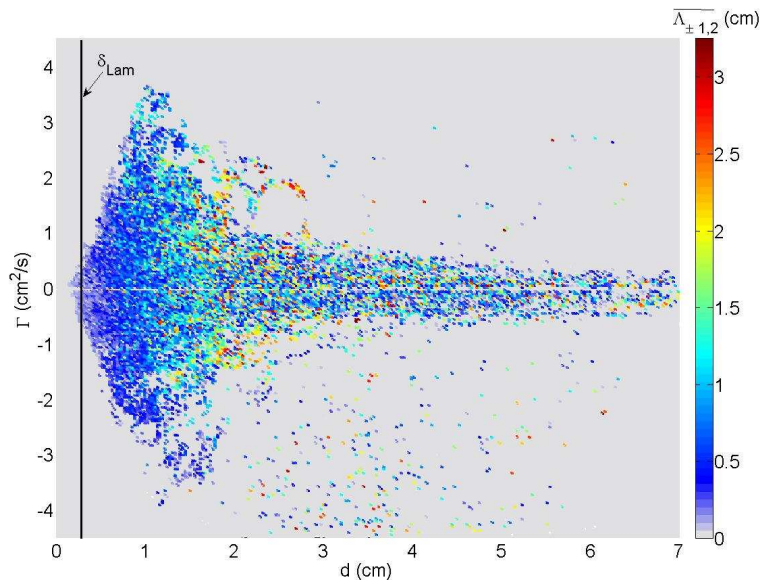


Figure 2.10: Behavior of coherent structure integral length scale and circulation with core-to-plate distance

in strength of coherent structures near the stagnation plate along with a decrease in integral length scale is consistent with the theory of vorticity amplification studied by Suter (15) and others as the mechanism leading to heat transfer augmentation in stagnating flows. Structures from the freestream, which are stretched by the mean flow strain rate around the stagnation plate, will increase in strength via conservation of angular momentum and decrease in length scale.

The coherent structure tracking algorithm was applied to the identified structures in an attempt to both quantify the amplification of vorticity in the stagnation region and validate the mechanistic model presented in Section 2.5. Figure 2.11 shows the coherent structures tracked through time across the ROI of the TRDPDV data for

a representative trial. The heat flux sensor location is marked on the center, right hand side of the image by a black dot. For a given time step the core location of a structure is marked by a contour color filled circle representing circulation strength. The average integral length scales are reflected in the size of each circle (These are not to scale for clarity).

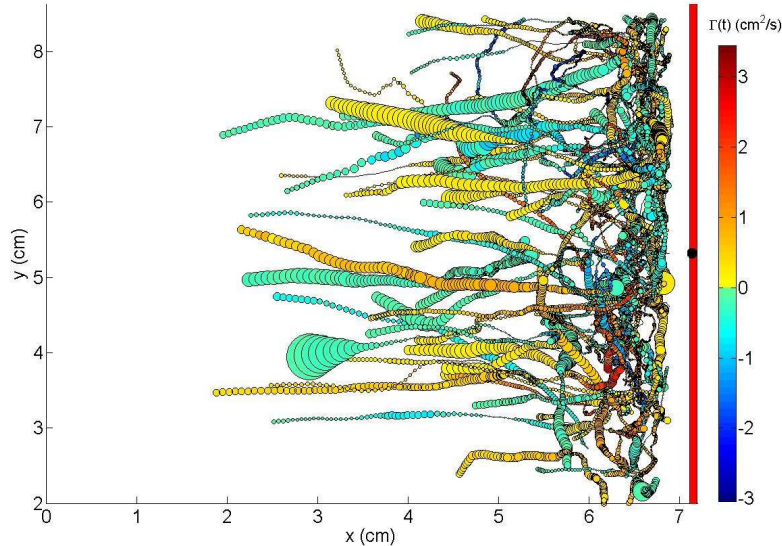


Figure 2.11: Coherent structure tracking results for a representative trial

Figure 2.11 reveals that a complex flow pattern exists near the stagnation region. Single coherent structures entering the stagnation region from the freestream (left to right in image) are clearly visible. Close inspection reveals that complex vortex structures, which may be paired (counter-rotating) or single, accumulate and translate across the stagnation plate surface. As mentioned earlier, single vortex structures typically induce a secondary flow near the stagnation plate in the form of a vortex with opposite rotational direction. It is also apparent that vortex stretching and amplification is present.

2.16 Validation of the Transient Mechanistic Model

Validation of the mechanistic model is provided in Figures 2.16(a-c) and 2.16(a-c). Both figures show an example of a coherent structure entering the stagnation region from the freestream which is approximately centered on the HFA sensing area and minimally influenced by surrounding vortex structures. From the coherence analysis, the model may only be expected to work well when the coherent structure's path passes within the region of highest coherence in front of the sensor. In this case a region centered on the sensor covering the entire width of the TRDPIV field-of-view and about 2.5cm tall should be the region of interest for model validation.

There are three plots contained in both Figures 2.16 and 2.16. The upper plot (a) is similar to Figure 2.11, providing the trajectory of the coherent structure through time. Note again that the contour color represents circulation strength and the size of the circle reflects integral length scale (not to scale). The center plot (b) shows selected physical properties of the tracked coherent structure through time. The lower plot (c) compares the transient heat transfer coefficient predicted using these properties in

conjunction with Eqns. 2.3-2.5, with the transient heat transfer coefficient measured experimentally by the HFA.

The first example in Figure 2.16(a) shows a coherent structure with clock-wise rotation enter the TRDPIV field-of-view with relatively large integral length scale and low circulation strength. As the structure approaches the plate, pronounced stretching and amplification occur for approximately 1.0 sec. The interplay of integral lengths scale and circulation strength is shown clearly in Figure 2.16(b). A gradual rise in the experimental, turbulent heat transfer coefficient is seen in Figure 2.16(c) to occur at 18.8 sec. As shown in Figure 2.16(a) this corresponds to the moment when the vortex structure first passes towards and turns abruptly away from the sensor. A second close passage at $t = 19.7$ sec. causes a second increase in heat transfer corresponding to the second peak in heat transfer seen in Figure 2.16(c). These motions serve to sweep cold freestream fluid into the laminar boundary layer region, thereby increasing heat transfer. The mechanistic model prediction using the coherent structure properties of Figure 2.16(b) is shown in red with the experimental data in Figure 2.16(c). The transient model prediction matches the experimental curve well in terms of magnitude and shape, but under-predicts the experimental turbulent heat transfer coefficient by around 20% over the first 1 – 1.5 seconds of identification and tracking. This reflects the fact that different coherent structures were still affecting the sensor during the initial approach of the coherent structure in Figure 2.16(a).

A slightly more complicated flow pattern is observed for the second example in Figure 2.16(a). In this case the coherent structure exists only in the near wall region and experiences large transverse flow motions. The first close passage of the structure at $t = 23.8$ sec. corresponds to the first, smaller peak in heat transfer in Figure 2.16(c). Note that circulation strength is minimal up to $t = 23.8$ sec. A return of the structure towards the sensor at $t = 25.7$ sec corresponds to the second, larger increase in heat transfer. This is due to the large increase in circulation strength shown in Figure 2.16(b). As the structure moves away heat transfer augmentation diminishes. Again the mechanistic model prediction in Figure 2.16(c) for the turbulent heat transfer coefficient is very close in shape and magnitude to that measured experimentally by the HFA. The validity of the model is further tested by examining the measured velocity $u_1(Surface, t)$ near the sensor surface and comparing it to the induced velocity, $u_\theta(t)$. This comparison is shown in Figure 2.16(b). The increase in circulation strength coincides with increased fluid velocity at the plate.

One final point worth may be made about this model. If it works well in predicting heat transfer augmentation for individual transient interactions, it would be expected to provide an accurate estimate of the time-averaged turbulent heat transfer. This is in fact the case as shown by the solid black lines in Figures 2.16(c) and 2.16(c) which are nearly identical to the overall time-averaged turbulent heat transfer denoted by the dashed blue lines.

2.17 Conclusions

This work successfully demonstrates the application of simultaneous TRDPIV and HFA measurements to the study of heat transfer in stagnating flows subject to freestream turbulence. These experimental studies confirm that coherent structures play an important role in the augmentation of heat transfer. Identifying and tracking these structures in time reveals a complex flow pattern in the stagnation region. Counter-rotating vortex pairs dominate the flow, along with a large number of weaker, smaller secondary flow structures. Calculation and examination of transient physical properties for the coherent structures (i.e. circulation strength, integral length scale, and proximity to the surface) makes it apparent that stretching and amplification of vorticity play an important role in defining the structure of the near-wall

flow and the augmentation of heat transfer. In agreement with current theory it is surmised that the divergence of streamlines near the stagnation plate surface acts to stretch and amplify the vorticity of coherent structures entering from the freestream. A hypothetical, mechanistic model which incorporates the aforementioned physical properties predicts both transient and time-average turbulent heat transfer coefficients, matching experimental values very well. Future research will include refined versions of the analytical techniques presented here and simultaneous flow and heat transfer measurements along the entire stagnation line.

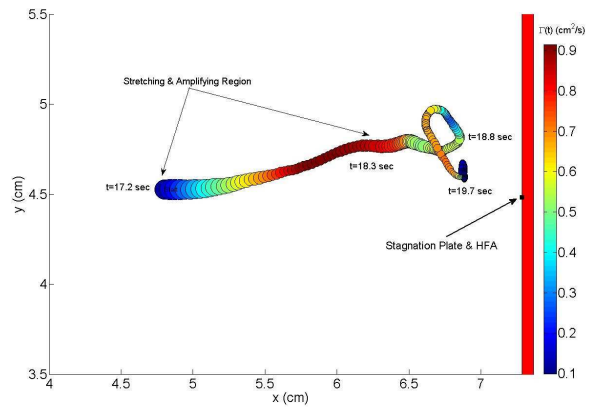
2.18 Acknowledgements

The principle author would like to thank several AETHER laboratory members including David Hubble for invaluable assistance during experimentation and Christopher Weiland for vortex identification code development and assistance with analysis. We also wish to thank program manager Patrick Phelan for supporting this research under contract number CTS-0423013 with the National Science Foundation.

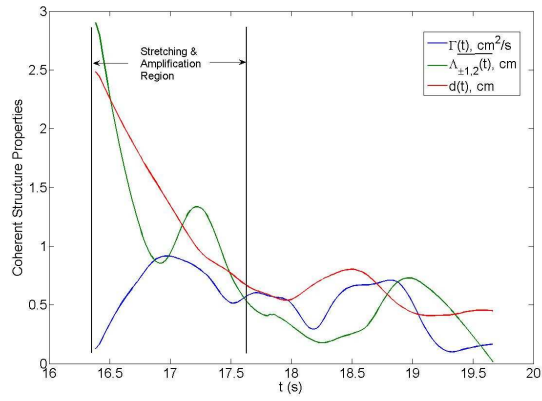
2.19 References

1. "Die Grenzschicht an einem in den gleichförmigen Flüssigkeitsstrom eingetauchten geraden Kreisylinder". Hiemenz, K. 1911, Dinglers Polytechnic J., Vol. 326, p. 321.
2. Goldstein, S. Modern Developments in Fluid Dynamics. Oxford : Clarendon Press, 1938.
3. "The Effect of Freestream Turbulence on Heat Transfer Rates". Kestin, J. NY : Acad. Press, 1966, Advances in heat transfer, Vol. 3, pp. 1-32.
4. "Enhancement of Stagnation-Line Heat Transfer by Turbulence". Kestin, J., and Wood, R. T. 1969, Progress in Heat and Mass Transfer, Vol. 2.
5. "Effects of Turbulence on Laminar Skin Friction and Heat Transfer". Smith, M. C. and Kuethe, A. M. 1966, Physics of Fluids, Vol. 9.
6. "The effect of turbulence on heat transfer from heated cylinders". Lowery, G.W. and R.I. Vachon. 1975, Int. J. Heat Mass Transfer, Vol. 18, pp. 1229-1242.
7. "Analytical Study of Freestream Turbulence Effects on Stagnation Point Flow and Heat Transfer". Traci, R. M. and D.C. Wilcox. 1974. Proc. AIAA 7th Fluid and Plasma Dynamics Conference. Paper No. 74-515.
8. "Effects of turbulence intensity and integral length scale of a turbulent free stream on forced convection heat transfer from a circular cylinder in cross flow". Yardi, N.R. and S.P. Sukhatme. Toronto, Canada : s.n., 1978. Proc. Int. Heat Transfer Conf. 6th Aug. 7-11.
9. "An Account of Free-Stream-Turbulence Length Scale on Laminar Heat Transfer". Dullenkopf, K. and R.E. Mayle. 1995, J. Turbomachinery, Vol. 117.
10. "Influence of Turbulence Parameters, Reynolds Number, and Body Shape on Stagnation-Region Heat Transfer". Van Fossen, G.J., Simoneau, R.J., and C.Y. Ching. 1995, J. Heat Transfer, Vol. 117.
11. "Measurements of the Influence of Integral Length Scale on Stagnation Heat Transfer". Van Fossen, G.J., and C.Y. Ching. 2, 1997, Int. J. Rotating Machinery, Vol. 3, pp. 117-132.
12. "The role of turbulence length scale and turbulence intensity on forced convection from a heated horizontal circular cylinder". Sak, C., Liu, R., Ting, D.S.-K., and G.W. Rankin. Exp. Thermal and Fluid Science, Vol. 31, pp. 279-289.
13. "Effect of turbulent integral length scale on heat transfer around a circular cylinder placed cross to an air flow". Peyrin, F. and A. Kondjoyan. 2002, Exp. Thermal and Fluid Science, Vol. 26, pp. 445-460.
14. "On the sensitivity of heat transfer in the stagnation-point boundary layer to free-stream vorticity". Suter, S.P., Maeder, P.F., and J. Kestin. 4, 1963, J. Fluid

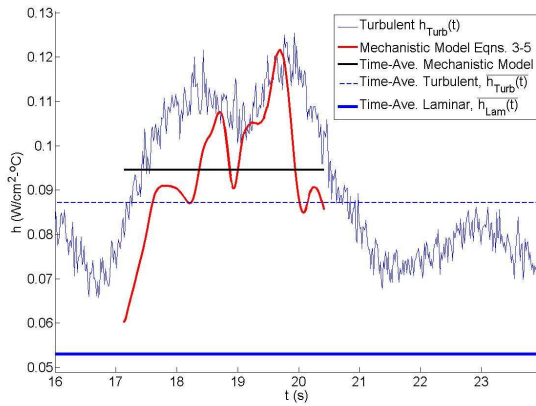
- Mech., Vol. 16, pp. 497-520.
15. "Vorticity amplification in stagnation-point flow and its effect on heat transfer". Suter, S.P. 1965, J. Fluid Mech., Vol. 23, pp. 513-534.
 16. "Influence of Inflow Disturbances on Stagnation-Region Heat Transfer". Bae, S., Lele, S.K., and Sung, H.J. 2000, Trans. AMSE, Vol. 22, pp. 258-265.
 17. "Direct Numerical Simulation of Stagnation Region Flow and Heat Transfer with Free-Stream Turbulence". Bae, S., Lele, S.K., and Sung, H.J. 6, 2003, Physics of Fluids, Vol. 15, pp. 1462-1484.
 18. "Distortion of upstream disturbances in a Hiemenz boundary layer". Zhongmin, X., and S. Lele. 2004, J. Fluids Mech., Vol. 519, pp. 201-232.
 19. "An investigation of vorticity amplification in stagnation flow". Sadeh, W., Suter, S., and Maeder, P. 1970 : s.n., ZAMP, Vol. 21, pp. 717-741.
 20. "Stretching of Freestream Turbulence in the Stagnation Region". Wei, C., and Miao, J. 9, 1992, AIAA Journal, Vol. 30, pp. 2196-2203.
 21. "Characteristics of Stretched Vortical Structures in Two-Dimensional Stagnation Flow". Wei, C., and Miao, J. 11, 1993, AIAA Journal, Vol. 31, pp. 2075-2082.
 22. "Vortex structure and heat transfer in the stagnation region of an impinging plane jet (simultaneous measurements of velocity and temperature fields by digital particle image velocimetry and laser-induced fluorescence". Sakakibara, J., Hishida, K., and Maeda, M. 13, 1997, Int. J. Heat Mass Transfer, Vol. 40, pp. 3163-3176.
 23. "Experimental Measurements and Modeling of the Effects of Large-Scale Freestream Turbulence on Heat Transfer". Nix, A. C., Diller, T.E., and W.F. Ng. 2007, ASME J. Turbomachinery, Vol. 129, pp. 542-550.
 24. "An Investigation of Flow Through Screens". Baines, W.D. and E.G. Peterson. July 1951, ASME J. Heat Transfer, pp. 467-480.
 25. Hinze, J. O. Turbulence. NY : McGraw-Hill, Inc., 1975.
 26. Ewing, J. "Development of a Direct-Measurement Thin-Film Heat Flux Array". Master's Thesis. Blacksburg, VA : Virginia Polytechnic Institute & State University, 2006.
 27. "The Convection Calibration of Heat Flux Sensors in Shear and Stagnation Flow". Gifford, A., Hoffie, A., T. E. Diller, and S. Huxtable. 2008, To Be Published.
 28. Raffel, M., Willert, C., and J. Kompenhans. Particle Image Velocimetry. s.l. : Springer-Verlag, 1998.
 29. "Fundamentals of digital particle image velocimetry". Westerweel, J. 1997, Meas. Sci. Technol., Vol. 8, pp. 1379-1392.
 30. Eckstein, A. "Development of Robust Correlation Algorithms for Image Velocimetry using Advanced Filtering". [Master's Thesis]. Blacksburg, VA : Virginia Polytechnic Institute & State University, 2007.
 31. "Low-Dimensional Modeling of Turbulence Using the Proper Orthogonal Decomposition: A Tutorial". Smith, T., Moehlis, J. and Holmes, P. 2005, Nonlinear Dynamics, Vol. 41, pp. 273-307.
 32. "A General Classification of Three-Dimensional Flow Fields". Chong, M.S., Perry, A.E., and B.J. Cantwell. 5, 1990, Phys. Fluids A, Vol. 2.
 33. "Visualizing Features and Tracking Their Evolution". Samtaney, R., Silver, D., Zabusky, N. and Cao, J. 7, 1994, Computer, Vol. 27, pp. 20-27.



(a)

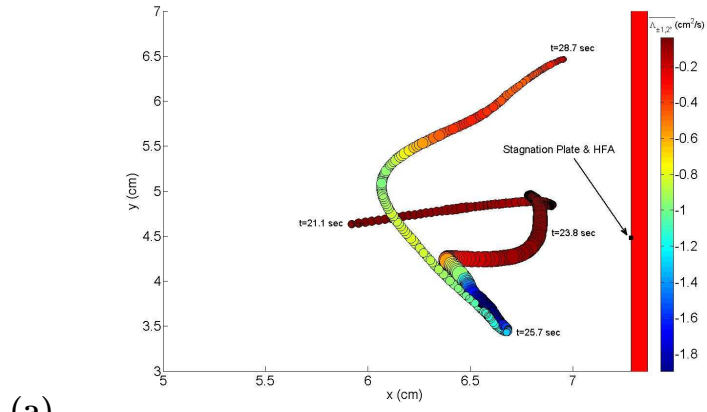


(b)

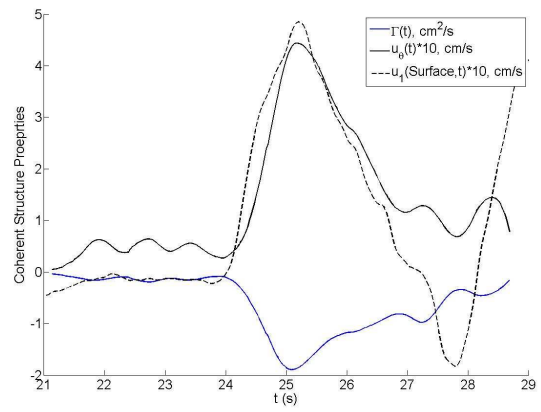


(c)

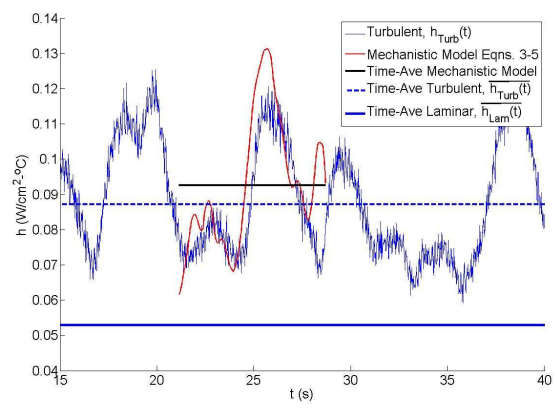
Figure 2.12: Example #1: Mechanistic Model Validations for Stream-wise Coherent Structure Interaction



(a)



(b)



(c)

Figure 2.13: Example #2: Mechanistic Model Validations for a Complicated Coherent Structure Interaction

Chapter 3

Further Validation of the Mechanistic Model for Heat Transfer Augmentation

3.1 Introduction

In Chapter 2 a mechanistic model was developed to predict the transient heat transfer resulting from coherent structure interactions in the stagnation region. The model is repeated here in Equations 3.1-3.3 for reference:

$$h_{Turb}(t) = h_{Lam}(t) + \Delta h_{Turb}(t)$$
$$where : \Delta h_{Turb}(t) = \frac{k}{\Lambda(t)\sqrt{\pi}} Pr^{0.5} Re_{\Lambda}(t)^{0.5} \quad (3.1)$$

The Reynolds number is based on the induced velocity magnitude at the plate surface due to the coherent structure and the integral length scale:

$$Re_{\Lambda} = \frac{\Lambda(t)u_{\theta}(t)}{\nu} \quad (3.2)$$

The induced velocity magnitude is calculated by approximating a structure as an infinite line vortex:

$$u_{\theta}(t) = \left| \frac{\Gamma(t)}{2\pi d(t)} \right| \quad (3.3)$$

Recall that validation of the mechanistic model was accomplished by examining a number of interactions where it appeared that only one coherent structure was responsible for the heat transfer augmentation. These interactions are shown in Figures 2.12 and 2.13 in Chapter 2. Based on the excellent agreement with the measured heat transfer, it appears that the model accurately captures the underlying interaction physics for single coherent structure interactions. Despite this success, the model represented in Equations 3.1-3.3 is incomplete on physical grounds. As evidence by TRPDIV animations, any number of coherent structures may act simultaneously to change the local flow properties, and hence heat transfer, at a point on the stagnation surface. Therefore, attempts have been made to modify and re-validate the mechanistic model. As discussed in Section 3.2, a cumulative induced velocity method is developed that calculates the induced velocity contributions from any number of

coherent structures simultaneously. Results from the model using this approach are presented in detail in Section 3.3. Finally, a trend analysis approach to validation of the mechanistic model is presented in 3.4. In this case the bulk behavior of the coherent structures near the HFA are examined to reveal trends in physical behavior.

3.2 Modified Mechanistic Model Using A Cumulative Induced Velocity Method

As discussed previously, a multitude of coherent structures may surround the HFA measurement location at any given time instance. Therefore, the induced velocity at the stagnation surface will be a resultant of contributions from each coherent structure. Accounting for this cumulative induced velocity within the mechanistic model is not straight-forward. For instance, one must recognize that the flow field in the stagnation region must obey the laws of fluid dynamics. i.e. every coherent structure will have some influence, however large or small, on every other coherent structure. It is beyond the scope of this research to devise an analytical model for the velocity distribution at the stagnation surface that accounts for these complex structure-to-structure interactions. Therefore, several assumptions have to be made in order to proceed with modifications to the mechanistic model. The first assumption must be that all structures act independently of one another. This means that an induced velocity from each structure may be calculated based on its specific properties at a given time instance. The individual velocities from all structures at the given time instance can then add and subtract from one another at a point in front of the HFA to produce a net or cumulative velocity. This may not be a bad assumption if the structures in the flow field are sufficiently separated from one another in space. Another significant assumption involves the integral length scale used in the modified version of the mechanistic model. At each time instance the cumulative velocity calculation will account for each coherent structure's core-to-plate distance and circulation strength, but no "cumulative" integral length scale is forthcoming. To remedy this problem the mean integral length scale of all the coherent structures present at each time instance is used. Figure 3.1 shows schematically how the cumulative velocity is calculated under these key assumptions.

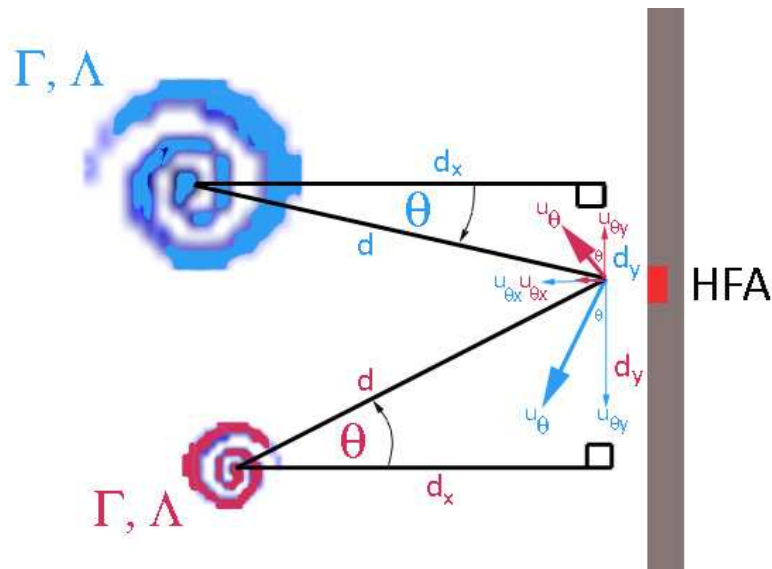


Figure 3.1: Schematic of Cumulative Induced Velocity Method

The cumulative velocity calculation is relatively straightforward and is done at each time instance for each tracked coherent structure. Following calculation of the induced velocity magnitude, u_θ , using Equation 3.3, the velocity components, u_{θ_x} and u_{θ_y} , may be determined for each individual coherent structure. The component calculations first require determination of the approach angle θ shown in Figure 3.1. This angle may be determined easily from trigonometric relationships, depending on the rotational orientation and quadrant location of the coherent structure. As such, there are four possible scenarios for a given coherent structure: 1) Upper quadrant and counter-clockwise spin, 2) Upper quadrant and clockwise spin, 3) Lower quadrant and counter-clockwise spin, and 4) Lower quadrant and clockwise spin. The calculation of θ and the velocity components for each case is summarized in Table 3.1 for reference.

Coherent Structure Flow Scenario	u_θ	θ	u_{θ_x}	u_{θ_y}
1	$\frac{\Gamma}{2\pi d}$	$\cos^{-1}\left(\left \frac{d_x}{d}\right \right)$	$u_\theta \cos \theta$	$u_\theta \sin \theta$
2	$\frac{\Gamma}{2\pi d}$	$\cos^{-1}\left(\left \frac{d_x}{d}\right \right)$	$-u_\theta \cos \theta$	$-u_\theta \sin \theta$
3	$\left \frac{\Gamma}{2\pi d}\right $	$\cos^{-1}\left(\left \frac{d_x}{d}\right \right)$	$-u_\theta \tan \theta$	$\sqrt{u_\theta^2 - u_{\theta_x}^2}$
4	$\left \frac{\Gamma}{2\pi d}\right $	$\cos^{-1}\left(\left \frac{d_x}{d}\right \right)$	$u_\theta \tan \theta$	$-\sqrt{u_\theta^2 - u_{\theta_x}^2}$

Table 3.1: Induced Velocity Component Calculations

3.3 Modified Mechanistic Model Validations

The calculations shown in Table 3.1 were performed for each tracked coherent structure, at each time instance, for the TRDPIV data set described previously in Chapter 2. Using vector addition two cumulative velocity components were calculated for the N coherent structures present at each time instance. These are calculated as

$$u_{\theta_x-C}(t) = \sum_{i=1}^N u_{\theta_x-i} \quad (3.4)$$

$$u_{\theta_y-C}(t) = \sum_{i=1}^N u_{\theta_y-i} \quad (3.5)$$

A new overall velocity magnitude is then

$$u_{\theta-C}(t) = \sqrt{u_{\theta_x-C}(t)^2 + u_{\theta_y-C}(t)^2} \quad (3.6)$$

Figures 3.2-3.4 compare the transient heat transfer coefficients found using the modified mechanistic model to the heat transfer coefficient measured by the HFA. To generate the three predicted heat transfer curves the cumulative induced velocities, u_{θ_x-C} , u_{θ_y-C} , and $u_{\theta-C}$ were used in turn in Equation 3.2 for the Reynolds number. As mentioned earlier the mean integral length scale of all coherent structures present at a given time instance was used in Equations 3.1 and 3.2. The presence of time lag between the predicted and measured heat transfer coefficients makes it difficult to make a direct visual comparison, so some time lag must be estimated. This was accomplished by performing a general cross-covariance between the two signals and identifying the lag associated with the highest normalized cross-covariance. The calculated time lags were approximately 0.65 seconds for model predictions using u_{θ_y-C}

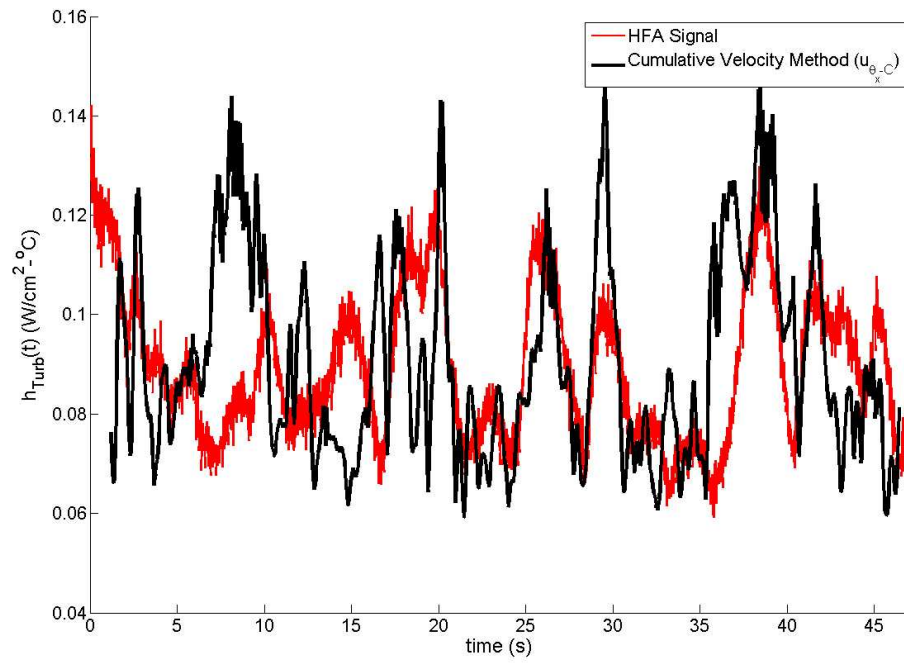


Figure 3.2: Mechanistic Model Predictions Using the Cumulative Induced Velocity Method: u_{θ_x-C}

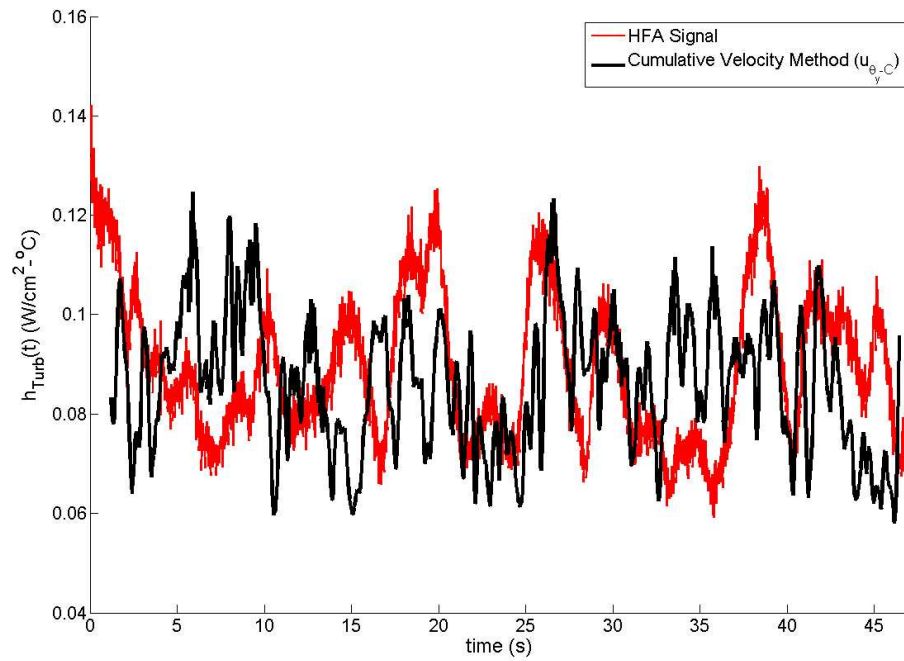


Figure 3.3: Mechanistic Model Predictions Using the Cumulative Induced Velocity Method: u_{θ_y-C}

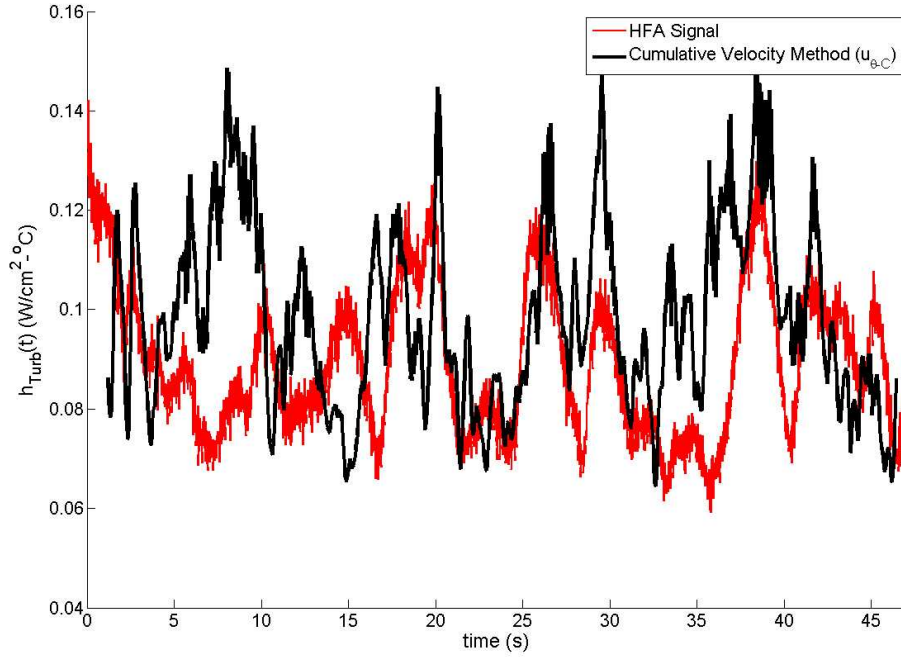


Figure 3.4: Mechanistic Model Predictions Using the Cumulative Induced Velocity Method: $u_{\theta-C}$

and 1.3 seconds for model predictions using u_{θ_x-C} and $u_{\theta-C}$, respectively. These values are reflected in the aforementioned plots.

After careful examination of Figures 3.2-3.4 it appears that the modified mechanistic model captures the measured heat transfer both in terms of magnitude and general trend over time. However, there are still regions where no sound agreement is reached. For instance, poor agreement between model and experiment is seen from $t = 5 - 10$ seconds for predictions using u_{θ_x-C} . This may be due to limitations in the model as discussed previously or an unidentified calculation error. Comparison of the predictions using the two induced velocity components reveals that the use of u_{θ_y-C} tends to under-predict the measured heat transfer, whereas u_{θ_x-C} tends to over-predict the measured heat transfer but to a better degree of accuracy. The fact that predictions using u_{θ_x-C} work so well is consistent with previous observations that the fluctuating velocity component along the x-direction has high levels of coherence with the measured heat transfer. This is also consistent with the hypothesis that motion *towards* the stagnation surface brings cold fluid directly into the heated boundary layer region, augmenting heat transfer. Motion *along* the surface in the y-direction would move fluid that is already heated compared to the surface temperature across the HFA, and hence not augment heat transfer as much.

To quantify the accuracy of the mechanistic model predictions shown in Figures 3.2-3.4, a scatter plot of predicted versus measured heat transfer coefficient was generated using the values shown in the figures at each time instance. A representative plot using $u_{\theta-C}$ is shown in Figure 3.5. Note that perfect agreement of the predicted heat transfer coefficient with the measured value should produce a 45° line which is shown in black. The data scatter tends to follow the 45° trend with some over-prediction evident at lower values of the measured heat transfer coefficient. Most data fits within a $\pm 15\%$ uncertainty band (red dashed lines) in the predicted heat transfer. As mentioned previously, attempts were made to quantify the time lag between the predicted and measured heat transfer coefficients. Since only one lag could be used,

regions where good agreement is evident, but not lag-adjusted properly, will increase the scatter in Figure 3.5. This may be the case from $t = 10 - 15$ seconds in Figure 3.4.

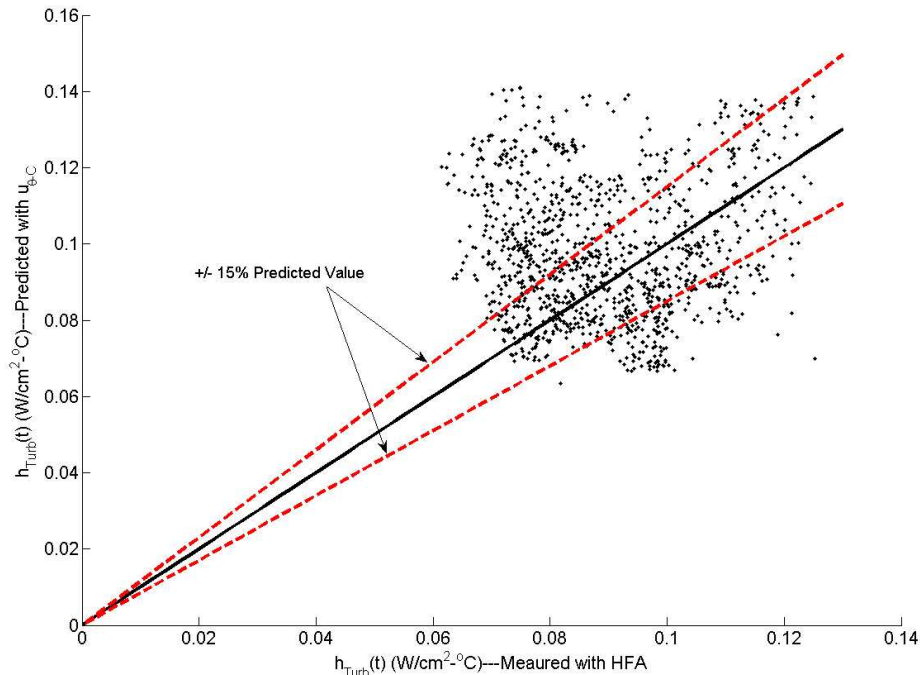


Figure 3.5: Accuracy of the Mechanistic Model Using $u_{\theta-C}$

3.4 Trend Analysis Validations

The underlying hypothesis for heat transfer augmentation via coherent structure interaction is that each structure brings cooler fluid from the freestream into the heated boundary layer region where conduction heat transfer occurs over a period of time. According to the mechanistic model in Equation 3.1, the amount of augmentation is moderated by the proximity of the structure to the surface, the strength of the structure, and its physical size. For a given core-to-surface distance, the general trend should be towards higher heat transfer augmentation at higher circulation strengths and lower integral length scales. This happens to be consistent with the vortex stretching and amplification mechanism first hypothesized by Sutera, which explains how coherent structures are affected by the mean flow strain rate around a stagnation body [1,2]. Hence, the basic form of the mechanistic model may be validated by looking for these specific trends in coherent structure behavior as a function of measured heat transfer in the vicinity of the HFA. This was accomplished by tabulating the properties of every coherent structure, along with the measured heat transfer coefficient, within a $2\delta_{Lam}$ long by δ_{Lam} wide rectangle in front of the HFA at every instance of time. The results of this analysis are shown in the three scatter plots in Figures 3.6-3.8.

Figure 3.6 shows a scatter plot of circulation magnitude versus measured heat transfer coefficient. It is readily apparent that higher circulation values tend to coincide with higher measured heat transfer coefficients. In fact, the mechanistic model assumes that $\Gamma \propto c * h_{Turb}^2$, where c is a constant of proportionality. To quantify the

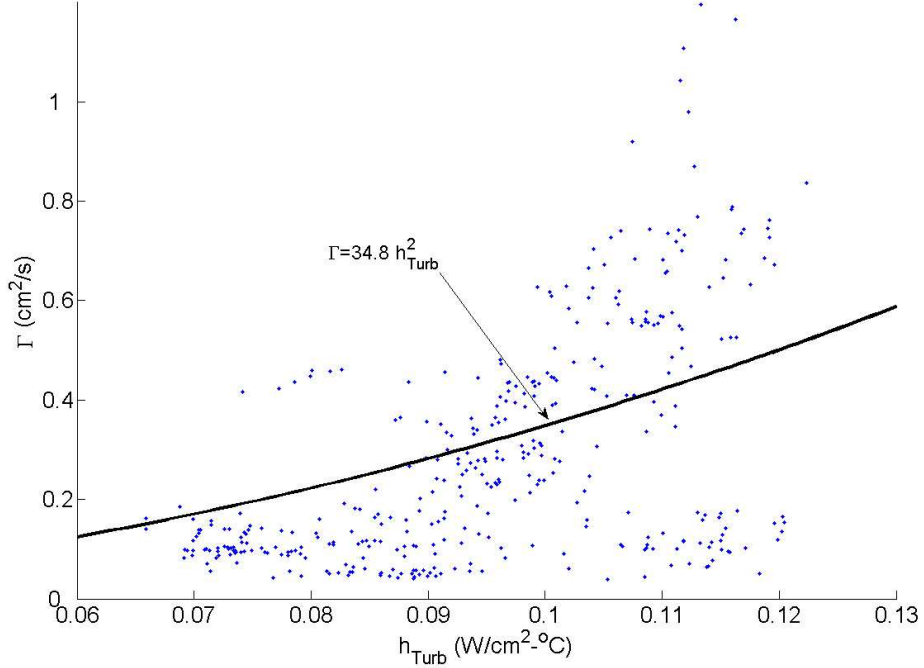


Figure 3.6: Coherent Structure Circulation Versus Measured Heat Transfer In the Vicinity of the HFA

trend in the data scatter, a least-squares fit of the data to a function of this form was calculated. This is shown as the black line across the data scatter with the estimated parameter $c = 34.8$. A similar scatter plot of integral length scale versus measured heat transfer coefficient is shown in Figure 3.7. Again, a trend exists in the scattered data. In this case it appears that decreasing integral length scale is concurrent with increasing values of the heat transfer coefficient. The mechanistic model assumes $\Lambda \propto d * h_{Turb}^{-2}$, with a constant of proportionality d . This curve-fit is shown in black in Figure 3.7 with $d = 0.0083$. Finally, Figure 3.8 shows the corresponding vortex Reynolds number versus measured heat transfer. The trend in Reynolds number is quite pronounced and captures the effects of integral length scale, circulation, and core-to-surface distance simultaneously. In accord with the mechanistic model, higher Reynolds numbers correspond to higher heat transfer levels. A least-squares curve fit of the form $Re_{\Lambda} \propto b * h_{Turb}^2$ is shown in black in Figure 3.8 with the constant of proportionality $b = 600$.

3.5 Conclusions

The incorporation of a cumulative induced velocity into the mechanistic model allows for surprisingly accurate predictions of the measured turbulent heat transfer coefficient, particularly with the x-component of the cumulative induced velocity. The mechanistic model is a valid tool for predicting transient and time averaged heat transfer in the stagnation region. Finally, the analysis of coherent structure properties and measured heat transfer near the HFA reveals trends in behavior that support the proposed form of the mechanistic model. Structures having higher circulation strength and smaller integral length scale tend to result in higher heat transfer. This is also consistent with the current theory of vorticity amplification in the stagnation

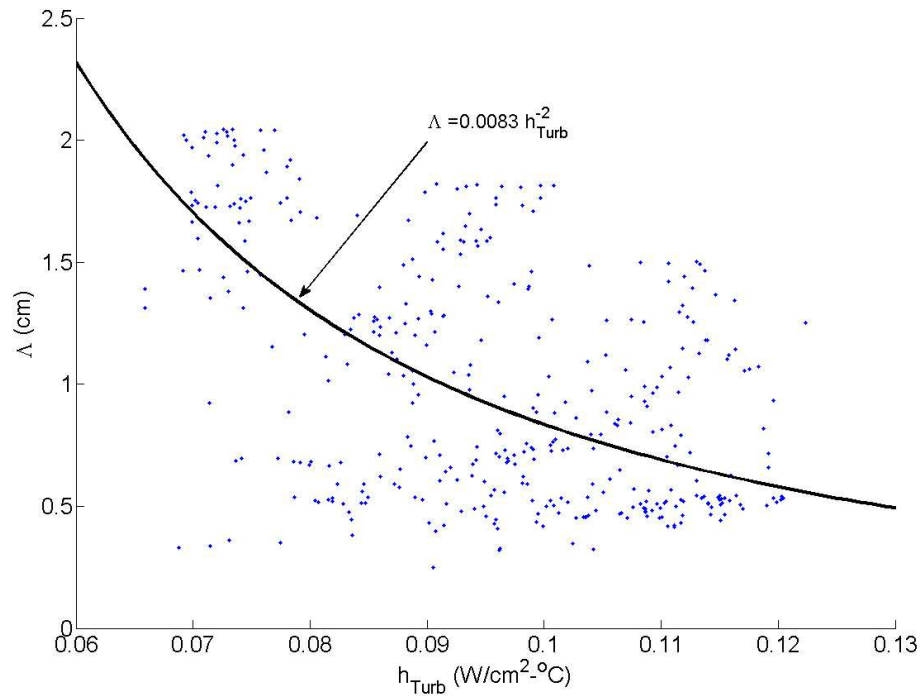


Figure 3.7: Coherent Structure Integral Length Scale Versus Measured Heat Transfer In the Vicinity of the HFA

region.

3.6 References

1. Suter, S.P., Maeder, P.F. and Kestin, J. "On the sensitivity of heat transfer in the stagnation-point boundary layer to free-stream vorticity," *J. Fluid Mech.*, Vol. 16, pp. 497, 1963.
2. Suter, S.P., "Vorticity amplification in stagnation-point flow and its effects on heat transfer," *J. Fluid Mech.*, Vol. 21, Part 3, pp. 513-534, 1965.

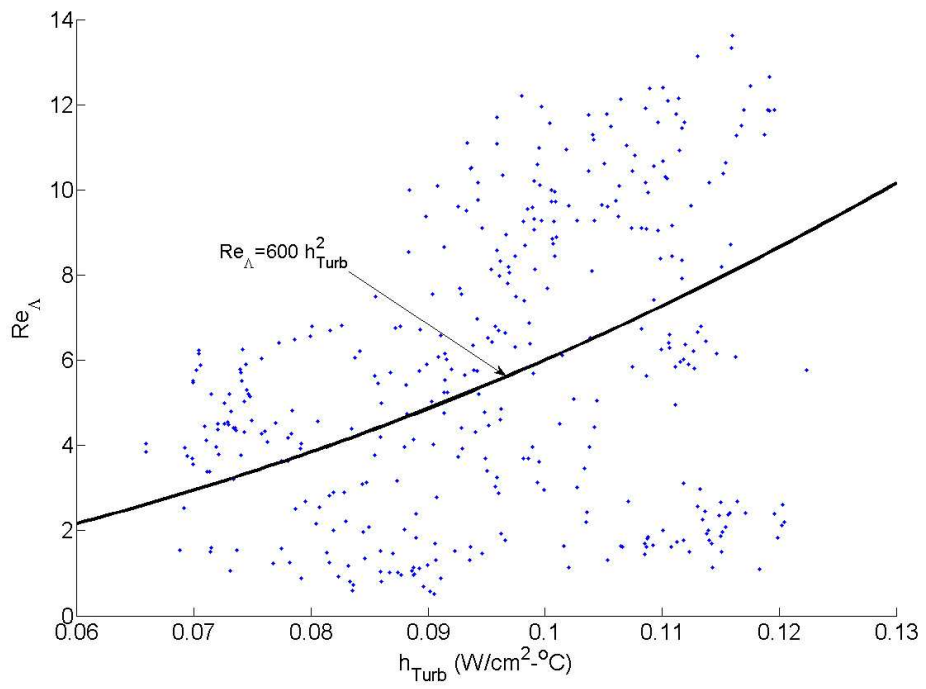


Figure 3.8: Coherent Structure Reynolds Number Versus Measured Heat Transfer In the Vicinity of the HFA

Part II
Related Studies

Chapter 4

A Durable Heat Flux Sensor for Extreme Temperature and Heat Flux Environments

This chapter is comprised of sections from AIAA Journal of Thermophysics and Heat Transfer Paper No. *AIAA – T – 3288* submitted on November 20, 2008. Acceptance of this paper for publication is still pending.

4.1 Abstract

This paper reports on the development and evaluation of a novel heat flux sensor, the High Temperature Heat Flux Sensor (HTHFS), capable of long term operation at temperatures and heat flux levels in excess of $1050\text{ }^{\circ}\text{C}$ and $10\text{--}13\text{W}/\text{cm}^2$, respectively. The current sensor configuration utilizes Type-k thermocouple materials in a durable welded thermopile arrangement contained within a surface-mountable high temperature housing. The steady state sensitivity of the design is predicted using a simplified one-dimensional thermal resistance. The design performance of a prototype sensor is validated using both conduction and convection heat transfer calibration facilities. The average experimental values of the sensitivity are $623.2 \pm 39.5\mu\text{V}/\text{W}/\text{cm}^2$ and $579.3 \pm 29.4\mu\text{V}/\text{W}/\text{cm}^2$ in conduction and convection, respectively. These calibration results compare very well with the predicted sensitivity. Minimal dependence on heat transfer coefficient is found in convection. Prolonged thermal cycling of the sensor using a high temperature kiln and a propane torch apparatus demonstrates survivability near the maximum temperature of the thermoelectric materials with negligible oxidation or loss of calibration.

4.2 Nomenclature

a	=	surface area in principle direction of heat transfer
α	=	thermal diffusivity
A	=	thermoelectric element A
B	=	thermoelectric element B
B_e	=	bias error
Cond	=	conduction designation
Conv	=	convection designation

δ	=	sensor thickness in principle direction of heat transfer
h	=	heat transfer coefficient
ins	=	insulation designation
j	=	heated air jet designation
k	=	thermal conductivity
n	=	# sensor components
N	=	# thermoelectric element pairs
P_e	=	precision error
q''	=	heat flux
Ref	=	first reference sensor designation
R''	=	thermal resistance
S	=	sensor sensitivity
S_{AB}	=	Seebeck coefficient for thermoelectric elements A and B
t	=	HTHFS sensor designation
t_s	=	thermal response time
T	=	temperature
U	=	measurement uncertainty
V	=	thermoelectric output voltage
W	=	weld designation
X_i	=	ith independent measurement variable

4.3 Introduction

The measurement of heat flux in extreme environments is a challenging task. Take for instance the high temperature turbulent flow environments found in modern turbomachinery or the searing temperatures, high heating rates, and aerodynamic loads on a spacecraft's thermal protection system. Measurement of heat flux in these conditions is notoriously difficult since most sensors have trouble surviving long enough to provide useful and cost-effective engineering data [1]. Recently the High Temperature Heat Flux Sensor (HTHFS) was prototyped and characterized to address the difficulty in making accurate, long duration heat flux measurements under these types of conditions [2]. The focus of the current study is to detail the design and performance of the latest version of the HTHFS.

4.4 Heat Flux Sensor Design

The current version of the HTHFS design is shown schematically in Figure 1. The sensor is composed of alternating thermo-electric element pairs connected electrically in series with electrical insulators isolating each element. An all-welded construction makes this thermopile simple and robust. As shown in Figure 1, the thermopile is set securely in a high temperature metal housing with potting material to create smooth mounting surfaces. Four bolts may be used in conjunction with thermal adhesive to flush-mount and secure the sensor to the measurement surface. Thermally shielded wires carry the heat flux and sensor surface temperature signals safely to a data acquisition system or other voltage sensing device.

When the HTHFS is affixed properly to a measurement surface, any heat flux applied to the surface will result in a temperature gradient across the effective thermal resistance of the thermopile. The temperature gradient serves to generate a voltage

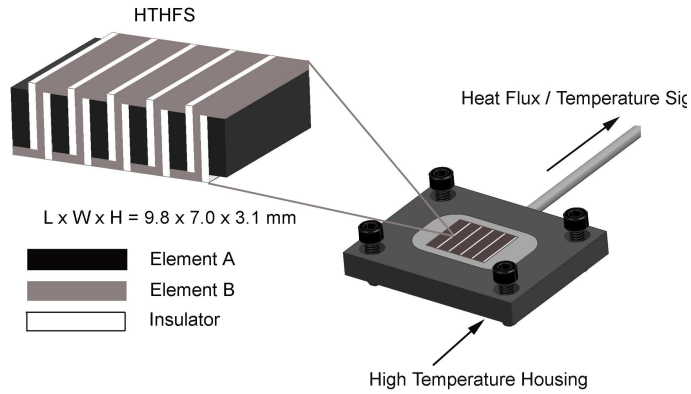


Figure 4.1: Surface mountable HTHFS with High Temperature Housing

which may be calibrated directly to the amount of applied heat flux. The voltage output (sensitivity) is scalable based on the number of thermoelectric element pairs and the Seebeck coefficient of thermoelectric element pair. The novel use of the thermopile as the thermal resistance layer is the fundamental difference between the HTHFS and most differential heat flux sensors that have been developed over the years [1]. Traditional differential heat flux sensors use a separate thermal resistance layer to create a temperature drop across the sensor. The temperature gradient is measured separately using thermocouple pairs or resistance-temperature detectors. This leads to added complexity, cost, and in some cases decreased reliability. A review of potential thermo-electric alloys was completed prior to constructing the high temperature version of the HTHFS. The results are tabulated in Table 4.1[3-5]. It is clear in examining Table 4.1 that a wide variety of HTHFS configurations are possible with extremely high operating temperatures. Standard Type-K materials were utilized for the current sensor due mainly to the high Seebeck coefficient, high temperature rating ($> 1000^{\circ}C$), durability, and relatively low cost.

Element #	Metal/ Alloy	Solidus/Melt $^{\circ}C$	Element A	Element B	$S_{AB} \mu V/^{\circ}C$
1	Alumel	1398	3	1	34.0
2	Copper	1085	4	1	40.0
3	Constantan	1171	3	2	39.4
4	Chromel	1426	5	2	22.1
5	Nickel	1452	7	2	6.70
6	Palladium	1553	4	3	60.1
7	Platinum	1768	5	3	20.5
8	Platinum/15%Iridium	1552	7	3	35.9
9	Platinum/13%Rhodium	1771	7	5	15.4
10	Platinum/1%Rhodium	1771	8	6	42.6
11	Platinum/5%Molebdenum	1770	9	10	40.7
12	Platinum/0.1%Molebdenum	1770	11	12	99.9

Table 4.1: Maximum Temperatures and Seebeck Coefficients Near Room Temperature

The electrical insulator, which is sandwiched between the thermo-electric elements, has to provide the same high temperature capability with a particular emphasis on survivability under thermal stress. A survey of potential insulators was completed with preference given to fire-cured ceramic pastes and thin ceramic plates composed primarily of aluminum oxide. Because the size of the thermopile and electrical insulators are arbitrary the HTHFS may also be scaled down to provide high

frequency response which is essential to capture transient events such as shock wave passage or freestream turbulence interactions. The current HTHFS size is Length x Width x Height = $9.0 \times 7.0 \times 3.1 \text{ mm}$. An acceptable estimate of thermal time response for a surface mounted heat flux sensor with a proper heat sink is given by Hager [6] as a ratio of sensor thickness, squared and the effective thermal diffusivity of the sensor, :

$$t_s = 1.5 \frac{\delta_t^2}{\alpha} \quad (4.1)$$

Using the thermal properties and size of the current HTHFS a thermal response time of roughly 2.0 seconds is obtained. This gives a frequency response on the order of 0.5 Hz . While this is considered to be too low for capturing fast transients it is clear that only a modest decrease in the thickness of the sensor can greatly increase the frequency response.

4.5 Theoretical HTHFS Sensitivity

Prediction of the sensitivity of the HTHFS is based on a simple heat transfer analysis using Fourier's Law and a thermal resistance model. Prediction of the sensitivity requires mathematical expressions for the voltage generated across the sensor under operating conditions, along with the heat flux through the sensor. As shown in Figure 4.1 the sensor consists of n_A and n_B thermoelectric elements in a thermopile arrangement creating $N = (n_A + n_B)/2$ pairs. With an applied heat flux a temperature gradient, $T = (T_2 - T_1)$, exists across the thermal resistance, R_t'' , of the sensor elements. In this case T_2 and T_1 are the top and bottom surface temperatures of the gage respectively. Both surfaces are assumed isothermal for analysis purposes. This temperature gradient generates a thermoelectric voltage, V_t , which is calculated according to the following equation:

$$V_t = NS_{AB}\Delta_T = NS_{AB}(T_2 - T_1) \quad (4.2)$$

where S_{AB} is the nominal Seebeck Coefficient for the thermoelectric alloys used in this study. The heat flux through the sensor is given by Equation 4.3

$$q_t'' = \frac{(T_2 - T_1)}{R_t''} \quad (4.3)$$

where R_t'' is the thermal resistance in the principle direction of heat transfer. Using the configuration of the HTHFS shown in Figure 4.1 a simplified one-dimensional thermal resistance model was constructed to estimate R_t'' .

As shown in Figure 5.1 the thermal resistance model consists of three distinct layers situated in series across the thickness of the HTHFS. Isothermal surfaces are assumed on the top and bottom surfaces and between each layer. Given the HTHFS materials and design it is assumed that parallel conduction is dominant in all three layers with adiabatic boundaries between elements. The overall thermal resistance model is given by Equation 5.5:

$$R_t'' = a_t \left(n_A \left(\frac{k_A a_A}{\delta_A} \right) + n_{ins} \left(\frac{k_{ins} a_{ins}}{\delta_{ins}} \right) + n_B \left(\frac{k_B a_B}{\delta_B} \right) \right)^{-1} + 2a_t \left(\frac{n_B k_W a_W}{\delta_W} \right)^{-1} \quad (4.4)$$

The variables k , a , and δ are the thermal conductivity, surface area, and thickness in the principal direction of heat transfer. Subscripts A , B , t , Ins , and W denote Element A , Element B , HTHFS, Insulation, and Weld respectively. Finally, the

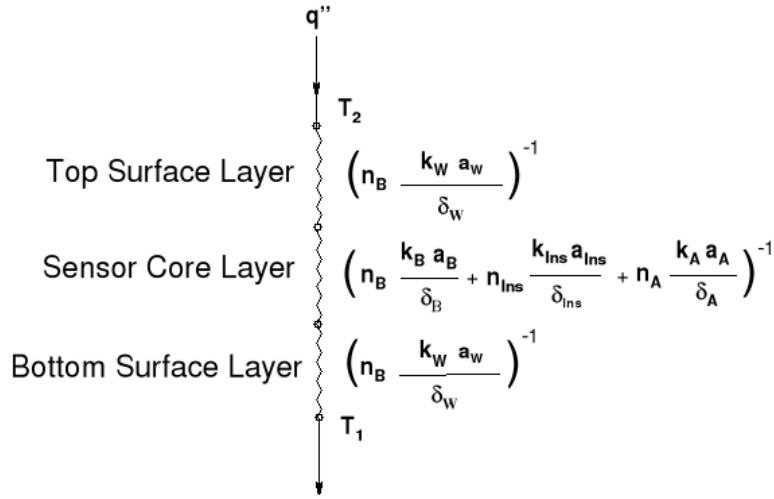


Figure 4.2: Simplified 1-D thermal resistance model of HTHFS

theoretical sensitivity for the HTHFS is found by division of Eq. 4.2 by Eq. 4.3. Hence,

$$S_{t-Cond} = \frac{V_t}{q_t''} = NS_{AB}R_t'' \quad (4.5)$$

Using Equation 5.5 the calculated value of the thermal resistance for the sensor evaluated in this study is $2.78cm^2 - ^\circ C/W$. It follows from Equation 4.5 that the theoretical conduction sensitivity of the HTHFS sensor is approximately $S_{t-Cond} = 558.8\mu V/W/cm^2$.

4.6 Heat Flux Sensor Calibrations

4.6.1 Introduction

The measurements obtained from a heat flux sensor are only as accurate as the method used in the sensor's calibration. There is currently no national standard for heat flux sensor calibration. However, several facilities have been developed by various private companies, government organizations, and universities. The general approach to heat flux calibration is to apply a repeatable reference heat flux to both the test sensor to be calibrated and a reference sensor. The reference sensor is assumed to accurately measure the reference heat flux. Sensitivity for the test sensor is obtained by simply dividing its voltage output by the heat flux measured by the reference sensor. The heat flux through the test and reference gages may be due to radiation, convection, conduction or mixed modes of heat transfer. It has been shown that the most useful calibration results are obtained when calibration is performed using the mode(s) of heat transfer the sensor will see in actual use [1]. The HTHFS sensor used in this study is first calibrated in conduction as a means of validating the analytical sensitivity calculations. The sensor is then calibrated in convection since this mode of heat transfer will be important in many of the proposed applications for the HTHFS.

4.6.2 Conduction Calibration

A new conduction calibration facility was recently developed in the AETHER laboratory at Virginia Polytechnic University to complement existing convection calibration facilities for shear and stagnation flow which are detailed in a work by Gifford, et.al.

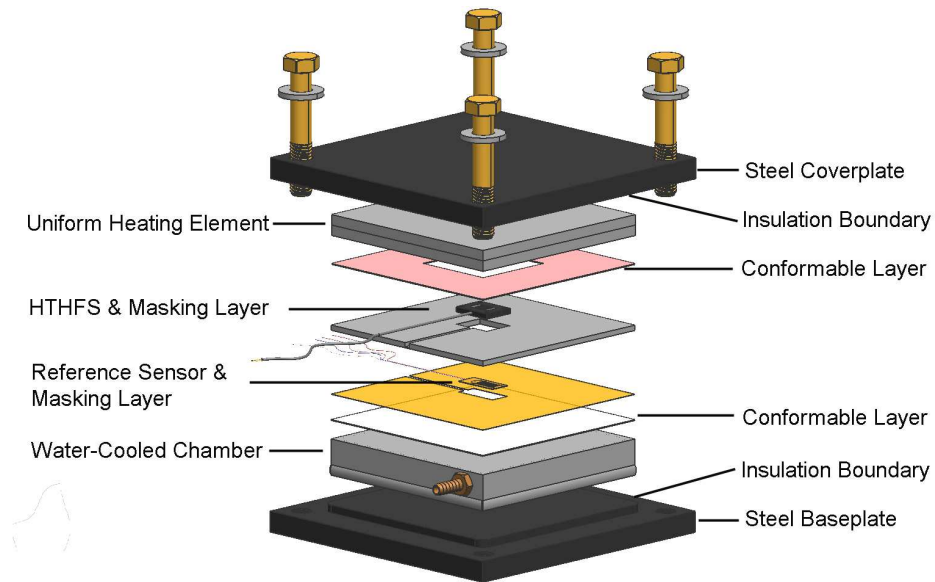


Figure 4.3: The Core of the Conduction Calibration Facility

[7]. The core of the conduction calibration facility is shown schematically in Figure 3. The conduction calibration facility is designed to supply a uniform heat flux through both the HTHFS sensor and a reference heat flux sensor. As shown in Figure 3 a uniform heat flux is supplied by a thin-film resistance heating element encased in two high thermal conductivity aluminum plates. The desired level of heat flux is set by a precision voltage regulator. Heat fluxes from $0.1 - 1.5 W/cm^2$ are available with this heating element. Thermal energy is carried out of the system using an internally water cooled aluminum chamber. Chilled water is circulated through the chamber using a high flow rate pump submerged in an ice-bath. A uniform heat flux is maintained through the HTHFS layer by surrounding the sensor with a metal mask made of material similar to the HTHFS housing material. A mask is also used around the reference heat flux sensor of similar composition and thickness. An RdF Corp. Micro-Foil heat flux sensor is used as the reference sensor in the conduction calibration facility. Contact resistance is minimized to a uniform level between the heated surface and the HTHFS as well as the cooled surface and the reference sensor via conformable layers of Gap Pad. The interface between the reference and HTHFS sensors is filled with a thermal grease to fill in asperities and minimize contact resistance. Two hardened steel plates are positioned on the top and bottom of the stack to ensure repeatable calibration results. A equal torque applied to four bolts in the steel plates draw the stack together to create constant clamping pressure through the stack. Heat transfer to the steel plates is minimized by high density insulating plates. Likewise, heat transfer via radiation and free convection from the sides of the stack is minimized by tightly packed, low thermal conductivity fibrous insulation (Not shown).

Instrumentation of the conduction calibration facility includes thermocouples as well as the lead wires carrying the voltage signals from the HTHFS and reference heat flux sensors. Type-K thermocouples are used to monitor both the heater core temperature and the water temperature which helps ensure steady state conditions are achieved prior to taking heat transfer data. The HTHFS and the reference sensor have built-in thermocouples for sensor temperature monitoring. All signals are recorded using a 24-bit National Instruments DAQ connected to a PC. All channels are sampled at $1 Hz$ since steady state heat transfer information is desired. Data is post processed in Matlab. The experimental conduction sensitivity, ϵ , for the HTHFS is calculated

using the following equation once steady state conditions are achieved:

$$S_{t-Cond} = \frac{V_t}{V_{Ref}/S_{Ref}} \quad (4.6)$$

where V_t is the output voltage for the HTHFS, V_{Ref} is the output voltage from the reference sensor, and S_{Ref} is the sensitivity of the reference heat flux sensor. The time interval used for averaging was 60 seconds.

In the current study, three series of conduction calibrations were performed consisting of four repeated trials each. For each series of four trials the HTHFS was mounted in the conduction calibration facility with new conformable layers and thermal grease and compressed to the same stack pressure. While the main goal of the conduction calibrations is to validate the analytical model predictions, they are also used to examine the effects of thermal cycling on conduction sensitivity. The first series of calibrations were performed on the HTHFS after repeated thermal cycling for extended period of time at $1050^\circ C$ in air within a high temperature kiln. The second and third series of calibrations were performed on the same sensor after repeated thermal cycling with a propane torch. In this case the sensor surface temperature approached $225^\circ C$ with the sensor measuring heat flux on the order of $10 - 13 W/cm^2$. Details of the thermal cycling regiments with kiln and torch are found in Section 4.7. Figure 4.4 shows the final conduction calibration results for the series of trials described above.

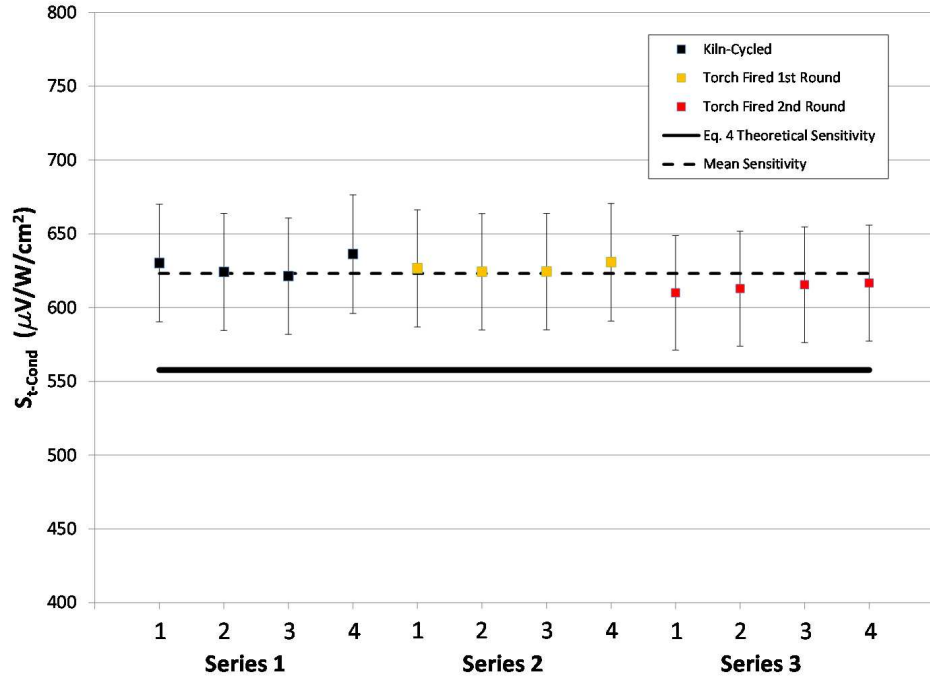


Figure 4.4: Conduction Calibration Results

As shown in Figure 4.4 the conduction calibration results compare favorably with the theoretical sensitivity calculation given the assumptions made in the thermal resistance model. The mean experimental sensitivity across all three series of calibrations is $623.2 \pm 39.5 \mu V/W/cm^2$, which is only 11.5% higher than the theoretical sensitivity. Considering the minimal scatter in the experimental sensitivity from series to series, it is apparent that repeated thermal cycling with kiln and propane torch has only a minimal impact on HTHFS conduction sensitivity.

4.6.3 Convection Calibration

The HTHFS sensor used in this study was also calibrated in turbulent stagnation point flow in anticipation that it will be used heavily in engineering applications involving convective heat transfer. Calibrations were performed in the AETHER laboratory convection calibration facility post thermal cycling. The design and performance of the convection calibration facility is detailed in a recent publication by Gifford et.al. [7]. The core of the convection calibration facility is shown schematically in Figure 4.5.

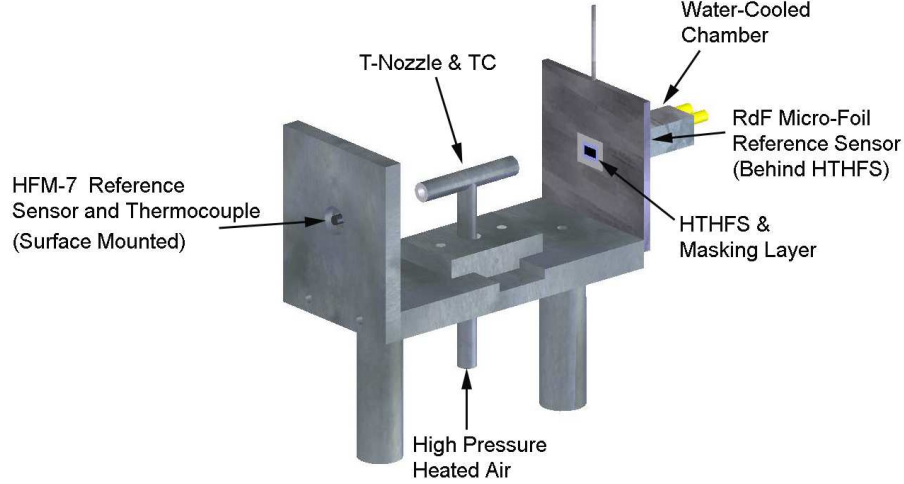


Figure 4.5: The Core of the Stagnation Flow Convection Calibration Facility

The stagnation flow convection calibration facility is composed of a main aluminum test stand, fully adjustable aluminum T-nozzle, and two sensor mounting plates. High-pressure, heated air from a custom heat exchanger (not shown) is directed through the precision machined T-nozzle where it is split evenly and directed towards both a reference heat flux sensor and a test sensor. The turbulent heat transfer coefficient on each side of the T-nozzle is identical to within approximately 3% at the stagnation point [7]. A Vatell Corp. *HFM* – 7 heat flux sensor is surface mounted in the left-hand plate at the stagnation point. A surface mounted Type-K thermocouple measures surface temperature near the HFM-7. This provides the reference heat transfer coefficient for a particular test. A Type-K thermocouple in the T-Nozzle provides total temperature measurement of the jet prior to exiting the nozzle. At steady state flow conditions, these measurements provide the heat transfer coefficient for a given air line pressure using Newton’s Law of Cooling:

$$h = (V_{Ref}/S_{Ref})/(T_j - T_{Ref}) \quad (4.7)$$

where V_{Ref} is the output voltage for the HFM-7, S_{Ref} is the sensitivity of the HFM-7 reference heat flux sensor and $(T_j - T_{Ref})$ is the temperature difference between the T-nozzle and the HFM-7 surface.

On the right-hand-side of the convection test stand the standard calibration plate is replaced by a metal mask which holds the HTHFS sensor. This is similar to the mask used in the conduction calibration facility. Immediately behind the HTHFS is the same RdF Corp. Micro-Foil reference heat flux sensor used in the conduction calibration experiments. A water-cooled chamber with a smooth aluminum surface is placed behind this reference sensor to create a constant rear surface temperature. The chamber is cooled using a high flow rate pump submerged in a water bath. The

four mounting screws on the HTHFS housing are used to draw the HTHFS, Micro-Foil sensor, and water-cooling chamber tightly together. Thermal grease is used to minimize contact resistance. Under steady state conditions the output voltage from the HTHFS coupled with the reference heat flux measurement from the RdF Micro-Foil sensor provides the experimental sensitivity for the HTHFS in convection as a function of heat transfer coefficient h . This happens to be calculated in exactly the same fashion as conduction calibration using Equation 4.6.

As in the case of conduction calibration, all signals are recorded using a 24-bit National Instruments DAQ connected to a PC. All channels are sampled at 1 Hz since steady state heat transfer information is desired. Data is post processed in Matlab. In steady state conditions approximately 60 seconds of data was averaged to obtain the convection sensitivity at a particular value of the heat transfer coefficient. The

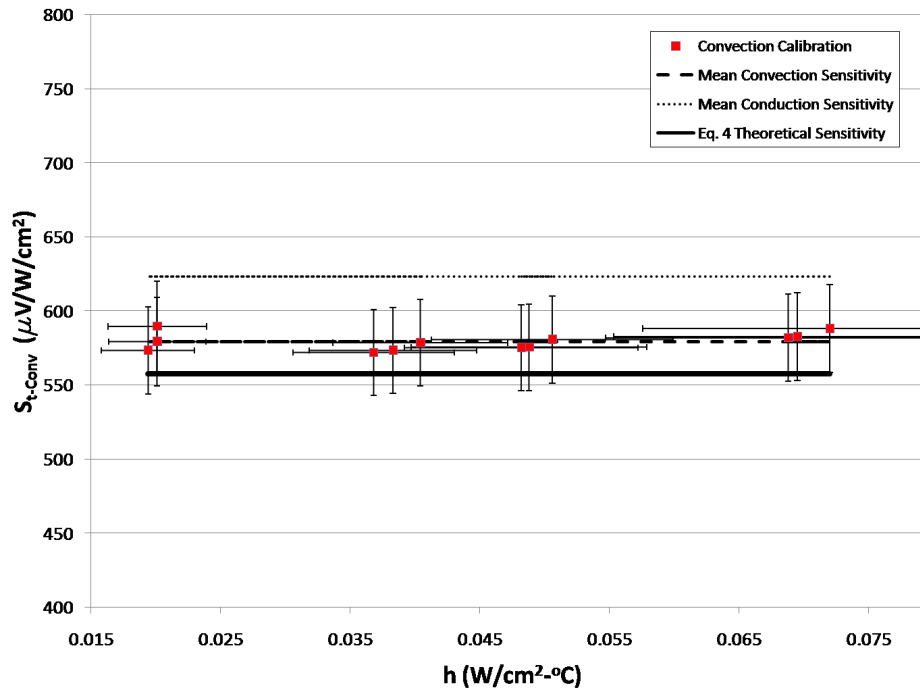


Figure 4.6: Convection Calibration Results

results of the convection calibration are shown in Figure 4.6. A total of four cases, consisting of four trials each at a particular line pressure setting, were performed for the convection calibration. Despite increasing uncertainty in the heat transfer coefficient over the range of $h = 0.02 - 0.07 W/cm^2 - ^\circ C$, the HTHFS sensitivity is essentially constant. Hence, sensitivity does not appear to depend on the heat transfer coefficient. The mean HTHFS sensitivity over the range of heat transfer coefficients is $S_{t-Conv} = 579.3 \pm 29.4 \mu V/W/cm^2$. The mean sensitivity is only around 4% higher than the theoretical sensitivity predicted via Equation 4.5 for conduction and only 7.5% lower than the mean experimental conduction calibration sensitivity.

4.6.4 Calibration Uncertainty Analysis

The following uncertainty analysis was performed on the calculation of the experimental sensitivity of the HTHFS in conduction and convection. The analysis follows that of Coleman and Steele⁸. The total uncertainty in the HTHFS sensitivity, S_t , for

a particular measurement is found using Equation 4.8:

$$\left(\frac{U_{S_t}}{S_t}\right)^2 = \sum_{i=1}^J \left(\frac{1}{S_t} \frac{\partial S_t}{\partial X_i} U_{X_i}\right)^2 \quad (4.8)$$

where U_{S_t} is the total experimental uncertainty, which is a function of independent experimental variables X_i . The total uncertainty in each independent variable is given by, U_{X_i} , while $\frac{\partial S_t}{\partial X_i}$ are the associated sensitivity coefficients. Using the formula for the time-averaged experimental gage sensitivity presented in Equation 4.6 for conduction, the expanded form of Equation 4.8 becomes:

$$U_{S_t-Cond} = S_t \sqrt{\left(\frac{1}{V_t}\right)^2 U_{V_t}^2 + \left(\frac{-1}{V_{Ref}}\right)^2 U_{V_{Ref}}^2 + \left(\frac{1}{S_{Ref}}\right)^2 U_{S_{Ref}}^2 + U_{rep}} \quad (4.9)$$

where U_{rep} is the estimated repeatability error in the conduction calibration facility. Equation 4.9, with the exception of the repeatability uncertainty, is identical in form to that used for the convection calibration data. However, there is also an uncertainty associated with the measured heat transfer coefficient in the convection calibration experiments. Application of Equation 4.8 to Equation 4.7 gives the following uncertainty in heat transfer coefficient:

$$U_h = h \sqrt{\left(\frac{-1}{T_j - T_{Ref}}\right)^2 U_{T_j}^2 + \left(\frac{1}{T_j - T_{Ref}}\right)^2 U_{T_{Ref}}^2 + \left(\frac{1}{V_{Ref}}\right)^2 U_{V_{Ref}}^2 + \left(\frac{1}{S_{Ref}}\right)^2 U_{S_{Ref}}^2 + U_{h-SS}} \quad (4.10)$$

In this case uncertainty in the convection calibration stand h-value from side-to-side is $U_{h-SS} = 0.03h$.

Uncertainties in each independent variable are estimated, or calculated using each variable's precision and bias error limits according to Equation 4.11:

$$U_{X_i} = \sqrt{B_{e-X_i}^2 + P_{e-X_i}^2} \quad (4.11)$$

Bias limits for the thermocouples used in the convection calibrations are a combination of thermocouple and data acquisition bias errors, and in this case depend on the mean values used to calculate the average sensitivity at a particular value of the heat transfer coefficient. A bias limit of $0.1^\circ C$ is quoted with the DAQ, while a bias error of 0.75% of full scale is quoted for each thermocouple reading. Hence, Equation 4.12 is used to calculate the total bias limit:

$$B_{e-T_j,Ref} = \sqrt{(0.1)^2 + (0.0075 T_{j,Ref})^2} \quad (4.12)$$

Where applicable the precision limits were calculated from 128 continuous samples of nominal room temperature data using a student's t-distribution with 127 degrees of freedom and a 95% confidence interval. Table 5.1 reports the overall average bias, precision, and total uncertainty in each measured quantity for the calibrations performed on the HTHFS in conduction and convection. All quantities are averaged over the number of experiments performed. Note that the reference sensor designations are written explicitly in Table 5.1 to avoid confusion.

The experimental conduction and convection sensitivities averaged over each series of trials are summarized in Table 5.2. The total uncertainty as a percentage of the overall sensor sensitivity is included. The percentage uncertainty is around 6% for the conduction calibrations and 5% for the convection calibrations. As apparent in Tables 5.2 the largest component of the total uncertainty for either calibration approach is associated with the bias error of the reference sensor sensitivity.

Conduction Calibration				
Xi	Bias Limit	Precision Limit	Total	Units
V_{RdF}	3.92	1.67	4.26	μV
V_{HTHFS}	3.92	1.14	4.08	μV
S_{RdF}	46.25	-	46.25	$\mu V/W/cm^2$
Convection Calibration				
Xi	Bias Limit	Precision Limit	Total	Units
T_j	0.76	0.72	1.05	$^{\circ}C$
T_{HFM}	0.33	0.16	0.37	$^{\circ}C$
V_{HFM}	3.92	2.48	4.63	μV
V_{RdF}	3.92	3.40	5.19	μV
V_{HTHFS}	3.92	2.49	4.64	μV
S_{HFM}	10.25	-	10.25	$\mu V/W/cm^2$
S_{RdF}	46.25	-	46.25	$\mu V/W/cm^2$

Table 4.2: Average Bias, Precision, and Total Uncertainties in Measured and Calculated Variables

Series #	Conduction			Convection		
	$S_t \left(\frac{\mu V}{W/cm^2} \right)$	$S_t \left(\frac{\mu V}{W/cm^2} \right)$	U_{S_t}	$S_t \left(\frac{\mu V}{W/cm^2} \right)$	$S_t \left(\frac{\mu V}{W/cm^2} \right)$	U_{S_t}
1	627.93	39.82	6.34	574.70	28.93	5.03
2	626.48	39.63	6.32	580.88	29.87	5.14
3	613.70	39.05	6.36	577.23	29.15	5.05
4	n/a	n/a	n/a	584.30	29.56	5.05

Table 4.3: Average Total Uncertainties in Sensitivity for Conduction and Convection

4.7 Thermal Cycling: Kiln and Torch Tests

As mentioned previously in Section IV the HTHFS sensor was subjected to repeated thermal cycling to determine the effects on sensor sensitivity and to show conclusively that the HTHFS design can withstand both extreme temperature and heat flux for an extended period of time. In the first series of tests the HTHFS was cycled on five successive occasions in air between $100^{\circ}C$ and $1050^{\circ}C$ inside a temperature feedback controlled kiln. The temperature ramp-up rate ranged from $0.5^{\circ}C/sec$ to $1.1^{\circ}C/sec$. The sensor was allowed to soak at the maximum temperature for 20 minutes before being pulled out of the kiln for rapid cooling back to a nominal $100^{\circ}C$. The HTHFS performed excellent in these tests and, as shown previously, the sensitivity was unaffected. Figure 4.7 shows the HTHFS immersed in the kiln. No failure in the sensor construction occurred and little to no oxidation was observed on the sensor surface.

A series of propane torch tests reinforced the positive results from the kiln thermal cycling studies. To maximize the applied temperature gradient and hence the heat flux and thermal stress on the sensor, a water cooled plate was constructed as shown in Figure 4.7(a). The HTHFS was pressed against the surface of the water-cooled plate by a stand-off metal shield. Torch applications lasted 10 minutes and were repeated 15 times without sensor failure. Figure 4.7(b) shows a photograph of the

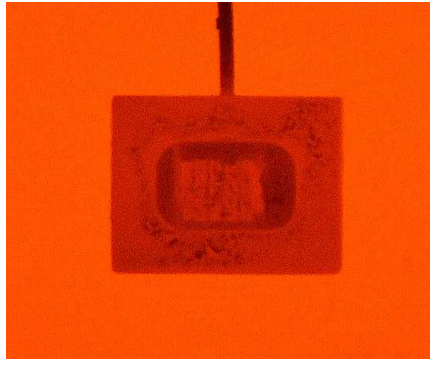


Figure 4.7: Thermal cycling HTHFS at 1050°C

HTHFS being subjected to the propane torch. A typical plot of surface temperature and the corresponding heat flux measured by the HTHFS are shown in Figure 4.9. Maximum heat flux levels were in the vicinity of $10 - 13\text{W}/\text{cm}^2$ over the course of testing.

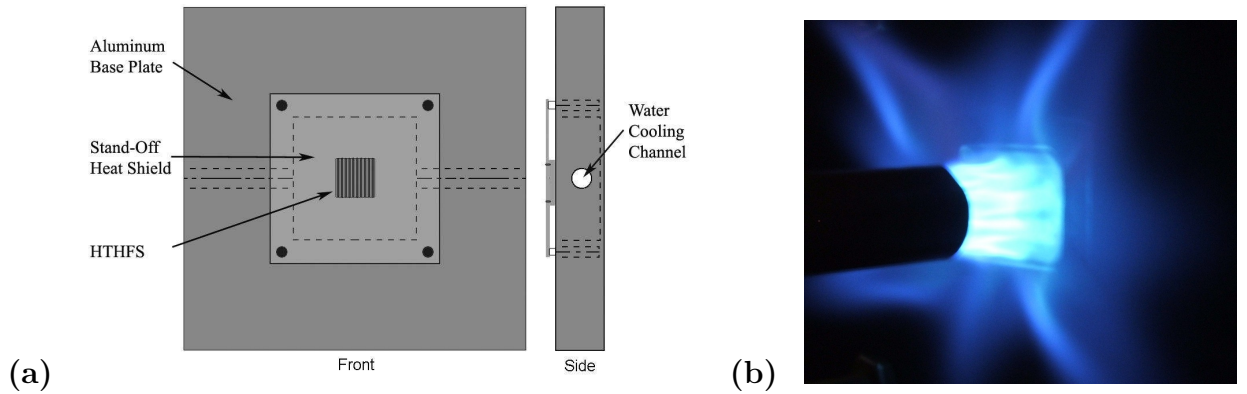


Figure 4.8: Propane Torch Test Apparatus and Torch Testing

4.8 Conclusions

The HTHFS has been successfully prototyped using high temperature thermoelectric elements and insulators in a durable thermopile design. Calibration of a representative sensor was performed in both conduction and convection heat transfer. Experimental sensitivities are very close to the value predicted using simple analysis and a 1-D thermal resistance modeling of the sensor. The HTHFS sensor was subjected to numerous thermal cycling tests involving kiln firing and propane torch applications. The sensors robust construction withstood these tests. Calibrations of this sensor after thermal cycling reveal no appreciable shift in sensitivity. The next phase of research will focus on miniaturization of the HTHFS concept for faster time response. Experiments are also planned to examine the effects of highly oxidizing atmospheres on the HTHFS materials.

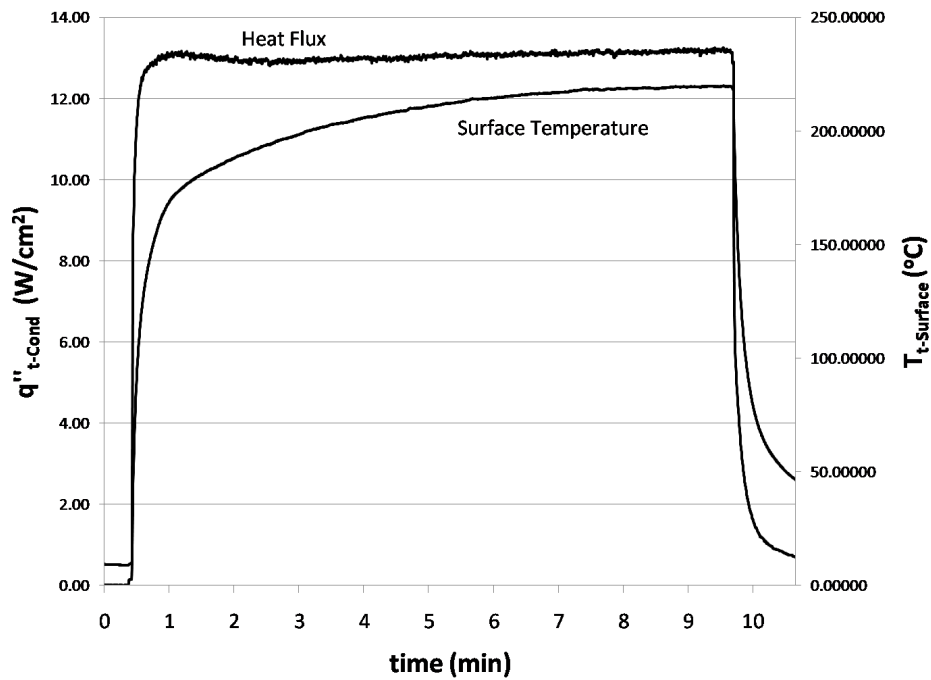


Figure 4.9: Example of Torch Testing Data

4.9 Acknowledgements

This work was sponsored by Sandia National Laboratories under Grant No. XXXXX. We wish to thank program managers Jim Nakos and Tom Blanchet for their patience and support on this project. We would also like to thank James Sracic for assistance with this project.

4.10 References

1. Diller, T.E., Heat Flux. The Measurement, Instrumentation and Sensors Handbook, 34, edited by J. G. Webster, CRC Press, Boca Raton, 1999, pp. 34.1-34.15.
2. Raphael-Mabel, S., Huxtable, S., Gifford, A., and T.E. Diller. "Design and Calibration of a Novel High Temperature Heat Flux Gage," ASME HT-2005-72761, July 17-22, 2005.
3. ASM Ready Reference: Thermal Properties of Metals, Material Data Series, edited by F. Cverna., ASM International, Materials Park, Ohio, 2002.
4. Blatt, Schroeder, Foiles, and Greig. Thermoelectric Power of Metals, Plenum Press, New York, NY, 1976.
5. Manual on the Use of Thermocouples in Temperature Measurement, ASTM, Philadelphia, Pa.,1970.
6. Hager, N., "Thin Foil Heat Meter," The Review of Scientific Instruments, Vol 36., No. 11, Nov 1965, pp.1564-1570.
7. Gifford, A., et.al. "Convection Calibration of Schmidt-Boelter Heat Flux Gages in Shear and Stagnation Air Flow," TBD Need reference specifics

8. Coleman, H.W. and Steele, W. G. Experimentation and Uncertainty Analysis for Engineers, John Wiley & Sons, New York, NY, 1989.

Chapter 5

Convection Calibration of Schmidt-Boelter Heat Flux Sensors in Shear and Stagnation Flow

This chapter is comprised of sections from ASME Journal of Heat Transfer Paper No. *HT* – 08 – 1529 submitted on November 30, 2008. Acceptance of this paper for publication is still pending.

5.1 Abstract

Experiments were performed to characterize the performance of Schmidt-Boelter heat flux gages in stagnation and shear convective air flows. The gages were of a standard design (25.4mm and 38mm diameter) using a copper heat sink with water cooling channels around the active sensing element. A simple model of the gages using an internal thermal resistance between the sensor surface and the heat sink is used to interpret the results. The model predicts a non-linear dependence of the gage sensitivity as a function of heat transfer coefficient.

Experimental calibration systems were developed to simultaneously measure the heat flux gage response relative to a secondary standard under the same flow and thermal conditions. The measured gage sensitivities in stagnation flow matched the model and were used to estimate the value of the internal thermal resistance for each of the four gages tested. For shear flow the effect of the varying gage surface temperature on the boundary layer was included. The results matched the model with a constant factor of 15 to 25 percent lower effective heat transfer coefficient. When the gage was water cooled, the effect of internal thermal resistance of the gage was markedly different for the two flow conditions. In stagnation flow the internal resistance further decreased the apparent gage sensitivity. Conversely, in shear flow it was effectively offset by the cooler heat sink of the gage and the resulting sensitivities were nearly the same as, or larger than, for radiation.

5.2 Nomenclature

E_g	Gage voltage output (mV)
h	Heat transfer coefficient ($Wm^2 - K$)
L	Nozzle width (mm)
q	Heat transfer (W)
q''	Heat flux (W/m^2)

R''	Thermal resistance ($m^2 - K/W$)
S	Gage sensitivity ($mV/(W/m^2)$)
T	Temperature ($^{\circ}C$)
ϵ	Surface emissivity
σ	Stefan-Boltzmann constant ($5.67 \times 10^{-8} W/m^2 - K^4$)
Subscripts	
abs	absorbed
$cond$	conduction
$conv$	convection
g	gage
inc	incident
p	plate
r	radiation source
rad	radiation
s	sink
w	water
∞	air

5.3 Introduction

As energy becomes increasingly costly, the importance of efficiency in energy systems becomes more important. One tool for analyzing and controlling energy intensive processes is the measurement of heat flux. The use of heat flux gages along with temperature measurements gives a more complete understanding of energy systems because of the additional information about energy transfer and heat paths that is provided.

Although a number of heat flux gages are commercially available, they are usually only calibrated in radiation. Consequently, if they are used for convective heat flux measurements there are questions about their accuracy. Because the gage can cause a disruption of the thermal conditions at the surface where it is mounted [1], it is important to calibrate heat flux gages in environments close to their use. The present research investigates the operation of heat flux gages in convection and the difference between radiation and convection calibration. A unique convection calibration facility was developed to calibrate four Schmidt-Boelter heat flux sensors and compare the results with the usual radiation calibrations. The implications for the measurement of convective heat flux are discussed.

5.4 Heat Flux Measurement

Most methods for measuring heat flux are based on either application of a sensor onto a surface or insertion through a hole in the material to a position flush with the surface. Either method can cause physical and/or thermal disruption of the surface. The measurement goal is to minimize these disruptions to measure the actual heat flux at the surface. This requires an understanding and analysis of the gage system.

The present work considers an insert heat flux gage as shown in Figure 1. In general, three modes of energy transfer act on the gage. Fig. 1 Heat flux sensor with the three modes of energy transfer Assuming that the material is opaque, an energy balance at the surface relates the different modes of heat transfer as

$$q_{cond} = q_{conv} + q_{rad} \quad (5.1)$$

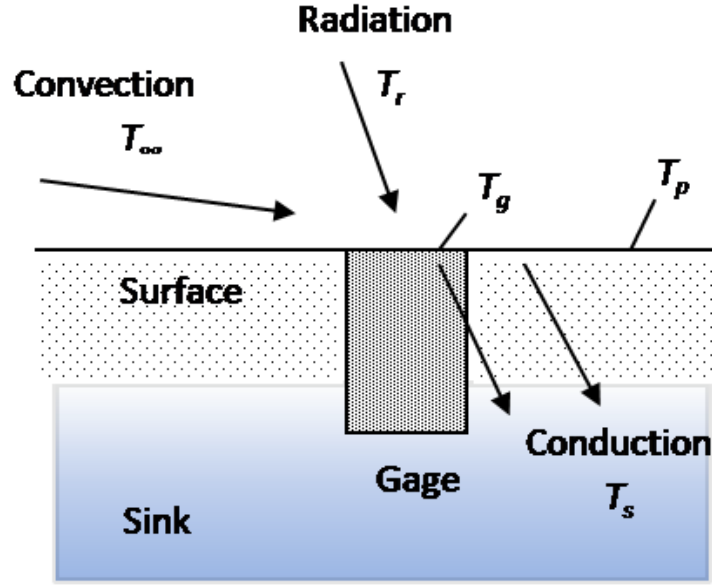


Figure 5.1: Simplified 1-D thermal resistance model of HTHFS

Conduction through the gage and the plate provides the pathway for the energy transfer by convection and radiation at the surface. The convection heat transfer can be expressed in terms of the difference in temperature between the fluid and the surface of the gage as

$$q''_{q_{conv}} = h_g (t_\infty - T_g) \quad (5.2)$$

Because the gage surface temperature may be different than the plate temperature, the convection to the gage may be different than that to the plate as expressed by

$$q''_{p_{conv}} = h_p (t_\infty - T_p) \quad (5.3)$$

The difference in surface temperature may also affect the heat transfer coefficient, as indicated by the different subscripts in equations 5.2 and 5.3. For radiation, if the radiator surrounds the gage and appears black, the flux to the gage is simply

$$q''_{rad} = \epsilon \sigma (T_r^4 - T_g^4) \quad (5.4)$$

where ϵ is the gray body emissivity of the gage and the temperatures are absolute. If the temperature of the radiator (T_r) is much higher than the temperature of the gage (T_g), the last term in equation 5.4 is negligible.

5.5 General Thermal Model of the Heat Flux Gage

As shown in Fig. 1, the heat flux gage measures the net convection and radiation at its surface. At steady state the thermal energy is necessarily transferred through the gage to a heat sink, which is usually the mounting plate or water cooling channels. An overall thermal resistance, R'' , from the surface of the gage to the heat sink can, therefore, be defined as

$$R'' = \frac{T_g - T_s}{q''_g} \quad (5.5)$$

where T_g is the average surface temperature of the gage, T_s represents the temperature of the heat sink, and q_g'' is the conduction through the gage. All of the thermal resistances between the gage surface and the heat sink are included. Examples of the thermal resistances are: solid material, contact resistances, air gaps, paint, thermal paste, potting material, and glue layers.

At the surface of the gage the net convection and radiation must equal the conduction through the gage, as expressed by equation 5.1. For the combined convection and radiation heat transfer case, the heat flux to the gage is matched with the conduction expressed in equation 5.4.

$$q_g'' = h_g (T_\infty - T_g) + \epsilon\sigma (T_r^4 - T_g^4) = \frac{T_g - T_s}{R''} \quad (5.6)$$

The heat flux to the plate due to combined convection and radiation heat transfer has the same form,

$$q_p'' = h_p (T_\infty - T_p) + \epsilon\sigma (T_r^4 - T_p^4) \quad (5.7)$$

but there is assumed to be no conduction resistance between the plate and the heat sink ($T_p = T_s$). In a purely convective environment without radiation, the ratio of equations 5.6 and 5.7 reduces to

$$\frac{q_g''}{q_p''} = \frac{h_g (T_\infty - T_g)}{h_p (T_\infty - T_s)} \quad (5.8)$$

The gage surface temperature, T_g , which is generally unknown, may be found using equation 5.6 as

$$T_g = \frac{\frac{T_s}{R''} + T_\infty h_g}{\frac{1}{R''} + h_g} \quad (5.9)$$

This gage surface temperature also appears as the center temperature of a resistance network as shown in Fig. 5.2. Using Fig. 5.2, the heat flux through the gage can be expressed in terms of the sink temperature using only the conduction resistance R'' and the convection resistance $1/h_g$ as

$$q_g'' = \frac{(T_\infty - T_s)}{\frac{1}{h_g} + R''} \quad (5.10)$$

Substitution of equation 5.10 into equation 5.8 gives a ratio of heat fluxes

$$\frac{q_g''}{q_p''} = \frac{1}{\frac{h_p}{h_g} + h_p R''} \quad (5.11)$$

The ratio of the heat flux to the gage and to the plate is then only a function of the two dimensionless parameters, h_p/h_g and $h_p R''$. These relate the flow parameters and the gage parameters to a systematic error in the resulting measurement. Kuo and Kulkarni [2] used a similar model for the internal resistance of a Gardon gage without the h_p/h_g term.

5.6 Heat Flux Gages

Two styles of heat flux gages already available on the market are the Heat Flux Microsensor (HFM) and the Schmidt Boelter (SB). The HFM is a thin-film thermopile

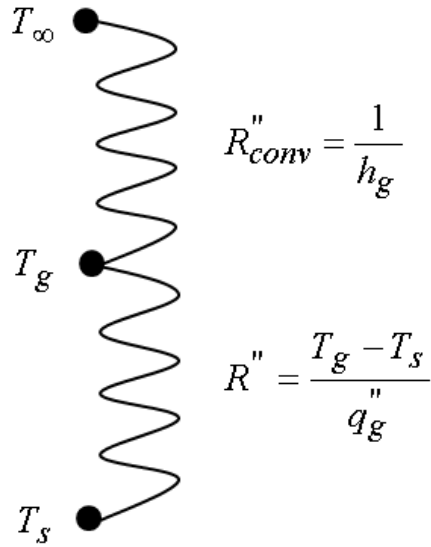


Figure 5.2: Heat flux gage resistance network for convection

that is less than 2 m thick [1]. It is deposited on a ceramic base of aluminium nitride ($k = 175W/m - K$) which is press fit into a 6.3mm diameter metal housing. The use of high temperature thermocouple materials allow operating temperatures over 800C for short times and heat flux from 1 kW/m, with no practical upper limit. Because of the thin sensor design, the thermal response time is less than $10\mu s$ so that the frequency response is well above $10kHz$ [3]. The high temperature and fast time response capabilities are useful for aerodynamic applications, including combustng flows and high speed events such as shock-waves. Because of the very thin design on a high conductivity base, it has a minimal thermal resistance, which is assumed to be negligible. Consequently, the HFM is used as the standard for the convection calibrations and is assumed to be at the same temperature and heat flux as the plate.

The Schmidt-Boelter Gage is the major emphasis of this work. The active element of a Schmidt-Boelter gage is a bare constantan wire, usually about 0.05mm in diameter, which is wrapped around the thermal resistance layer, or wafer [1]. Consequently, the sensor is sometimes called a wire-wound gage. The wafer is usually made of anodized aluminium with the geometry illustrated in Fig. 5.3. The wire/wafer assembly is electroplated with copper on one side. After plating, the wafer with the wire is placed into the gage body, which works as a heat sink for the sensor. The entire wafer is then surrounded by a potting material to give a smooth surface to the top of the gage.

The basic heat flux sensing mechanism uses the temperature gradient developed between the top and the bottom surface of the wafer. The sensitivity is directly proportional to the number of turns of constantan wire wound around the wafer, although the output is less than that for an actual thermopile with separate thermocouple wire and junctions [4]. The thermoelectric signal is produced with what appears to be a constantan wire in electrical series with a parallel combination of constantan and copper. Four different Schmidt-Boelter gages have been examined. They were manufactured by Medtherm Corp. and included two one-inch (25mm) in diameter and two one-and-one-half-inches (38mm) in diameter. They were supplied by Sandia National Laboratories.

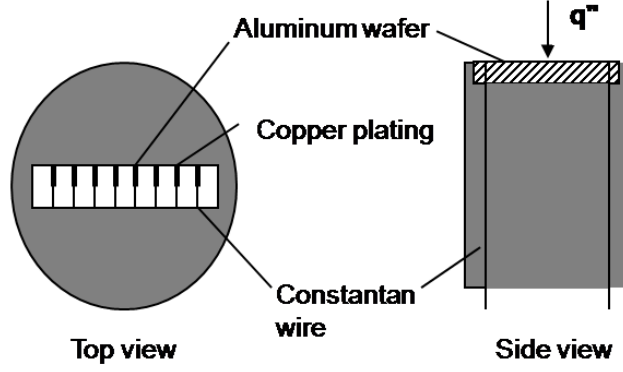


Figure 5.3: Schematic diagram sketch of the Schmidt-Boelter gage

5.7 Radiation Calibration

Heat flux gages are almost always calibrated based on an incident radiation source. The narrow-angle method focuses a beam of radiation from a black-body cavity onto the gage surface, which sits outside of the cavity. The insert method actually puts the gage into a graphite-tube cylindrical cavity. Murthy et al. [5] describe these two radiation calibration methods as used at the National Institute of Standards and Technology (NIST). For the incavity calibrations an optical pyrometer is used to measure the center partition temperature of the graphite tube and control the power supply to maintain the cavity temperature at the set point. The NIST narrow-angle method uses an electrical substitution radiometer (ESR) as the standard. The heat flux gage to be calibrated and the transfer standard radiometer are alternately substituted at the same position to receive equal radiant heat flux from the blackbody cavity. The heat flux gage manufacturers use variations of these methods to calibrate the gages that are used commercially. They usually provide calibrations based on the incident radiation, but may also include the effect of the gage absorptivity (assumed equal to the emmissivity) for an absorbed sensitivity

$$S_{abs} = \frac{S_{inc}}{\epsilon} = \frac{E_g}{q_g''} \quad (5.12)$$

where E_g is the voltage output of the gage and q_g'' is the net heat flux to the gage as shown previously in equation 5.10. The absorbed sensitivity will be used throughout this paper.

The cavity temperatures for radiation calibration usually range from $1100^\circ C$ to $2500^\circ C$ [5]. This corresponds to radiation heat fluxes up to $3,300 kW/m^2$. Because the gage is maintained at close to room temperature ($300K$) during calibration, the contribution of the T_g^4 term in equation 5.4 is negligible ($< 0.2\%$). In addition, convection effects are designed to be negligible. Consequently, there is no effect of the gage temperature on the heat flux during radiation calibration. Therefore, the gage heat flux is the same as the plate heat flux, $q_g'' = q_p''$, for radiation calibration and

$$S_{abs} = \frac{E_g}{q_p''} \quad (5.13)$$

5.8 Convection Calibration

Because the internal conduction pathway for measuring heat flux within most heat flux gages is the same for convection or radiation, the convection sensitivity for the heat flux that passes through the gage is the same as that for the absorbed radiation, $S_g = S_{abs}$. Unlike for the radiation calibration, however, the convection heat transfer is dependent on the surface temperature of the gage. Consequently, any temperature difference relative to the plate will cause a difference in the measured heat transfer and the influence of equation 5.11 must be considered when interpreting convection results. Using the same form as equation 5.13 gives the convection sensitivity in terms of the plate heat flux as

$$S_{conv} = \frac{E_g}{q_p''} = \frac{S_{abs}}{\frac{h_p}{h_g} + h_p R''} \quad (5.14)$$

This equation represents the two major effects on the apparent sensitivity of heat flux gages in convection, i.e. changes in the heat transfer coefficient and internal thermal resistance. It is the major theoretical assumption of this research and will be used to help interpret the experimental results.

5.9 Convection Calibration Facility

A convection calibration facility has been developed to calibrate heat flux gages for heat transfer in both shear and stagnation flow. In shear flow there is an upstream thermal boundary layer influence on the heat transfer coefficient at the gage, which means that $h_g \neq h_p$. Conversely, for stagnation flow there is no upstream boundary layer, so that $h_g = h_p$ for this case. The basic apparatus is the same for both shear and stagnation flow, as illustrated in Fig. 5.4.

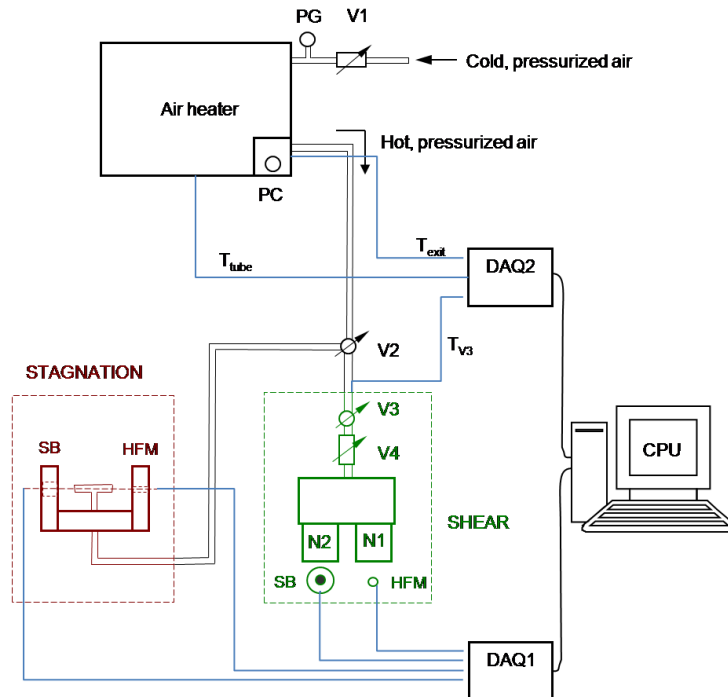


Figure 5.4: Schematic of the Convection Calibration Facility

A compressed air supply with a maximum pressure of about $400kPa$ is connected to the facility with a pressure gage (PG) to set the supply pressure. The air flows directly into an air heater consisting of a copper tube with a high temperature heater tape wrapped around the tube and a power controller to adjust the exit air temperature. A series of valves (V1 to V4) directs the air flow to the stagnation stand or through the nozzles (N1 and N2) of the shear stand. The electrical power of about $2kW$ is sufficient to heat the air to over $150^{\circ}C$. An aluminum box was constructed around the copper tubing and packed with glass-fiber insulation. An *NITBX – 68T* 24-bit data acquisition unit (DAQ1) was used to measure the two heat fluxes and the temperatures. A second data acquisition unit (DAQ2) was used to record the heater temperature and pressure. The data sampling was carried out with LabVIEW®.

5.9.1 Stagnation Stand

The stagnation stand was designed to provide the same convective heat flux to the reference standard and to the test gage. This was realized by simply putting a tee junction in the air supply line with a $6.3mm$ orifice at each end, creating equal impinging jets on each surface. Figure 5.5 shows the basic design of the stagnation stand. The gages were mounted in vertically aligned plates which were connected to the main support plate, forming a U-shape and holding the tee nozzle in position. The distance between orifices and plates was set at $50mm$, to provide maximum and consistent convection heat flux. The inlet heated air from the air heater was directed into the tee nozzle from the bottom side of the stand.

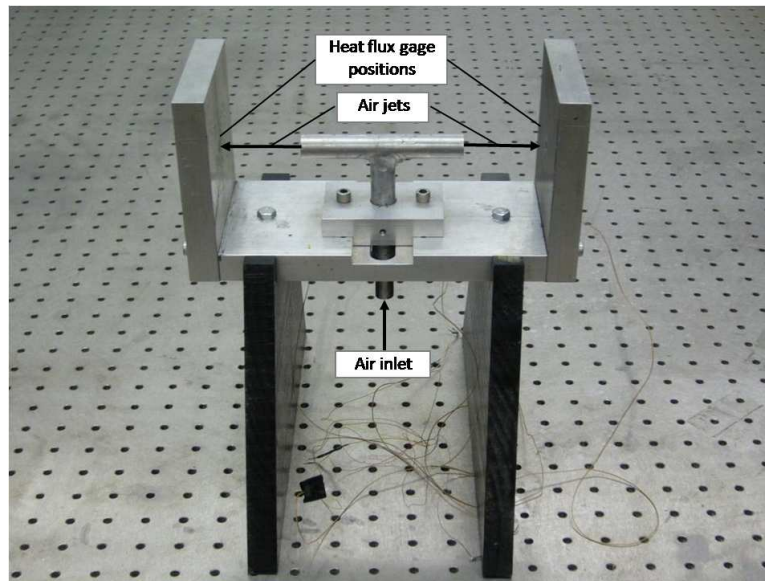


Figure 5.5: Stagnation Calibration Stand

A type K thermocouple was mounted in the air supply of the nozzles, immediately before the tee junction to measure the incoming air temperature. Thermocouples were also press fit into the aluminium plates flush with the surface. They were located right next to the heat flux gages to measure the plate temperature at the gage location. The gages were mounted into the plate and aligned with the center line of the nozzle. The $25 - mm$ diameter Schmidt-Boelter gages have a large flange that was connected to the back of the plate with three screws. A washer between the flange and the plate aligns the gage surface flush with the plate surface. The $38 - mm$ diameter Schmidt-Boelter gages did not have a flange and were held into the plate by using one plastic set screw. To close the air gaps between gages and plate and to better align gage and

plate surface, a high thermal conductivity paste was used ("*OmegaTherm201*©"). The HFM was mounted into the plate with a special screw assembly to provide good thermal contact with the plate as illustrated in Fig.5.6.

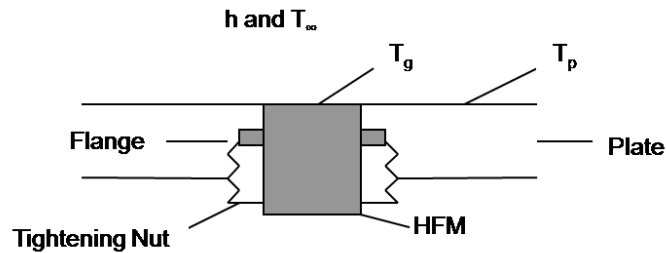


Figure 5.6: HFM mounting in a plate

The calibration test started with the sensors blocked by a cover to divert the air jets until a steady-state condition was reached (constant air temperature through the tee nozzle). At this point the data acquisition was started and a few seconds of data was taken to establish the reference zero for each gage in each test run before the cover was removed allowing the jets to impinge on the sensors. The measurements with flow were taken for 20 seconds. After the test was done, the stand was allowed to cool down to room temperature again, which took approximately 20 minutes. Several tests were performed to confirm that the heat flux from each of the impinging jets was the same. These consisted of a series of measurements that switched the sensors from one side to the other. The results showed no difference due to location on the calibration values of the gages within the three percent uncertainty of the measurements.

5.9.2 Shear Stand

The shear stand provided turbulent convective air flow parallel to a plate surface. Heated air was directed to a plenum and then through two identical flat nozzles over the plate. The exit dimensions of the nozzles are $L = 12mm \times H = 2.4mm$, as illustrated in Fig. 5.7.

The plenum and nozzles were mounted to the plate as pictured in Fig. 5.8, creating a wall jet along the plate. The heat flux gages were mounted in the plate by the same procedure as for the stagnation stand. The centers of the gage sensing areas were placed about $20mm$ from the exit of the nozzles, side-by-side along the nozzle centerlines. In Fig. 5.8 the nozzles are labeled "1" and "2", with the HFM mounted with nozzle *N2* and a $38mm$ diameter Schmidt-Boelter gage mounted with nozzle *N1*. The flow characteristics from the nozzles were measured with Particle-Image Velocimetry (PIV) and were shown to be typical of a well developed wall jet at the gage locations [6].

The plenum assembly was designed to provide the same air flow through both nozzles. To improve the uniformity, a flow resistance made of copper foam was mounted inside of the plenum and attached to the nozzle inlets. Total pressure measurements were done to quantify the flow at the nozzle exits. The results are shown in Fig. 5.9 in terms of the corresponding velocities at a few positions at the exit of each nozzle. Notice that the flow velocity is nearly identical at the center of each nozzle. The effect on the heat flux measurements is discussed later.

All of the thermocouples used were type K. There were two thermocouples placed inside of the box to measure the air temperature in the middle of each nozzle entrance. There were two thermocouples press fit into the plate. They were located along

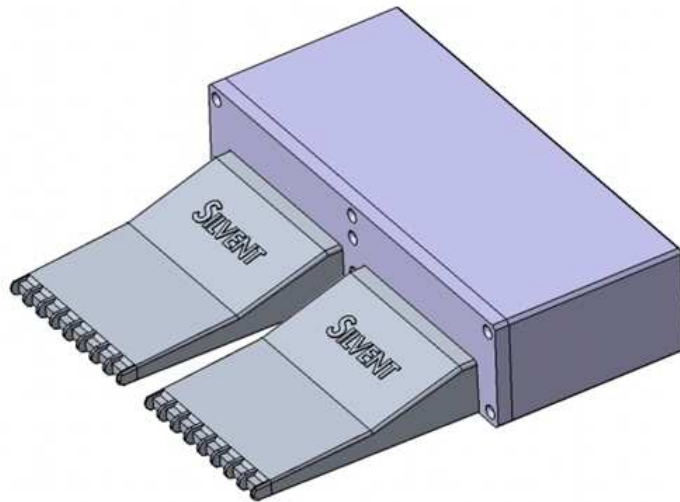


Figure 5.7: Shear Stand Nozzles

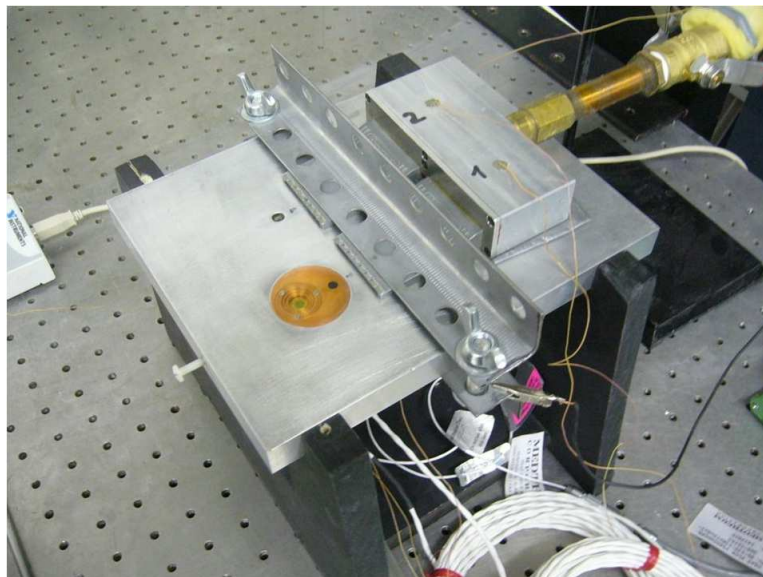


Figure 5.8: Picture of the assembled shear stand

the centerline of the nozzles, upstream of the corresponding heat flux gage, and at the same distance from the nozzle. If water cooling was used, there was also a thermocouple for measuring the water temperature.

The sampling frequency for all of the temperatures and heat fluxes was set to $1Hz$. Data sampling began 10 seconds before the flow was initiated to establish the reference zero values for the heat flux gages. Data were taken until the air temperature in the plenum reached steady-state conditions. This took approximately ten minutes (for lower pressures) to seven minutes (for higher pressures). Once steady-state temperature was achieved, data were taken for another 30 seconds. After a test was completed, the entire assembly was cooled down to room temperature in order to start from the same initial conditions.



Figure 5.9: Exit nozzle velocities from total pressure measurements

5.10 Data Analysis

The heat transfer coefficient was determined from the HFM standard measurements of heat flux and temperature, which were assumed to match those of the plate, as previously discussed.

$$h_p = \left[\frac{q_p''}{(T_\infty - T_p)} \right]_{HFM} \quad (5.15)$$

Radiation effects were neglected because the plate and gages were near room temperature and the same small effect acts on both gages. The corresponding heat flux that should be measured by the Schmidt-Boelter gage being calibrated is then

$$q_{SB}'' = h_p (T_\infty - T_s)_{SB} \quad (5.16)$$

with the calculated sensitivity of the Schmidt-Boelter gage

$$S_{conv} = \frac{E_g}{q_{SB}''} = \frac{E_g}{h_p (T_\infty - T_s)_{SB}} \quad (5.17)$$

The value of the sink temperature, T_s , for the Schmidt-Boelter gage was taken from the mounting plate or from the cooling water temperature at the location of the gage. The resulting convection sensitivity gives the gage output relative to the heat flux to the surrounding plate and includes the effect of the altered gage surface temperature on the heat flux experienced by the gage.

A typical set of test data for the shear stand is shown in Fig. 5.10. The air temperatures are shown at each side of the plenum box before the air enters the nozzles. The values on each side are nearly identical over the entire length of the test. The plate temperatures start from about 28°C room temperature and rise until they reach 70°C at the end of the test on both sides with negligible differences. The heat flux signal shows a maximum at around 100 seconds and then decreases as the air to plate temperature difference decreases over the duration of the test of about 730 seconds. The sensitivity was averaged in the range of 500 seconds to 600 seconds for the shear stand. Figure 5.11 shows the resulting heat transfer coefficient, which remains essentially constant over this time span, as expected. The stagnation tests are similar, except the temperature changes are smaller because of the shorter run time (about 30s) of these tests.

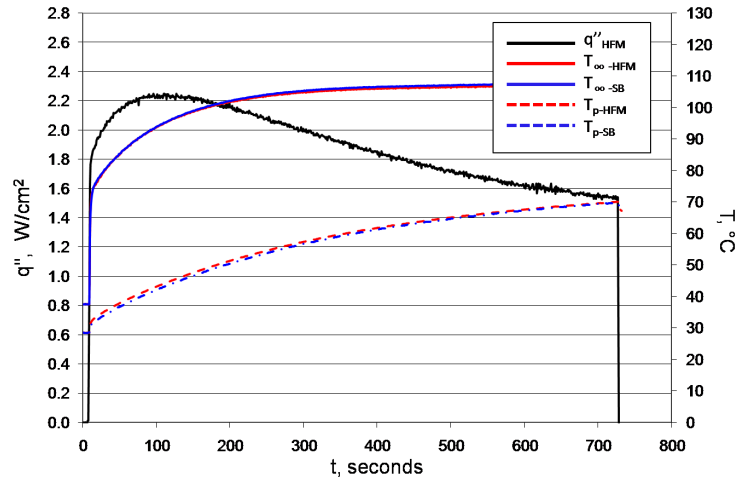


Figure 5.10: Typical heat flux and temperature data for the shear stand

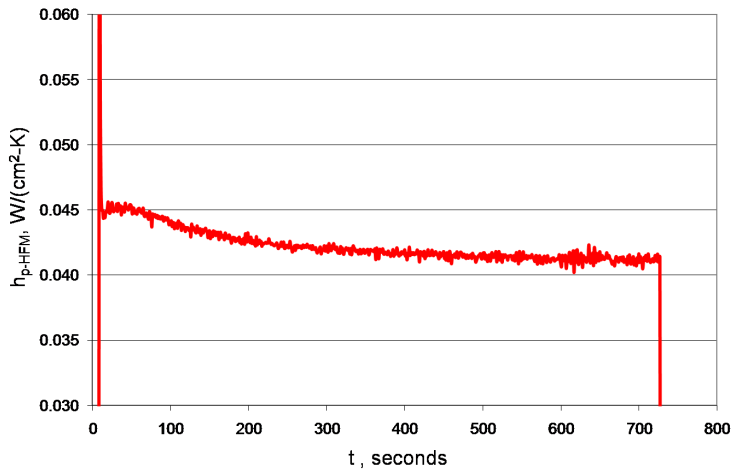


Figure 5.11: Typical progression of the heat transfer coefficient for the shear stand

Because the heat flux results could be up to twenty percent different from the two nozzles on the shear stand, the Schmidt-Boelter gage and HFM were switched and tested under both nozzles. The resulting sensitivity was averaged between the tests on both sides of the shear stand. This was not necessary for the stagnation tests because the heat flux matched within experimental uncertainty from side-to-side.

5.11 Calibration Results

The measured sensitivities were plotted for each gage over a range of air pressures, giving different heat transfer coefficients. An example of the results is shown in Fig. 12 for one of the four Schmidt-Boelter gages in the stagnation flow calibration stand. The average experimental uncertainty was estimated to be 6.6% for the measured sensitivities. This was obtained from the combined standard error of all of the associated bias and precision uncertainties [7]. The largest contribution was the radiation

calibration uncertainty between the two gages, which was estimated to be 5%. The assumption for stagnation flow is that the heat transfer coefficient is the same for the two gages and the plate, $h_g = h_p$, because there is no boundary layer development along the plate leading to the gage. Equation 5.14 then reduces to

$$S_{conv} = \frac{S_{abs}}{1 + h_p R''} \quad (5.18)$$

The red line in Fig. 5.12 represents the least squares curve fit of this equation for R'' while forcing the curve through the radiation calibration point at $h_p = 0$. The corresponding values of R'' for all of the gages are listed in Table 5.1, along with the associated uncertainties. The uncertainty values are rather large because R'' is obtained from a curve fit of the sensitivity data, which amplifies the individual uncertainties. As expected, the gage with the lowest radiation sensitivity has the smallest internal resistance, R'' . In addition, the physically larger gages have higher internal resistance. The values reported are consistent with the expected thermal resistances of the aluminium wafer and potting material in the Schmidt-Boelter gages [4]. They are of the same form, but generally lower than the values for comparable Gardon gages [8].

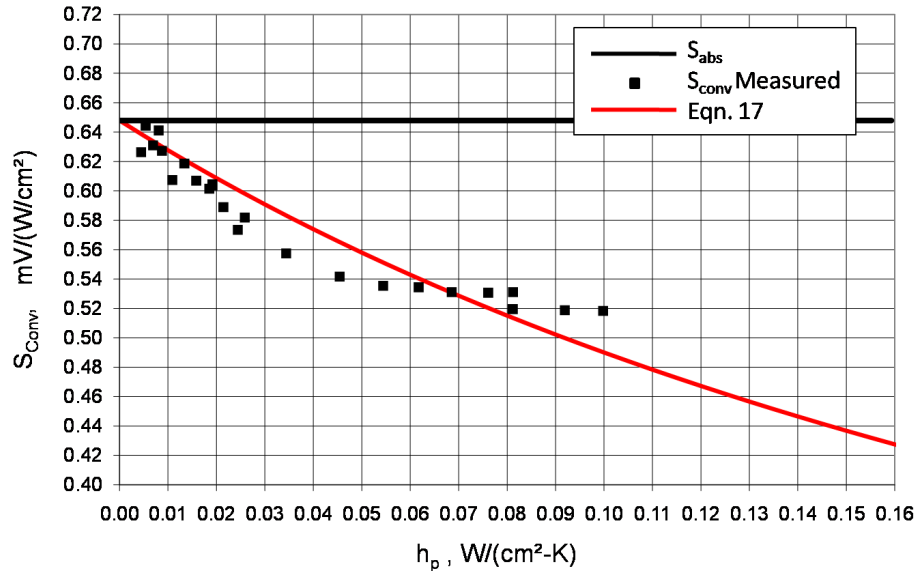


Figure 5.12: Stagnation calibration sensitivities for SB137861 in stagnation flow

Sensor	$S_{abs} \left(\frac{mV}{W/cm^2} \right)$	$R'' \left(\frac{cm^2 K}{W} \right)$	R'' Uncertainty (%)
1.0 in. SB 137861	0.648	3.22	56
1.0 in. SB 137864	0.428	2.65	66
1.0 in. SB 142781-T	0.681	5.78	34
1.0 in. SB 142782-T	0.782	5.42	36

Table 5.1: Summary of stagnation calibration results

The results for shear flow were done to observe the effects of the gage temperature distribution on the heat transfer coefficient. As discussed in the introduction, this is an important effect in boundary layer flows. It is anticipated that the effective heat transfer coefficient over the gage will be decreased by the smaller difference in gage temperature relative to that of the surrounding plate. To observe this effect the theoretical curve in equation 5.14 was used to fit the data, assuming that the value of R'' remained the same as for the stagnation tests. The equation was then fit to the data using h_p/h_g as the variable parameter. Figure 5.13 shows an example of the results for the same gage as shown in stagnation flow in Fig. 5.12. The average experimental uncertainty of the measured sensitivity values was estimated to 11.6%. The largest contribution to the uncertainty was an estimated 10% uncertainty in the heat transfer coefficient between the two nozzles.

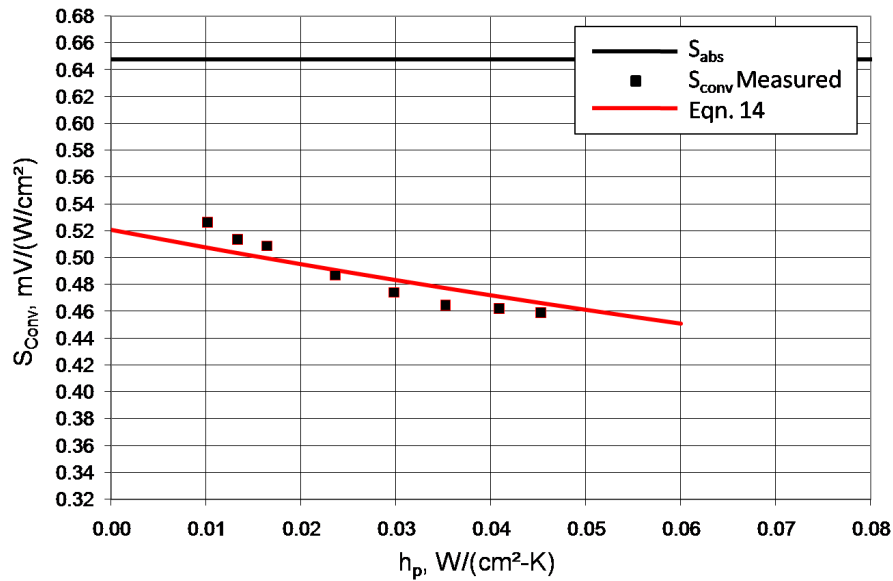


Figure 5.13: Calibration sensitivities for SB 137861 in shear flow

The values of h_p/h_g obtained for all four gages are listed in Table 5.2 with the corresponding values of estimated uncertainty. The largest contribution to the uncertainty is from the measured gage sensitivity. As expected, the lowest value (smallest temperature effect) is for the gage with the lowest sensitivity. All of the values are not far from one, which is typical of turbulent boundary layers over the relatively small dimensions of the heat flux gages.

The ratio h_p/h_g was assumed constant for each gage even though a wide range of h_p values was used. Because the value of this ratio is probably a combination of gage geometry and flow effects, there may be a second-order effect of h_p on h_p/h_g . The constant value assumption, however, is validated by the good fit of the curve with the data, certainly within experimental uncertainty.

5.11.1 Effects of Water Cooling

Schmidt-Boelter heat flux gages are often operated with water cooling when used in hot environments. This alters the internal heat transfer pathways and could affect the apparent thermal resistances and heat flux measured by the gage. Therefore, the

Sensor	$S_{abs} \left(\frac{mV}{W/cm^2} \right)$	$\frac{h_p}{h_g}$	$\frac{h_p}{h_g}$ Uncertainty (%)
1.0 in. SB 137861	0.648	1.24	17
1.0 in. SB 137864	0.428	1.14	16
1.0 in. SB 142781-T	0.681	1.20	18
1.0 in. SB 142782-T	0.782	1.16	17

Table 5.2: Ratio of heat transfer coefficients for shear flow

calibration tests were repeated with water cooling to further characterize the gage response.

Fig. 5.14 shows the sensitivities for stagnation flow, both with and without water cooling for comparison. Moreover, when water cooling is introduced, the water temperature is another possible sink temperature for reducing the data, in addition to the plate temperature. Therefore, the data are shown in Fig. 5.14 for both possible heat sink temperatures. Because the water temperature was constant at room temperature (30C), the results generally straddle the uncooled case. The actual sensor temperature is now lower than the plate temperature because of the lower temperature water cooling, but always higher than the water temperature itself. Consequently, because of the larger actual temperature difference the heat flux and corresponding sensitivity will be higher than the uncooled case when using the plate temperature. The opposite is true when using the water temperature as the heat sink. The gage temperature difference $T_\infty - T_g$ is then smaller than $T_\infty - T_s$, giving a smaller gage heat flux and lower apparent gage sensitivity.

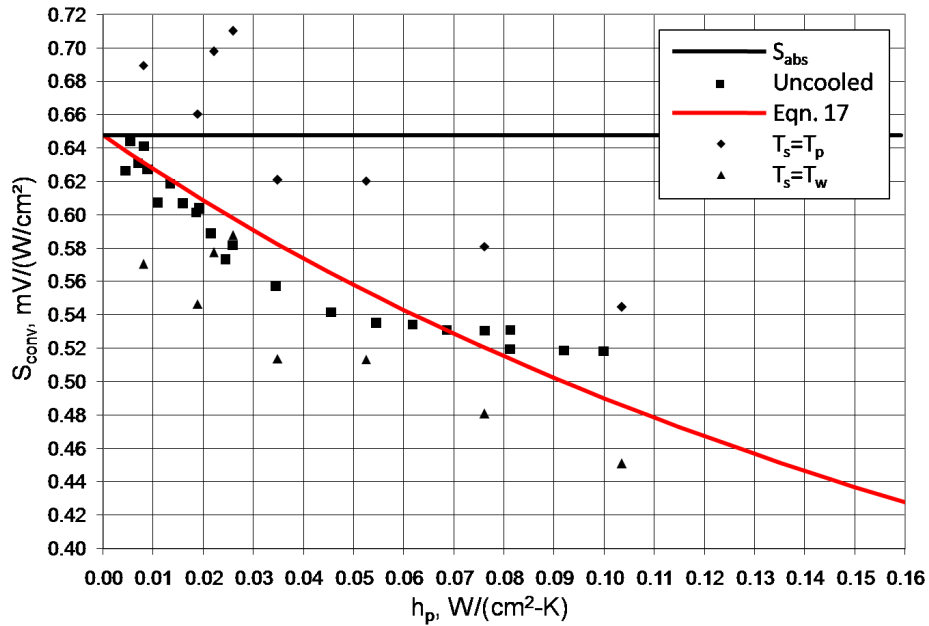


Figure 5.14: Stagnation calibration sensitivities for SB 137861 in stagnation flow with water cooling

The corresponding results for shear flow are shown in Fig. 5.15. The trends are quite different. When using the water temperature to define the heat flux, the sensitivity is close to the uncooled case. The sensitivities when using the plate tem-

perature, however, are much higher. In fact, the results for water cooling using the plate temperature actually appear to match the radiation sensitivity! The water cooled copper casing around the blackened sensor can be seen in Fig. 5.8. As the heated flow first goes over the aluminum plate, then the water-cooled copper gage, the temperature difference is increasing, which increases the heat flux and apparent sensitivity. This is somewhat balanced by the effect on the boundary layer of the varying temperatures. The result is a sensitivity using the plate temperature that is higher than the uncooled case and nearly that of the radiation calibration. For the case of the 38 – mm diameter gages the water cooling is higher than the radiation line by up to 10%. It is important to note that the sensitivity for water cooling is dependent on the temperature of the cooling water among other variables and would not be the same for other conditions. In summary, it appears that the matched sensitivities with the radiation calibration is more by chance of the test conditions than a characteristic of the gage.

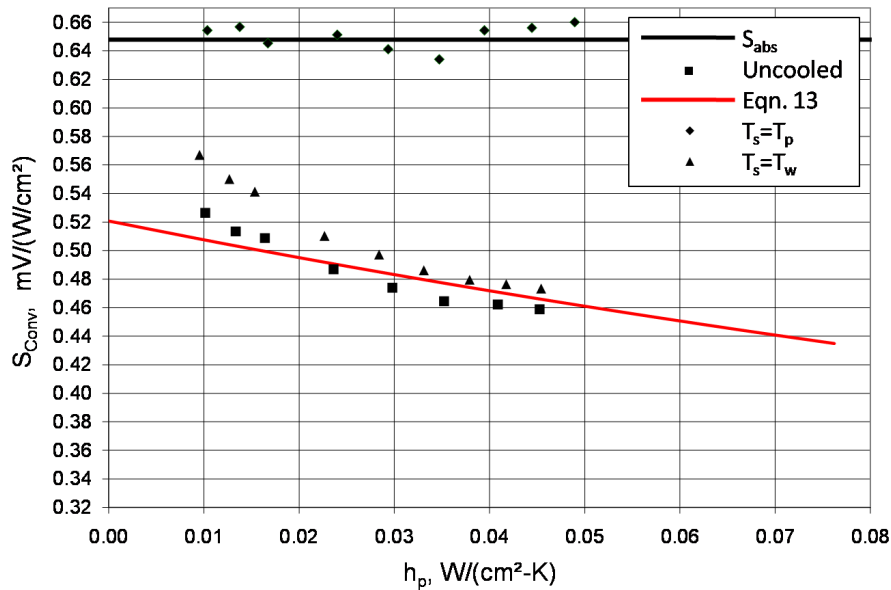


Figure 5.15: Calibration sensitivities for SB 137861 in shear flow with water cooling

5.12 Conclusions and Recommendations

A convective heat flux calibration system that provides measurements in both stagnation and shear flows was developed and tested. This was used to show that Schmidt-Boelter heat flux gage sensitivities obtained in convection are different from those obtained by the standard radiation calibration. A model equation based on internal and external thermal resistances provides a good explanation for the dependence of the apparent gage sensitivity on the heat transfer coefficient. The internal resistance R'' in this model is based on the material properties of the gage, as measured in stagnation flow. Additional thermal effects of the gage on the boundary layer were measured in shear flow and characterized by the ratio h_p/h_g . The experimental results matched the model and were used to estimate values of these two parameters for the four Schmidt-Boelter gages tested, although the uncertainties were high for R'' .

Differences between the calibrations with stagnation and shear flow were further amplified when water cooling of the gage was introduced. This factor complicates interpretation of the results for convective flows. A detailed understanding of the temperature distribution around the gage would be helpful to obtain an understanding of the gage operation. For example, this could be achieved with 3-D computational modeling and an experimental surface temperature mapping system.

5.13 Acknowledgments

Funding for this work was provided by Sandia National Labs through program managers Jim Nakos and Tom Blanchet.

5.14 References

1. Diller, T. E., "Advances in Heat Flux Measurements," *Advances in Heat Transfer*, Vol. 23, Academic Press, Boston, 1993.
2. Kuo, C. H. and Kulkarni, A. K., "Analysis of Heat Flux Measurement by Circular Foil Gages in Mixed Convection/Radiation Environment," *ASME Journal of Heat Transfer*, Vol.113, 1991, pp. 1037-1040.
3. Holmberg, D. G. and Diller, T. E., "High-Frequency Heat Flux Sensor Calibration and Modelling," *ASME Journal of Fluids Engineering*, Vol. 127, 1995, pp 502-506.
4. Kidd, C. T. and Nelson, C. G., "How the Schmidt-Boelter Gage Really Works," *Proc. 41st International Instrumentation Symposium, ISA*, Research Triangle Park, 1995, pp. 347-368.
5. Murthy, A. V., Fraser, G. T., and De Witt, D. P., "Experimental In-Cavity Radiative Calibration of High-Heat-Flux Meters," *AIAA Journal of Thermophysics and Heat Transfer*, Vol. 20, 2006, pp. 327-335.
6. Hoffie, Andreas, "Convection Calibration of Schmidt-Boelter Heat Flux Gages in Shear and Stagnation Air Flows," *MS Thesis, Virginia Tech, Blacksburg, VA*, 2006.
7. Taylor, B. B and Kuyatt, C. E., "Guidelines for Evaluating and Expressing the Uncertainty of NIST Measurement Results," *NIST Technical Note 1297*, 1994.
8. Borell, G. J. and Diller, T. E., "A Convection Calibration Method for Local Heat Flux Gages," *ASME Journal of Heat Transfer*, Vol. 109, 1987, pp. 83-89.

Chapter 6

Conclusions and Recommendations for Future Research

6.1 Conclusions

Several important conclusions may be made regarding the results presented in this dissertation. As revealed in Chapters 2, coherent structures play an important role in the augmentation of heat transfer. Identifying and tracking coherent structures within the TRDPIV flow field provides evidence that is consistent with the current theory of vorticity amplification in the stagnation region. It was hypothesized that heat transfer augmentation occurs when coherent structures sweep cold fluid from the freestream directly into the heated boundary layer region. This is indeed the case, as evidenced by the success of a mechanistic model based on this premise. The incorporation of integral length scale, circulation strength, and core-to-surface distance of coherent structures into the mechanistic model lead to accurate predictions of the transient and time-average turbulent heat transfer coefficients measured experimentally with the HFA sensor. These results were further validated in Chapter 3 using an improved model based on a cumulative induced velocity method. Trend analysis of coherent structure properties versus measured heat transfer confirmed that the form and function of the model are indeed valid.

The HTHFS heat flux sensor described in Chapter 4 represents the state-of-the-art in high temperature, long-lasting heat flux sensing technology. This sensor was successfully designed and constructed using high temperature thermoelectric elements and insulators in a surface mountable configuration. The sensor was calibrated in both conduction and convection using custom designed calibration facilities. Experimental sensitivities from the calibration facilities were nearly identical to the values predicted using simple analysis and a 1-D thermal resistance model of the sensor. The HTHFS performed very well after being subjected to numerous thermal cycling tests involving kiln firing and propane torch applications.

As reported in Chapter 5, two varieties of Schmidt-Boelter heat flux sensors were extensively calibrated in both shear and stagnation flow using newly developed convection calibration facilities. These calibration studies reveal that Schmidt-Boelter heat flux sensors have markedly different sensitivities in convection than in the standard case of radiation calibration. The sensitivity in both stagnation and shear flow decreases with heat transfer coefficient, with a more pronounced effect on calibrations in shear flow. The dependence of gage sensitivity on heat transfer coefficient is shown to be a direct result of internal and external thermal resistances. These effects are successfully quantified using an analytical sensitivity model. Finally, it is shown that water-cooling Schmidt-Boelter heat flux sensors leads to increased differences in sensitivity between shear and stagnation flows.

6.2 Recommendations for Future Research

A great deal of exciting and potentially ground-breaking research is within sight on several of the projects covered in this dissertation. As shown in Chapter 2 extensive baseline work has been completed on the effects of freestream turbulence on stagnation point heat transfer. Consequently this will enable many more interesting studies in the future. One such series of studies could provide a very useful and comprehensive set of correlation curves for heat transfer engineering design purposes, and also bridge the gap between local coherent structure properties on the stagnation plate and the turbulence characteristics of the freestream. First, we could obtain simultaneous TRDPIV and heat transfer measurements at a fixed Reynolds number, while varying both turbulence intensity, $\overline{T}u_\infty$, and integral length scale, $\overline{\Lambda}_\infty$. This is easily done since freestream turbulence parameters could be systematically varied using any one of three fully characterized turbulence grids. A parametric space could be developed showing contours of time-averaged heat transfer augmentation, $\overline{\Delta h_{turb}}$, at various levels of freestream turbulence intensity and integral lengths scale. Time and money permitting the same experiments could be repeated for different Reynolds numbers. The end result would be a very comprehensive series of heat transfer correlations that are more in-depth than ever done before. In traditional fashion an engineer could pick the freestream turbulence parameters present in their particular problem at a given Reynolds number and simply look up the associated heat transfer augmentation. Granted these results would only be valid for body shapes having a deceleration term similar to that found in our stagnation studies $a \sim 0.6(1/s)$. The TRDPIV data from these same parametric experiments would also reveal a great deal of information about the behavior of coherent structures in the stagnation region. As discussed in Chapter 3 the mean vortex size and circulation strength in the stagnation region follow identifiable trends when compared to the measured heat transfer augmentation. With further analysis these structures may be correlated to the freestream turbulence properties via amplification ratios. Therefore, an analogous series of contours and correlations could be generated based on these locally derived quantities.

The prospects for the high temperature heat flux sensor are equally high. As discussed in Chapter 4 the HTHFS has been successfully prototyped and evaluated in a surface mountable configuration. The basic design is extremely durable and reliable even after extensive thermal cycling via torch applications. There has been great interest in taking the HTHFS concept to the next level, i.e. miniaturizing the entire sensor to achieve high frequency response. A variety of approaches to miniaturization can be examined. One approach, leveraging the capabilities of the local Blacksburg business, Nuvotronics, would involve fabrication of separate, basic HTHFS structures, i.e. an Alumel/Insulation/Chromel group, using proprietary semiconductor fabrication technologies. These basic structures could then be welded together in any number to achieve the desired levels of output. Preliminary discussions of that approach places the sensor dimensions at $0.25mm \times 2.0mm \times 2.0mm (H \times L \times W)$. A sensor with this thickness would have a frequency response on the order of $50Hz$. This would be a substantial increase in sensor performance for the HTHFS, and would likely capture a large share of the market for high temperature heat flux sensors that can last long periods of time in harsh environments. Once this manufacturing approach is perfected, a variety of sensor mounting options could be examined. This would include surface-mountable housings and plug-type varieties. Another interesting avenue of study would be embedding the sensor in aerospace or industrial equipment for structural health/performance monitoring purposes.

As mentioned previously, there is no uniform standard for the accurate calibration of heat flux sensors in single or mixed modes of heat transfer. Hence, there is a great deal of research that may be done towards increasing the uniformity and accuracy of heat flux calibrations. The current generation of shear and stagnation calibration facilities at Virginia Tech are a solid foundation for future convection calibration studies. With some modifications, the convection calibration facilities could become

the standard for calibrations in turbulent shear and stagnation flow. For instance, if the bias errors associated with the reference standard gages used in each facility could be eliminated, the total uncertainty in calibrations for each facility could be reduced by up to 5%! Likewise, a more accurate surface temperature measurement capability would allow for more accurate assessment of the reference heat transfer coefficient. The shear stand in particular will require modifications to improve uniformity in flow and heat transfer characteristics from nozzle to nozzle. This currently is the largest source of calibration error. Once modifications to each facility are complete, a great deal of experimental studies can be envisioned.

Appendix A

Computational Codes

```

%"HeatTransferReduction.m" Created by Andrew Gifford
%Purpose: This code was designed to import and reduce the heat transfer
%data obtained by the HFA sensor and associated thermocouples.
%The primary output from this code includes time-averaged heat transfer
%quantities and various plots.

clc
clear all
close all
%%%%%%%%%%%%%%%%%%%%%%%%%%%%%%%%%%%%%%%%%%%%%%%%%%%%%%%%%%%%%%%%%%%%%%%%
%%%%%%%%%%%%%%%%%%%%%%%%%%%%%%%%%%%%%%%%%%%%%%%%%%%%%%%%%%%%%%%%%%%%%%%%
%Import data from text file:
FSVel=0.1;           %Freestream mean velocity(m/s)
TcFS=24.04;         %Freestream temperature (Deg C)
Fs=1000;           %Original heat transfer sampling rate
AMP=1000;          %Amplification of custom amplifier board
Sens=42.6*10^(-6); %TFHFG Sensitivity (microV/W/cm^2)
filename='10cms_Small_Grid2_Heated_Plate_T2_xMU17_3_Horz.txt';
direc=['P:\Feb 6 Tests\Heat Transfer\'];
fid = fopen([direc filename]);
for z=1:22
    tempz=fgetl(fid);
end
a = fscanf(fid,'%g %g %g %g %g %g %g %g %g %g %g',[11,inf]);
fclose(fid);
t=a(1,:);
qV=a(8,:);
TSV=a(3,:);
qVb=a(2,:);
CV=a(4,:);
hcomp=a(7,:);
clear a
pack
%%%%%%%%%%%%%%%%%%%%%%%%%%%%%%%%%%%%%%%%%%%%%%%%%%%%%%%%%%%%%%%%%%%%%%%%
%Find the exact starting and ending times for the PIV camera signal.
%This will create a truncated heat flux signal corresponding to
%the time period where TRDPIV was acquired.
index=[1:1:length(t)];
figure
hold on
ylim([-0.5 3.0])
plot(index,qV,'k')
plot(index,CV)
xlabel('Index #')
ylabel('Voltage')
legend('Heat Flux','Camera')
disp('Look at figure. Use data cursur to find start and end of Camera Signal.
Export these to workspace as time1 and time2')
disp('Close figure and hit enter to resume after pause. The indices will be
shown and you can follow prompts from there')
pause
timeon = input('Enter the index where the camera turns on at:');
timeoff = input('Enter the index where the camera turns off at:');
time_heatflux_piv=t(timeon:1:timeoff);
heatflux_piv=qV(timeon:1:timeoff);
Tsurf_piv=TSV(timeon:1:timeoff);
%%%%%%%%%%%%%%%%%%%%%%%%%%%%%%%%%%%%%%%%%%%%%%%%%%%%%%%%%%%%%%%%%%%%%%%%

```

```

%Calculate mean heat flux signal at zero heating rate and no turbulence
qVDCO=mean(qV(1:1000));
%Convert voltage to heat flux, divide out amplification, and
%subtract off the DC offset in the heat flux:
heatflux_piv=((heatflux_piv-qVDCO)/AMP)/Sens;
qV=((qV-qVDCO)/AMP)/Sens;
%Low Pass Filter the data to within frequency response of gage:
[b3,a3]=ellip(9,0.5,50,30/500);
heatflux_pivF=filtfilt(b3,a3,heatflux_piv);
Tsurf_pivF=filtfilt(b3,a3,Tsurf_piv);
qVF=filtfilt(b3,a3,qV);
TSVF=filtfilt(b3,a3,TSV);
%Calculate Heat Transfer Coefficient for downsampled and filtered data:
%Three seconds on either side of piv range:
LT1=timeon-10000;
LT2=timeoff+10000;
time_Long=t(LT1:LT2);
heatflux_Long=qVF(LT1:LT2);
Tsurf_Long=TSVF(LT1:LT2);
hCalc_Long=heatflux_Long./(Tsurf_Long-TcFS);
hCalc_pivF=heatflux_pivF./(Tsurf_pivF-TcFS);
%This figure shows downsampled and filtered signals for comparison:
figure
[AX,H1,H2] =
plotyy(time_heatflux_piv,heatflux_pivF,time_heatflux_piv,Tsurf_pivF,'plot')
set(get(AX(1),'Ylabel'),'string','Heat Flux (W/cm^2)')
set(get(AX(2),'Ylabel'),'string','Surface Temp (Deg. C)')
title('Downsampled and Filtered Heat Flux and Surface Temperature Signals
Simult. TRDPIV')
xlabel('Time (s)')
%Calculate mean heat transfer quantities:
h_ave=mean(hCalc_pivF);
h_aveLong=mean(hCalc_Long);
q_ave=mean(heatflux_pivF);
q_aveLong=mean(heatflux_Long);
DT_ave=mean(TSVF-TcFS);
TFilm=(mean(TSVF)+TcFS)/2;
%Look-up table for freestream thermodynamic properties:
Ttable=[273.15 280 290 295 300 305 310 315 320 325]';%(K)
ktable=[0.569 .582 .589 .606 .613 .620 .628 .634 .640 .645]';%(W/mK)
Prtable=[12.99 10.26 7.56 6.62 5.83 5.20 4.62 4.16 3.77 3.42]';%(ND)
Viscosity=[0.001750 0.001422 0.001080 0.000959 0.000855 0.000769 0.000695
0.000631 0.000577 0.000528]';%(Ns/m^2)
specvol=[0.001 0.001 0.001001 0.001002 0.001003 0.001005 0.001007 0.001009
0.001011 0.001013]';%(m^3/kg)
%Plate Temperature Based:
Pr1=interp1(Ttable(:,1),Prtable(:,1),(mean(TSVF)+273.15));%(ND)
k1=interp1(Ttable(:,1),ktable(:,1),(mean(TSVF)+273.15));%(W/mK)
kNu1=(interp1(Ttable(:,1),Viscosity(:,1),(mean(TSVF)+273.15)))*(interp1(Ttable(:,1),specvol(:,1),(mean(TSVF)+273.15)));%(m^2/s)
%Film Temperature Based:
Pr2=interp1(Ttable(:,1),Prtable(:,1),(TFilm+273.15));%(ND)
k2=interp1(Ttable(:,1),ktable(:,1),(TFilm+273.15));%(W/mK)
kNu2=(interp1(Ttable(:,1),Viscosity(:,1),(TFilm+273.15)))*(interp1(Ttable(:,1),specvol(:,1),(TFilm+273.15)));%(m^2/s)
%Save time-averaged heat transfer quantities:
save Mean_DT_Value DT_ave -ASCII

```

```

save Mean_TFilm TFilm -ASCII
save Mean_kNu1 kNu1 -ASCII
save Mean_kNu2 kNu2 -ASCII
save Mean_q_Value q_ave -ASCII
save Mean_q_ValueLong q_aveLong -ASCII
save Mean_h_Value h_ave -ASCII
save Mean_h_ValueLong h_aveLong -ASCII
save Mean_k_Value1 k1 -ASCII
save Mean_Pr_Value1 Pr1 -ASCII
save Mean_k_Value2 k2 -ASCII
save Mean_Pr_Value2 Pr2 -ASCII
%Save the transient heat transfer data:
Concurrent_TRDPIV_HF_Data=[time_heatflux_piv;heatflux_pivF;hCalc_pivF;Tsurf_pivF];
save Concurrent_TRDPIV_HF_Data.mat Concurrent_TRDPIV_HF_Data

%"TRDPIVReduction.m" Created by Andrew Gifford
%Purpose: This code was designed to import and reduce the TRDPIV data.
%Velocity field data is imported from three dimensional arrays of U and V
%velocities which are generated from a POD reduction scheme. Turbulence
%quantities and coherence values are generated. The POD reduction codes are
%general use in the AETHER laboratory and may be obtained with permission of
%the author(s) upon request.

%%%%%%%%%%%%%%%%%%%%%%%%%%%%%%%%%%%%%%%%%%%%%%%%%%%%%%%%%%%%%%%%%%%%%%%%
%%%%%%%%%%%%%%%%%%%%%%%%%%%%%%%%%%%%%%%%%%%%%%%%%%%%%%%%%%%%%%%%%%%%%%%%

clear all
close all
clc

%Load the POD reduced velocity component arrays:
load('UData')
load('VData')

%Optinon to choose slice of data in y-direction
[Ly Lx Lz]=size(uvec);
ylim1=1;
ylim2=Ly;%Default
ymax=(ylim2-ylim1)+1;
lagt=ylim1-1;
numvects_x = Lx;
numvects_y = Ly;

%TRDPIV data set and flow properties:
FSVel=0.1; %Freestream velocity, m/s
Magnification=105.25; %Image magnification, microns/pixel
ModMag=Magnification*10^(-6); %Image magnification, meters/pixel
timeskip=1; %Pic a time skip if needed
startframe=1; %Starting frame (time)
endframe=3768; %Ending frame (time)
Fs=62.5; %Sampling frequency between time steps
FsV=125; %Time Separation between correlation images
NOT Fs ABOVE!!!
finalfreq=Fs/timeskip; %Final frequency of data set used in
processing

```

```

gridspace=4;                                %Vector spacing in TRDPIV data field

%Generate vector containing sample time instances:
numframestot=round(((endframe-startframe)+1)/timeskip);
time(1)=0;
for z=2:1:numframestot
    time(z)=(1/Fs)*(z-1);
end

%Load thermal properties and heat transfer data for model prediction
%purposes:
load('Concurrent_TRDPIV_HF_DataG1T2.mat');
Pr=load('-ascii', 'Mean_Pr_Value1');
k=load('-ascii', 'Mean_k_Value1');
knu=load('-ascii', 'Mean_kNu1');
alpha=knu/Pr;
HF=Concurrent_TRDPIV_HF_Data(3,:);
HFtime=Concurrent_TRDPIV_HF_Data(1,:);

pack
tic
%Zero out matrices to allow for faster processing:
VelMean=zeros(numvects_y,numvects_x);
C1=zeros(ymax,numvects_x);
C2=zeros(ymax,numvects_x);
C3=zeros(ymax,numvects_x);
f1=zeros(ymax,numvects_x);
f2=zeros(ymax,numvects_x);
f3=zeros(ymax,numvects_x);
urms=zeros(ymax,numvects_x);
Tux=zeros(ymax,numvects_x);
Tux2=zeros(ymax,numvects_x);
T1a=zeros(ymax,numvects_x);
L1a=zeros(ymax,numvects_x);
L2a=zeros(ymax,numvects_x);
C1opt=zeros(ymax,numvects_x);
L1b=zeros(ymax,numvects_x);
L2b=zeros(ymax,numvects_x);
T1c=zeros(ymax,numvects_x);
L1c=zeros(ymax,numvects_x);
L2c=zeros(ymax,numvects_x);
dh1=zeros(ymax,numvects_x);
dh2=zeros(ymax,numvects_x);
dh3=zeros(ymax,numvects_x);
dh4=zeros(ymax,numvects_x);
dh5=zeros(ymax,numvects_x);
dh6=zeros(ymax,numvects_x);
VelMeanv=zeros(numvects_y,numvects_x);
C1v=zeros(ymax,numvects_x);
C2v=zeros(ymax,numvects_x);
C3v=zeros(ymax,numvects_x);
f1v=zeros(ymax,numvects_x);
f2v=zeros(ymax,numvects_x);
f3v=zeros(ymax,numvects_x);
vrms=zeros(ymax,numvects_x);
Tuy=zeros(ymax,numvects_x);
Tuy2=zeros(ymax,numvects_x);

```

```

T1av=zeros(ymax,numvects_x);
L1av=zeros(ymax,numvects_x);
L2av=zeros(ymax,numvects_x);
Cloptv=zeros(ymax,numvects_x);
L1bv=zeros(ymax,numvects_x);
L2bv=zeros(ymax,numvects_x);
T1cv=zeros(ymax,numvects_x);
L1cv=zeros(ymax,numvects_x);
L2cv=zeros(ymax,numvects_x);
dh1v=zeros(ymax,numvects_x);
dh2v=zeros(ymax,numvects_x);
dh3v=zeros(ymax,numvects_x);
dh4v=zeros(ymax,numvects_x);
dh5v=zeros(ymax,numvects_x);
dh6v=zeros(ymax,numvects_x);
%For each vector location calculate all pertinent properties:
for b=1:1:ymax
    for h=1:1:numvects_x
        %Zero phase distorted data and convert to m/s
        udata = decimate(uvec(b,h,:),timeskip)*ModMag*FsV;
        vdata = decimate(vvec(b,h,:),timeskip)*ModMag*FsV;
        %Downsample all data to TRDPIV data frequency:
        DS_time=downsample(time,timeskip);
        DS_HF=decimate(HF,1000/finalfreq);
        DS_HFtime=downsample(HFtime,1000/finalfreq);
        if length(DS_HF)>=length(udata)
            DS_HF=DS_HF(1:length(udata),1);
            DS_HFtime=DS_HFtime(1:length(udata),1);
        else
            udata=udata(1:length(DS_HF));
            vdata=vdata(1:length(DS_HF));
            DS_time=DS_time(1:length(DS_HF));
        end
        %Temporary mean-removed data sequences:
        tempu=udata-mean(udata);
        tempv=vdata-mean(vdata);
        %Mean velocity components at current point in flow field:
        VelMean(b+lagt,h)=mean(udata);
        VelMeanv(b+lagt,h)=mean(vdata);
        %Call GlobalCoherence.m to calculate flow and heat transfer signal
        %coherence at current point in flow field:
        [C1(b+lagt,h),C2(b+lagt,h),C3(b+lagt,h),f1(b+lagt,h),f2(b+lagt,h),...
        f3(b+lagt,h)]=GlobalCoherence(tempu,DS_HF-mean(DS_HF)',finalfreq);
        [C1v(b+lagt,h),C2v(b+lagt,h),C3v(b+lagt,h),f1v(b+lagt,h),f2v(b+lagt,h),...
        f3v(b+lagt,h)]=GlobalCoherence(tempv,DS_HF-mean(DS_HF)',finalfreq);
        %RMS velocity componet values at current point in flow field:
        urms(b+lagt,h)=sqrt(mean((tempu).^2));
        vrms(b+lagt,h)=sqrt(mean((tempv).^2));
        %Turbulencies intensities:
        Tux(b+lagt,h)=urms(b+lagt,h)/VelMean(b+lagt,h);
        Tuy(b+lagt,h)=vrms(b+lagt,h)/VelMeanv(b+lagt,h);
        %Integral length scales using first-zero-crossing method:
        [L1au(b+lagt,h),L2au(b+lagt,h)]=L1_FZCM(tempu,udata,finalfreq,FSVel);
        [L1av(b+lagt,h),L2av(b+lagt,h)]=L1_FZCM(tempv,vdata,finalfreq,FSVel);
        %Nix, Diller model calculation for heat transfer augmentation:
        [dh1(b+lagt,h)]=...
ModelDh(urms(b+lagt,h),L1au(b+lagt,h),k,alpha); %W/cm^2-C

```

```

    [dh2(b+lagt,h)]=...
ModelDh(vrms(b+lagt,h),Llav(b+lagt,h),k,alpha);%W/cm^2-C
    end
end

toc

```

```

%"GlobalCoherence.m" written by Andrew Gifford
%This function accepts the time series of two signals and determines three
%levels of coherence between the two signals according to the formula:
%C(f)=|Rsig1,sig2|^2/|Rsig1,sig1||Rsig2,sig2|
%The coherence typically has a dominant peak followed by several lesser
%peaks. The peak indicates that the two signals share large amounts of
%energy at the given peak's frequency.

```

```

function [C1,C2,C3,f1,f2,f3]=GlobalCoherence(sig1,sig2,fs)
sig3=cat(3,cat(3,sig1,sig1),sig1);%Four times repeated signal to gain freq
resolution
sig4=cat(3,cat(3,sig2,sig2),sig2);%Four times repeated signal to gain freq
resolution
n=length(sig3);      %length of time series
fchar=0.25;          %frequency you are trying to resolve (Hz)
e=2;                 %Number of events at fchar to study in a given cpsd
window
tau=e*(1/fchar);    %time span for segment
win=tau/(1/fs);     %window size
ovlp_perc=0.50;     %window overlap percentage
ovlp=ovlp_perc*win; %window overlap
[pxx,fxx]=cpsd(sig3,sig3,win,ovlp,[],fs);%Individual cross-power spectrums
[pyy,fyy]=cpsd(sig4,sig4,win,ovlp,[],fs);%Individual cross-power spectrums
[pxy,fxy]=cpsd(sig3,sig4,win,ovlp,[],fs);%Individual cross-power spectrums
%Frequencies used to estimate cross-power spectrums:
f=fxx;
%Coherence values at each frequency:
C=(pxy.*conj(pxy))./(pxx.*pyy);
%Alternative function built into Matlab may be used:
% [C,f] = mscohere(sig3,sig4,win,ovlp,[],fs,'onesided');
for tt=1:1:length(C)
    if isnan(C(tt))==1 || isnan(f(tt))==1
        C(tt)=0;
        f(tt)=0;
    else
        end
end
end
[ind,peaks] = findpeaks(C);
[B,IX] = sort((peaks),'descend');
if isempty(B)==1
    %Level one coherence
    C1=0;
    f1=0;
    %Level two coherence
    C2=0;
    f2=0;
    %Level two coherence
    C3=0;

```

```

    f3=0;
elseif length(B)==1
    for kk=1:1:length(ind);
        newind(kk)=ind(IX(kk));
    end
    %Level one coherence
    C1=B(1);
    f1=f(newind(1));
    %Level two coherence
    C2=0;
    f2=0;
    %Level three coherence
    C3=0;
    f3=0;
elseif length(B)==2
    for kk=1:1:length(ind);
        newind(kk)=ind(IX(kk));
    end
    %Level one coherence
    C1=B(1);
    f1=f(newind(1));
    %Level two coherence
    C2=B(2);
    f2=f(newind(2));
    %Level three coherence
    C3=0;
    f3=0;
else
    for kk=1:1:length(ind);
        newind(kk)=ind(IX(kk));
    end
    %Level one coherence
    C1=B(1);
    f1=f(newind(1));
    %Level two coherence
    C2=B(2);
    f2=f(newind(2));
    %Level three coherence
    C3=B(3);
    f3=f(newind(3));
end
end

```

```

%"L1_FZCM.m" written by Andrew Gifford
%This function calculates the integral length scale from the transient
%velocity history at a point in the flowfield.
function [L1,L2]=L1_FZCM(sig1,sigtot,Fs,Uinf)

```

```

%Perform auto-correlation of signal:
[R,Rx]=xcorr(sig1,'coeff');
%Extract positive ranges:
R=R(round(length(Rx)/2):length(Rx));
Rx=Rx(round(length(Rx)/2):length(Rx));
%Find first zero crossing if present:
MinVal=find(R<=0);
taumin=MinVal(1);

```

```

%Take total range if needed:
if isempty(taumin)
    taumin(1)=max(Rx);
else
end
%Calculate integral length scales based on freestream velocity and local
%mean velocity:
T1a=trapz(R(1:taumin(1)))*(1/Fs);
L1=T1a*Uinf;
L2=abs(T1a*mean(sigttotal));
%Optional viewing of xcorr results:
% figure
% hold on
% plot(Rx,R)
% plot(taumin(1),R(taumin(1)),'*')

%"ModelDh.m" written by Andrew Gifford
%This function calculates the predicted heat transfer augmentation due to
%coherent structure interaction using the model developed by Nix et al.

function [dh]=ModelDh(urms,L,k,alpha)
dh=(k/sqrt((pi*(alpha)*(L/urms)))/100^2; %W/cm^2-C

%"VortexIdentificationScheme.m" originally formulated by Chris Weiland and
%modified by Andrew Gifford for use with a vortex tracking code.
%This code is used to identify coherent structures within the TRDPIV
%flowfield using a variety of methods, providing circulation and location.
%The code and sub-function were modified to better identify and store these
%identified vortices in time-stamped arrays for later use in vortex
%tracking schemes.
clear all
close all
clc

%Pertinent input parameters:
FSVel=0.1; %Freestream Mean Velocity(m/s)
timeskip=1; %Time skip if needed
startframe=1; %Start frame number
endframe=3768; %End frame number
Fs=62.5; %Frequency of frames
numframestot=round(((endframe-startframe)+1)); %Total # of frames
Magnification=105.25;%image magnification micron/pixel
ModMag=105.25e-6; %image magnification meters/pixel
vector_spacing=4; %Original vector grid spacing
%Set the location of the HFA sensor of choice:
gagelocy=106.5*vector_spacing*Magnification*100/(10^6);%(cm);
gagelocx=173*vector_spacing*Magnification*100/(10^6);%(cm);
%Choose method of velocity gradient estimation for ID schemes:
gradient_method='sec_order';
vortex_method='Dcrit';
%Initialize variables:
vort_loc_mat_t=[0];
rowstart=1;

```

```

vort_vec=[0];
graymap=flipud(gray(numframestot));
maxvorts=0;
graymon
%Set limits of velocity field vectors and generate a grid:
numvects_x=173;
numvects_y=207;
[X,Y] = meshgrid(1:1:numvects_x,1:1:numvects_y);
%Calculate physical space vectors for plotting:
X=X*vector_spacing*Magnification*100/(10^6);%(cm)
Y=Y*vector_spacing*Magnification*100/(10^6);%(cm)
%Time Separation between correlation images used to calculate velocities:
FsV=125;
%For each time step look for and identify coherent structures, calculate
%circulation and location relative to HFA heat flux sensor, and examine
%plot feedback to determine CS identification filtering levels. The input
%velocity component fields are found using "Velocity.m" script:
for k=1:timeskip:numframestot
    temp_nameu=strcat('uVelsFrame',num2str(k));
    temp_namev=strcat('vVelsFrame',num2str(k));
    uvec=load(temp_nameu,'-ascii');
    vvec=load(temp_namev,'-ascii');
    uvec=uvec*ModMag*FsV;%m/s
    vvec=vvec*ModMag*FsV;%m/s
    %Call vortex_computation to determine the x and y coordinates of all
    %coherent structures identified with the chosen method.
    %This provides an unfiltered array of values from the chosen ID method
    %which are stored in cal_mat:
    [cal_mat,grid_y,grid_x]=vortex_computation(uvec,vvec,vortex_method,...
        gradient_method,ModMag,vector_spacing);
    %A trial filtering scheme is set using C_mag and a_filt. C_mag is a
    %subjective number used to define the vortex core regions within the
    %cal_mat array when it is contoured in "vortex_identification.m". The
    %a_filt term is another subjective term to filter out the unwanted
    %identified structures in cal_mat whom have closed-contour areas
    %less then or equal to a_filt:
    C_mag=35;
    a_filt=25;
    %The function "vortex_identification.m" written by Chris Weiland and
    %modified by Andrew Gifford uses the filtering criteria to sort out the
    %best candidate vortices and calculate their location, area, and
    %strength. An array called cal_mat_new is returned which may be used to
    %compare with the original unfiltered cal_mat to see the effects of
    %filtering coefficients C-mag and a_filt. This allows for user
    %feedback and adjustment on a trial time step.
    [vortex_centers,circulation,area,cal_mat_new]=...
        vortex_identification(abs(cal_mat),C_mag,uvec,vvec,ModMag,a_filt);
    [vrow,vcol]=size(vortex_centers);
    kstep=(k+(timeskip-1))/timeskip;
    %Storage of the vortex properties for each identified vortex in
    %"vortarray" matrix which is saved for each time step.
    vort_vec=[k*[ones(1,vrow)]',vortex_centers,(circulation.*100^2)',...
        (area.*100^2)'];
    vortarray(1:vrow,1:5,kstep)=[vort_vec(1:vrow,1),vort_vec(1:vrow,2),...
        vort_vec(1:vrow,3),vort_vec(1:vrow,4),vort_vec(1:vrow,5)];
    tempmat=vortarray(1:vrow,1:5,kstep);
    tempname=['vortarray_', 'step_', num2str(kstep), '.mat'];

```

```

save(tempname,'tempmat')
disp(['Time step ',num2str(k),' done'])
%Use the following commented section to determine visually how well the
%filtering levels are performing:
%   figure
%   hold on
%   contourf(X,Y,abs(cal_mat(:,:)),[C_mag C_mag]);
%   quiver(X,Y,uvec,vvec,5)
%   colorbar
%   ylim([0 207]*vector_spacing*Magnification*100/(10^6));
%   xlim([0 173]*vector_spacing*Magnification*100/(10^6));
%   title('Pre-Filtered Coherent Structure ID Contours')
%   xlabel('x (cm)')
%   ylabel('y (cm)')
%   hold off
%%%%%%%%%%%%%%%%%%%%%%%%%%%%%%%%%%%%%%%%%%%%%%%%%%%%%%%%%%%%%%%%%%%%%%%%
%   figure
%   hold on
%   contourf(X,Y,cal_mat_new(:,:),[C_mag C_mag]);
%   quiver(X,Y,uvec,vvec,5)
%   colorbar
%   ylim([0 207]*vector_spacing*Magnification*100/(10^6));
%   xlim([0 173]*vector_spacing*Magnification*100/(10^6));
%   title('Post-Filtered Coherent Structure ID Contours')
%   xlabel('x (cm)')
%   ylabel('y (cm)')
%   hold off
%%%%%%%%%%%%%%%%%%%%%%%%%%%%%%%%%%%%%%%%%%%%%%%%%%%%%%%%%%%%%%%%%%%%%%%%
%   figure
%   hold on
%   quiver(X,Y,uvec,vvec,5)
%   r=plot(vortarray(:,2,kstep)*vector_spacing*Magnification/...
%   (10^6)*100,vortarray(:,3,kstep)*vector_spacing*Magnification/...
%   (10^6)*100,'o','MarkerSize',5);
%   set(r,'MarkerFaceColor',graymap(k,:), 'MarkerEdgeColor','k');
%   ylim([0 207]*vector_spacing*Magnification*100/(10^6));
%   xlim([0 173]*vector_spacing*Magnification*100/(10^6));
%   xlabel('x (cm)')
%   ylabel('y (cm)')
%   title(['Filtered Vortex Identification Core Locations Using'...
%   ,gradient_method_2,'GradientEst.',' and ',...
%   vortex_method,' Vortex ID Scheme'])
%   pause
%   close all
clear temp_nameu temp_namev uvec vvec cal_mat grid_y grid_x...
vortex_centers circulation area cal_mat_new vort_vec vortarray
end

```

The following codes are general use in the AETHER Laboratory and may be obtained by permission of the original author(s): "vortex_identification.m", "vortex_computation.m", and "vortex_circulation.m" and as such will not be included herein.

```

%"Vortex_Tracking.m" written by Andrew Gifford to provide the AETHER
%Laboratory with a basic framework for tracking coherent strucutres within
%a time series of TRDPIV flowfields. The code is currently set up to import
%the "vortarray_step_x.mat" files generated from the code named

```

```

%"VortexIdentificationScheme.m" These arrays are read in separately to form
%a master array called "vortarray" from which tracking is performed. The
%tracking algorithm, although customized, is based on the work of Samtaney
%et al. The basic approach is to examine an identified structure at the
%current time step and compare it to all other structures identified at all
%other times in the future. A candidate tracked structure will satisfy
%several change criteria: displacement in x and y, circulation strength,
%orientation, and time.

clear all
close all
clc
tic
maxlen=0;
%Choose which time steps to read in for tracking:
start=1;
skip=1;
stop=3278;
Fs=62.5; %Hz Final sampling frequency of data used to generate
%vortarray_step_x.mat files within function VortexIdentificationScheme.m
%Pre-screen the vortarray_step_x.mat files to determine the appropriate
%number of rows (maxlen) for building the master array "vortarray".
for uu=start:skip:stop
    load(['vortarray_step_',num2str(uu)]);
    if length(tempmat)>maxlen
        maxlen=max(size(tempmat));
    else
        end
end
end
%Read in the vortarray_step_x.mat files sequentially to build the three
%dimensional array "vortarray":
for vv=start:1:stop
    load(['vortarray_step_',num2str(vv)]);
    [row,col]=size(tempmat);
    vortarray(1:maxlen,1:5,vv)=padarray(tempmat, maxlen-row, 0,'post');
    clear tempmat
end
end
%Identify the size of vortarray:
[m,n,p]=size(vortarray);
%Set key parameters for velocity and gage location calculations:
Magnification=105.25; %micron/pixel
vector_spacing=4; %image vector spacing
gagelocy=106.5*vector_spacing*Magnification*100/(10^6);%(cm)
gagelocx=173*vector_spacing*Magnification*100/(10^6);%(cm)
%Set the limits of displacement in x and y between time steps. These values
%may be estimated if a mean propagation velocity is known. Also, set limits
%on the amount of time that may elapse between tracked structures.
dist_lim_x=0.03; %cm
dist_lim_y=0.05; %cm
time_lim=(1/Fs)*skip; %seconds
%Zero initialize arrays for tracking:
vortcount=0;
count=0;
temp_x_1(1:m)=0;
temp_y_1(1:m)=0;
temp_G_s2(1:m,1:p)=0;
temp_G_s1(1:m)=0;

```

```

Master_Array(1:100,1:5,1:100)=0;
temp_t_2(1:m,1:p)=0;
temp_x_2(1:m,1:p)=0;
temp_y_2(1:m,1:p)=0;
temp_G_2(1:m,1:p)=0;
temp_G_s2(1:m,1:p)=0;
res_x(1:m,1:p)=0;
res_y(1:m,1:p)=0;
res_t(1:m,1:p)=0;
%For comparison of vortices at time step i=1 through
%time step i=p-1:
for i=1:p-1
    %For time step, i, look at each structure, j, present in the flow field
    %at that time step for comparison with all other structures identified
    %at all other times:
    for j=1:m
        %Extract the values of x, y, and the rotation sign for the chosen
        %structure:
        temp_x_1(j)=(vortarray(j,2,i))';
        temp_y_1(j)=(vortarray(j,3,i))';
        temp_G_s1(j)=sign(vortarray(j,4,i))';
        %For a non-zero valued structure within the
        %"vortarray" matrix, initialize a counter and set the starting or
        %original structure to the one in question:
        if temp_x_1(j)~=0 && temp_y_1(j)~=0
            vortcount=vortcount+1;
            orig_vort=vortarray(j,:,i);
            %For the given structure, compare it to those at the next time
            %step after the one you're on and continue till the end using a
            %dummy time index k:
            for k=(i+1):1:(p-1)
                if k==i+1
                    temp_G_s2(1:m,k)=temp_G_s1(j);
                    Master_Array(1,1:5,vortcount)=[orig_vort];
                else
                    %Extract all other structures at time step, k, and use
                    %search criteria to identify if the candidate structure
                    %should be kept, i.e. tracked with structure "j":
                    temp_t_2(:,k)=(vortarray(:,1,k))';
                    temp_x_2(:,k)=(vortarray(:,2,k))';
                    temp_y_2(:,k)=(vortarray(:,3,k))';
                    temp_G_2(:,k)=(vortarray(:,4,k))';
                    temp_G_s2(:,k)=sign(vortarray(:,4,k))';
                    %This section uses dummy variable "q" to scan through
                    %the structures extracted above at time step ,k, and
                    %uses residual values for comparison with the criterion
                    %for displacement, time, and circulation orientation
                    %described previously:
                    for q=1:m
                        if temp_x_2(q,k)~=0 && temp_y_2(q,k)~=0
                            res_G(q,k)=abs((abs(temp_G_2(q,k))-...
                                abs(Master_Array(count+1,4,vortcount)))...
                                /Master_Array(count+1,4,vortcount));
                            res_x(q,k)=abs(((temp_x_2(q,k)-...
                                Master_Array(count+1,2,vortcount)))...
                                /Master_Array(count+1,2,vortcount));
                            res_y(q,k)=abs(((temp_y_2(q,k)-...

```

```

        Master_Array(count+1,3,vortcount)))...
        /Master_Array(count+1,3,vortcount));
res_t(q,k)=(temp_t_2(q,k)-...
        Master_Array(count+1,1,vortcount));
%If structure "q" meets all the criterion it is
%kept as a tracked structure for structure "j"
%and stored in the "Master_Array" which is a
%three dimensional array having rows
%corresponding to time, columns containing the
%structures physical properties at each time
%step in the tracking, and a third dimension
%which is a counter for each unique tracked
%structure:
if all([res_x(q,k)<=dist_lim_x, res_y(q,k)...
        <=dist_lim_y, res_t(q,k)<=time_lim,...
        temp_G_s2(q,k)=...
        sign(Master_Array(count+1,4,...
        vortcount))]=1)
        count=count+1;
        tempvort=[vortarray(q,:,k)];
        Master_Array(count+1,1:5,...
        vortcount)=[tempvort];
        vortarray(q,:,k)=0;
        clear tempvort
    else
    end
end
end
end
end
count=0;
pause(0.01)
disp(['Vortex Track ',num2str(vortcount),' done'])
else
end
end
end
save Master_Array_Long.mat Master_Array

```

```

%Use this section of code to extract only the longest lived structures from
%the Master_Array:
clear all
close all
clc
load('Master_Array_Long.mat')
[xx,yy,zz]=size(Master_Array);
countb=0;
counta=0;
for tt=1:zz
    for pp=1:xx;
        if abs(Master_Array(pp,2,tt))>0
            countb=countb+1;
        else
        end
    end
end
if countb>32 %Time intervals...actual tracking time = #*(1/Fs)

```

```

        counta=counta+1;
        Master_Array_2(:,:,counta)=Master_Array(:,:,tt);
    else
    end
    countb=0;
end
save MasterArray_Long.mat Master_Array_2
pack
%%%%%%%%%%%%%%%%%%%%%%%%%%%%%%%%%%%%%%%%%%%%%%%%%%%%%%%%%%%%%%%%%%%%%%%%
%This section is used to compute the spatial cross-correlation based length
%scale analysis which requires function "length_scale.m".

clear all
close all
clc
%Read in the stored coherent structure tracks:
load('MasterArray_Long.mat')
Magnification=105.25; %micron/pixel
vector_spacing=4; %image vector spacing
FsV=125; %Sampling frequency between correlated images

tic
[xx3,yy3,zz3]=size(Master_Array_2);
for z=1:zz3
    tic
    %Send the structure core location points for each tracked structure
    %to the length scale calculation algorithm:
    [a,b,c,d]=length_scale(Master_Array_2(:,:,z),vector_spacing,...
        Magnification,FsV);
    L_x_plus=padarray(a, xx3-length(a), 0, 'post');
    L_x_minus=padarray(b, xx3-length(b), 0, 'post');
    L_y_plus=padarray(c, xx3-length(c), 0, 'post');
    L_y_minus=padarray(d, xx3-length(c), 0, 'post');
    LS_Array(:,1:4)=[L_x_plus L_x_minus L_y_plus L_y_minus];
    disp(['Length_Scales_Track_test_',num2str(z),' done'])
    %Save the final properties of each tracked structure in separate .mat
    %filed for later use:
    tempname=['Vortex_Track_Long_', 'Number_',num2str(z),'.mat'];
    save(tempname,'LS_Array')
    clear a b c d L_x_plus L_x_minus L_y_plus L_y_minus LS_Array
    toc
end
toc

%Rebuild the total matrix of vortex tracks including length scale for later
%use:
clear all
close all
clc
load('MasterArray_Long.mat')
[xx3,yy3,zz3]=size(Master_Array_2);
for p=1:1:179
    tempname=['Vortex_Track_Long_', 'Number_',num2str(p),'.mat'];
    load(tempname);
    Master_Array_2(:,6:9,p)=LS_Array(:,1:4);
end
end

```

```

save MasterArray_Longb.mat Master_Array_2

%"length_scale.m" written by Andrew Gifford is used to calculate the
%spatial integral length scales (i.e. transverse and longitudinal) for a
%given tracked coherent structure as it moves through space and time within
%the TRDPIV flowfield.
%The inputs to the function are the coherent structure's core location
%through time as provided by the Vortex_Tracking.m algorithm, the vector
%spacing in the TRDPIV data, and the sampling frequency of the
%original TRDPIV image pairs.

function [L_x_plus L_x_minus L_y_plus L_y_minus]=...
    length_scale(Vorts,vec_space,mag,FsV);

%Input vector spacing and image magnification:
vec_space=4; %Pixels
mag=100;     %microns/pixel

%Calculate the size of the tracked coherent structure data and eliminate
%zero padded values:
[xx,yy,zz]=size(Vorts);
countb=0;
for pp=1:xx;
    if abs(Vorts(pp,2,1))>0
        countb=countb+1;
    else
        end
end

Vorts=Vorts(1:countb,:,1);
%For the given tracked coherent structure, the mean and fluctuating
%velocity are required at each core location through time.
%First, noise in the coherent structure's tracked core locations is
%filtered out mildly with the low pass filtering of the smooth.m function:
t=Vorts(:,1,1);
span=round(length(Vorts(:,2,1))/6);
x=round(smooth(Vorts(:,2,1),span,'rloess'));
y=round(smooth(Vorts(:,3,1),span,'rloess'));
%Now read in the velocity fields at each time step in the coherent
%structure track:
for k=1:length(t)
    temp_nameu=strcat('uVelsFrame',num2str(t(k)));
    temp_namev=strcat('vVelsFrame',num2str(t(k)));
    uvec(:, :,k)=load(temp_nameu,'-ascii');
    vvec(:, :,k)=load(temp_namev,'-ascii');
    uvec(:, :,k)=uvec(:, :,k)*mag/10^6*FsV;%m/s;
    vvec(:, :,k)=vvec(:, :,k)*mag/10^6*FsV;%m/s;
end

%Compute the u'rms and v'rms matrices:
[Ly,Lx,Lt]=size(uvec);
%Load pre-computed mean flow field velocity arrays:
load('MeanU.mat')
load('MeanV.mat');
%Calculate fluctuating velocity values:
for j=1:1:Ly

```

```

for i=1:1:Lx
uprime(j,i,:)=uvec(j,i,:)-mean(uvec(j,i,:));
vprime(j,i,:)=vvec(j,i,:)-mean(vvec(j,i,:));
end
end
pack
%For each vortex time step pick out the corresponding location in the flow
%field of the core and calculate the transverse and longitudinal integral
%length scales from that point using the fluctuating velocities at that
%location. This is done using a normalized cross-correlation coefficient.
%The calculations are repeated in a 3x3 grid around the true core location
%to obtain a better average value of the integral length scales. This was
%done to mitigate errors in integral length scale due to poor
%identification of the true structural core location which can happen using
%the vortex ID scheme.
for qq=1:3
    for ww=1:3
        for k=1:length(t)
            xstart=[x(k)-1, x(k), x(k)+1];
            ystart=[y(k)-1, y(k), y(k)+1];
            tstart=k;
            x_plus=[Lx-xstart(qq)+1];
            x_minus=xstart(qq)+1;
            y_plus=Ly-ystart(ww)+1;
            y_minus=ystart(ww)+1;
            Rx_plus_r=[0:1:x_plus-1];
            Rx_minus_r=[0:1:x_minus-2];
            Ry_plus_r=[0:1:y_plus-1];
            Ry_minus_r=[0:1:y_minus-2];
            %The cross-correlation coefficients in space:
            for w=1:length(Rx_plus_r)
                Rx_plus(w)=(uprime(ystart(ww),xstart(qq),tstart)*...
                    uprime(ystart(ww),xstart(qq)+(w-1),tstart))/...
                    (uprime(ystart(ww),xstart(qq),tstart)*...
                    uprime(ystart(ww),xstart(qq),tstart)));
            end
            for e=1:length(Rx_minus_r)
                Rx_minus(e)=(uprime(ystart(ww),xstart(qq),tstart)*...
                    uprime(ystart(ww),xstart(qq)-(e-1),tstart))/...
                    (uprime(ystart(ww),xstart(qq),tstart)*...
                    uprime(ystart(ww),xstart(qq),tstart)));
            end
            for f=1:length(Ry_plus_r)
                Ry_plus(f)=(vprime(ystart(ww),xstart(qq),tstart)*...
                    vprime(ystart(ww)+(f-1),xstart(qq),tstart))/...
                    (vprime(ystart(ww),xstart(qq),tstart)*...
                    vprime(ystart(ww),xstart(qq),tstart)));
            end
            for g=1:length(Ry_minus_r)
                Ry_minus(g)=(vprime(ystart(ww),xstart(qq),tstart)*...
                    vprime(ystart(ww)-(g-1),xstart(qq),tstart))/...
                    (vprime(ystart(ww),xstart(qq),tstart)*...
                    vprime(ystart(ww),xstart(qq),tstart)));
            end
            %Use first zero crossing method to find the integral length
            %scales in the transverse and longitudinal directions (cm):

```

```

L_x_plus(k,ww,qq)=L1_FZCM_Spatial(Rx_plus,Rx_plus_r,vec_space,mag);

L_x_minus(k,ww,qq)=L1_FZCM_Spatial(Ry_plus,Ry_plus_r,vec_space,mag);

L_y_plus(k,ww,qq)=L1_FZCM_Spatial(Ry_plus,Ry_plus_r,vec_space,mag);

L_y_minus(k,ww,qq)=L1_FZCM_Spatial(Ry_plus,Ry_plus_r,vec_space,mag);
    clear w xstart ystart tstart x_plus x_minus y_plus y_minus
Rx_plus_r...      Rx_minus_r Ry_plus_r Ry_minus_r Rx_plus Rx_minus Ry_plus
Ry_minus
    pack
    end
    end
    end
end
%Filtering of noise and averaging over 3x3 set of values:
[p1,q1,r1]=size(L_x_plus);
[p2,q2,r2]=size(L_x_minus);
[p3,q3,r3]=size(L_y_plus);
[p4,q4,r4]=size(L_y_minus);
L_x_plus=MedianFilter(L_x_plus,10.0,10.0);
L_x_minus=MedianFilter(L_x_minus,10.0,10.0);
L_y_plus=MedianFilter(L_y_plus,10.0,10.0);
L_y_minus=MedianFilter(L_y_minus,10.0,10.0);
for d1=1:p1
L_x_plustemp(d1,1)=sum(sum(L_x_plus(d1,1:3,1))+sum(L_x_plus(d1,1:3,2))+...
    sum(L_x_plus(d1,1:3,3)))/9;
end
for d2=1:p2
L_x_minustemp(d2,1)=sum(sum(L_x_minus(d2,1:3,1))+sum(L_x_minus(d2,1:3,2))+...
    sum(L_x_minus(d2,1:3,3)))/9;
end
for d3=1:p3
L_y_plustemp(d3,1)=sum(sum(L_y_plus(d3,1:3,1))+sum(L_y_plus(d3,1:3,2))+...
    sum(L_y_plus(d3,1:3,3)))/9;
end
for d4=1:p4
L_y_minustemp(d4,1)=sum(sum(L_y_minus(d4,1:3,1))+sum(L_y_minus(d4,1:3,2))+...
    +sum(L_y_minus(d4,1:3,3)))/9;
end
L_x_plus=L_x_plustemp;
L_x_minus=L_x_minustemp;
L_y_plus=L_y_plustemp;
L_y_minus=L_y_minustemp;

%"L1_FZCM_Spatial.m" written by Andrew Gifford
%This function is used solely by "length_scale.m" to calculate the spatial
%integral length scale.

function [L]=L1_FZCM_Spatial(R,Rx,vec_space,mag)

%Find first zero crossing of the cross-correlation coefficient if present:
MinVal=find(R<=0);
taumin=MinVal(1);
%Take total range if needed:
if isempty(taumin)

```

```

    taumin(1)=max(Rx);
else
end
%Integrate the cross-correlation coefficient to the first zero crossing and
%calculate the spatial integral length scale:
L=trapz(R(1:taumin(1)))*vec_space*mag*0.0001;%cm
%Optional viewing of cross-correlation coefficient:
% figure
% hold on
% plot(Rx,R)
% plot(taumin(1),R(taumin(1)),'*')

%"TrackedStructureAnalysis.m" written by Andrew Gifford is used to examine
%the transient physical properties of the tracked coherent structures and
%use this information to model and predict the experimentally measured heat
%transfer. The code requires the MasterArraymat file of coherent structure
%properties generated with the Vortex_Tracking.m code.

clear all
close all
clc

%Read in the required data sets:
load('MasterArray.mat');
V=Master_Array_2;
%Determine array size and input required constants:
[xV,yV,zV]=size(V);
Fs=62.5; %final data set frequency in Hz
gridspace=4; %image vector spacing pixels
Magnification=105.25; %image magnification in microns/pixel
gagelocy=106.5*gridspace*Magnification*100/(10^6);
gagelocx=173*gridspace*Magnification*100/(10^6);
maxy=207*gridspace*Magnification*100/(10^6);
maxx=173*gridspace*Magnification*100/(10^6);
%Read in the simultaneous heat transfer data:
load('Concurrent_TRDPIV_HF_DataG1T2.mat');
Q=(Concurrent_TRDPIV_HF_Data);
%Input required constants for heat transfer analysis and downsample to Fs:
t=decimate(Q(1,:),16);
t=t-t(1);
h=decimate(Q(3,:),16);
[xQ,yQ,zQ]=size(t);
Ttable=[273.15 280 290 295 300 305 310 315 320 325]';%(K)
ktable=[0.569 .582 .589 .606 .613 .620 .628 .634 .640 .645]';%(W/mK)
Prtable=[12.99 10.26 7.56 6.62 5.83 5.20 4.62 4.16 3.77 3.42]';%(ND)
Viscosity=[0.001750 0.001422 0.001080 0.000959 0.000855 0.000769...
0.000695 0.000631 0.000577 0.000528]';%(Ns/m^2)
specvol=[0.001 0.001 0.001001 0.001002 0.001003 0.001005 0.001007...
0.001009 0.001011 0.001013]';%(m^3/kg)
Pr=interp1(Ttable(:,1),Prtable(:,1),(30.8+273.15));%(ND)
k=interp1(Ttable(:,1),ktable(:,1),(30.8+273.15))/100;%(W/cmK)
knu=((interp1(Ttable(:,1),Viscosity(:,1),(30.8+273.15)))*...
(interp1(Ttable(:,1),specvol(:,1),(30.8+273.15))))*100^2;%(cm^2/s)
alpha=knu/Pr;
%Initialize array for induced velocity calculations:
master_induced_velocity=[0 0 0 0];

```

```

%Begin analysis of each vortex track:
for i=1:zV
    tempmat=0;
    tempvar=V(:,1,i);
    %Determine array zero padding start point:
    [p1]=find(abs(V(:,4,i))<=0);
    if isempty(p1), p1=length(tempvar-1);else end
    %Low-pass filter coherent structure data to eliminate noise errors:
    smooth_len1=round(0.05*p1(1));
    smooth_len2=round(0.05*p1(1));
    smooth_len3=round(0.05*p1(1));
    temp_vort_track_t=V((1:p1(1)-1),1,i).*(1/Fs);
    temp_vort_track_x=smooth(V((1:p1(1)-1),2,i)*gridspace*Magnification...
        *100/(10^6),smooth_len1,'rloess');
    temp_vort_track_y=smooth(V((1:p1(1)-1),3,i)*gridspace*Magnification...
        *100/(10^6),smooth_len1,'rloess');
    temp_vort_track_gamma=smooth(V((1:p1(1)-1),4,i),smooth_len2,'rloess');
    temp_vort_track_spin=sign(V((1:p1(1)-1),4,i));
    temp_vort_track_area=V((1:p1(1)-1),5,i);
    temp_vort_track_Lmean=smooth(mean([V((1:p1(1)-1),6,i),...
        V((1:p1(1)-1),8,i)],2),smooth_len3,'rloess');
    temp_vort_track_Lx=smooth(V((1:p1(1)-1),6,i),smooth_len3,'rloess');
    temp_vort_track_Ly=smooth(V((1:p1(1)-1),8,i),smooth_len3,'rloess');
    %Calculate distances of core to heat flux sensor location:
    for kk=1:length(temp_vort_track_t)
        if temp_vort_track_y(kk)>=gagelocy
            %Distance from wall, always >=0
            distx(kk)=(gagelocx-temp_vort_track_x(kk));
            disty(kk)=temp_vort_track_y(kk)-gagelocy;
            dist(kk)=sqrt(distx(kk)^2+disty(kk)^2);
        else
            %Distance from wall, always >=0
            distx(kk)=(gagelocx-temp_vort_track_x(kk));
            disty(kk)=gagelocy-temp_vort_track_y(kk);
            dist(kk)=sqrt(distx(kk)^2+disty(kk)^2);
        end
    end
end
%Determine the cumulative induced velocity components
%for each tracked structure which is location and spin orientation
%dependent:
for pp=1:p1(1)-1
    if spin(pp)<0
        countspinminus=countspinminus+1;
    else
        countspinplus=countspinplus+1;
    end
    %Induced velocity magnitude using Biot-Savart:
    v_ind(pp,i)=abs(temp_vort_track_gamma(pp))/(2*pi*abs(dist(pp)));
    if spin(pp)<0 & disty(pp)>=0 %Positive Quadrant CCW Vortex
        if disty(pp)~=0
            thetal(pp,i)=acosd(distx(pp)/dist(pp));%Degrees
            vx(pp,i)=abs(v_ind(pp,i)*cosd(thetal(pp,i)))*cm/s
            vy(pp,i)=abs(v_ind(pp,i)*sind(thetal(pp,i)))*cm/s
        elseif disty(pp)==0;
            vx(pp,i)=0;
            vy(pp,i)=v_ind(pp,i);
        else

```

```

end
elseif spin(pp)<0 & disty(pp)<=0 %Negative Quadrant CCW Vortex
if disty(pp)~=0
    thetal(pp,i)=acosd(distx(pp)/dist(pp));%Degrees
    vx(pp,i)=-1*abs(v_ind(pp,i)*tand(thetal(pp,i)));//cm/s
    vy(pp,i)=abs(sqrt(v_ind(pp,i)^2-vx(pp,i)^2));%cm/s
elseif disty(pp)==0;
    vx(pp,i)=0;
    vy(pp,i)=v_ind(pp,i);
else
end
elseif spin(pp)>0 & disty(pp)>=0 %Positive Quadrant CW Vortex
if disty(pp)~=0
    thetal(pp,i)=acosd(distx(pp)/dist(pp));%Degrees
    vx(pp,i)=-1*abs(v_ind(pp,i)*cosd(thetal(pp,i)));//cm/s
    vy(pp,i)=-1*abs(v_ind(pp,i)*sind(thetal(pp,i)));//cm/s
elseif disty(pp)==0;
    vx(pp,i)=0;
    vy(pp,i)=-1*v_ind(pp,i);
else
end
elseif spin(pp)<0 & disty(pp)<=0 %Negative Quadrant Cw Vortex
if disty(pp)~=0
    thetal(pp,i)=acosd(distx(pp)/dist(pp));%Degrees
    vx(pp,i)=abs(v_ind(pp,i)*tand(thetal(pp,i)));//cm/s
    vy(pp,i)=-1*abs(sqrt(v_ind(pp,i)^2-vx(pp,i)^2));%cm/s
elseif disty(pp)==0
    vx(pp,i)=0;
    vy(pp,i)=-1*v_ind(pp,i);
else
end
else
    thetal(pp,i)=0;
    vx(pp,i)=0;
    vy(pp,i)=0;
end
%Use induced velocity magnitude to calculate heat transfer using
%the original Nix et al. model:
Re(pp,i)=abs(v_ind(pp,i))*temp_vort_track_Lmean(pp)/knu;
dH_Nix(pp,i)=0.5642*(k/temp_vort_track_Lmean(pp))*sqrt(Pr)*...
    sqrt(Re(pp,i));
time(pp,i)=temp_vort_track_t(pp);
end
%Build an array of time and induced velocities:
tempmat=[temp_vort_track_t,vx(1:length(temp_vort_track_t),i),...
    vy(1:length(temp_vort_track_t),i),temp_vort_track_Lmean];
master_induced_velocity=cat(1,master_induced_velocity,tempmat);
clear temp_vort_track_t temp_vort_track_x temp_vort_track_y...
    temp_vort_track_gamma temp_vort_track_area...
    temp_vort_track_Lmean dist p1 temp1 temp2 tempmat
end

%Plot original model versus experimentally measured heat transfer:
vortpic=13;
figure
hold on
plot(t,h,'r')

```

```

plot(time(:,1),dH_Nix(:,vortpic),'k')
xlabel('time (s)')
ylabel('h_{Turb}(t) (W/cm^2-^oC)')
legend('HFA Signal','Nix Method')
xlim([0 47])

%Cumulative Induced Velocity Analysis and Predictions of Heat Transfer:
%Set time step for analysis:
time_step=0.04;
time_mat=[0:time_step:max(t)];
temp1=master_induced_velocity(:,1);
%For each time instance in the experimentally measured heat transfer data,
%examine what the mechanistic model predicts:
for pp=1:1:length(time_mat)
    [r2,c2]=find((time_mat(pp)-time_step/3)<temp1 &...
        temp1<(time_mat(pp)+time_step/3));
    if isempty(r2)==0
        for kk=1:length(r2)
            timer(kk)=temp1(r2(kk));
            length_scale_val(kk)=master_induced_velocity(r2(kk),4);
        end
        vx_final(pp)=sum(master_induced_velocity(r2,2));
        vy_final(pp)=sum(master_induced_velocity(r2,3));
        velocity(pp)=sqrt(vx_final(pp)^2+vy_final(pp)^2);
        mean_vel_mag1(pp)=velocity(pp);
        mean_vel_mag2(pp)=vx_final(pp);
        mean_vel_mag3(pp)=vy_final(pp);
        mean_time(pp)=mean(timer);
        mean_L_total(pp)=mean(length_scale_val);
        Re_total1(pp)=abs(mean_vel_mag1(pp))*mean_L_total(pp)/knu;
        Re_total2(pp)=abs(mean_vel_mag2(pp))*mean_L_total(pp)/knu;
        Re_total3(pp)=abs(mean_vel_mag3(pp))*mean_L_total(pp)/knu;
        %The three predicted heat transfer quantities using the cumulative
        %induced velocities:
        mean_h_total1(pp)=0.5642*(k/mean_L_total(pp))*sqrt(Pr)*...
            sqrt(Re_total1(pp))+0.053;
        mean_h_total2(pp)=0.5642*(k/mean_L_total(pp))*sqrt(Pr)*...
            sqrt(Re_total2(pp))+0.053;
        mean_h_total3(pp)=0.5642*(k/mean_L_total(pp))*sqrt(Pr)*...
            sqrt(Re_total3(pp))+0.053;
        clear timer length_scale_val r2 c2 tfind
    else
        mean_vel_mag1(pp)=0;
        mean_vel_mag2(pp)=0;
        mean_vel_mag3(pp)=0;
        mean_time(pp)=0;
        mean_L_total(pp)=0;
        Re_total1(pp)=0;
        Re_total2(pp)=0;
        Re_total3(pp)=0;
        mean_h_total1(pp)=0;
        mean_h_total2(pp)=0;
        mean_h_total3(pp)=0;
    end
end
end

```

```

%Plots of cumulative induced velocity predicted heat transfer versus
%experimentally measured values:
[xt,yt]=size(mean_time);
last=380;
figure
hold on
plot(t,h,'r')
plot(mean_time(1:yt-last),smooth(mean_h_total1(1:yt-last),15,'rloess'),'k')
xlabel('time (s)')
ylabel('h_{Turb}(t) (W/cm^2-^oC)')
legend('HFA Signal','Cumulative Velocity Method (u_{\theta-C})')
xlim([0 47])

figure
hold on
plot(t,h,'r')
plot(mean_time(1:yt-last),smooth(mean_h_total2(1:yt-last),15,'rloess'),'k')
xlabel('time (s)')
ylabel('h_{Turb}(t) (W/cm^2-^oC)')
legend('HFA Signal','Cumulative Velocity Method (u_{\theta_x-C})')
xlim([0 47])

figure
hold on
plot(t,h,'r')
plot(mean_time(1:yt-last),smooth(mean_h_total3(1:yt-last),15,'rloess'),'k')
xlabel('time (s)')
ylabel('h_{Turb}(t) (W/cm^2-^oC)')
legend('HFA Signal','Cumulative Velocity Method (u_{\theta_y-C})')
xlim([0 47])

```